Ph.D. Dissertation

Design of Analog Front-End of Touch-Screen Controller with Enhanced Noise Immunity and Configurable SNR and Frame Rate

SNR 및 Frame Rate 의 조절이 가능하고 강화된 잡음 면역성을 가지는 터치스크린 컨트롤러용 아날로그 전단 회로의 설계

by

Jun-Eun Park

February, 2017

Department of Electrical Engineering
and Computer Science
College of Engineering
Seoul National University

Design of Analog Front-End of Touch-Screen Controller with Enhanced Noise Immunity and Configurable SNR and Frame Rate

지도 교수 정 덕 균

이 논문을 공학박사 학위논문으로 제출함
2016 년 8 월

서울대학교 대학원
전기·컴퓨터공학부
박 준 은

박준은의 박사 학위논문을 인준함
2016 년 8 월

위 원 장 ______________________ (인)

부위원장 ______________________ (인)

위 원 ______________________ (인)

위 원 ______________________ (인)

위 원 ______________________ (인)

Design of Analog Front-End of Touch-Screen Controller with Enhanced Noise Immunity and Configurable SNR and Frame Rate

by

Jun-Eun Park

A Dissertation Submitted to the Department of
Electrical Engineering and Computer Science
in Partial Fulfillment of the Requirements for the Degree of
Doctor of Philosophy
at
SEOUL NATIONAL UNIVERSITY

August, 2016

Committee in Charge:

Chairman	Hyuk-Jae Lee
Vice-Chairman	Deog-Kyoon Jeong
Member	Jaejin Park
Member	Yongsam Moon
Member	Jung-Hoon Chun

Abstract

Design of Analog Front-End of Touch-Screen Controller with Enhanced Noise Immunity and Configurable SNR and Frame Rate

Jun-Eun Park
Department of Electrical Engineering and Computer Science
College of Engineering
Seoul National University

A design of analog front-end (AFE) for touch-screen controller (TSC) with highly enhanced noise immunity and configurable signal-to-noise ratio (SNR) and frame rate is proposed. First, the AFE for the mobile TSC is presented, which provides a configurable SNR and frame rate. The AFE configures its SNR and frame rate by adjusting the sampling cycles of the employed ADC. The test chip is fabricated in a 0.18-μm CMOS process and occupies a 2.2-mm^2 active area. The test chip achieves 60-dB SNR and 200-Hz frame rate with 12 × 8 TSP. The SNR can be adjusted from 40 to 67 dB, while the frame rate is then inversely scaled from 50 Hz to 6.4 kHz. The test chip consumes 6.26 mW from a 3.3-V supply.

The AFE for the tablet TSC is also presented, which provides highly enhanced noise immunity and configurable SNR and frame rate. The proposed AFE provides TX channels of 36 and RX channels of 64 in order to support a large-size TSP. A multi-driving TX structure with frequency-hopping signal generator is employed to improve the SNR and noise immunity. For a suppression of severe noise interference injected through the TSP, the RX sensing block adopts pre-filtering differential sensing method and high-order noise filtering structure. The AFE supports configurable SNR and frame rate with on-chip frame-rate controller. The test chip is fabricated in a 0.18-μm CMOS process. The active area of the test chip is 36 mm^2. A 12.2-inch TSP with TX channels of 36 and RX channels of 64 is used in the measurement. The test chip achieves 54-dB SNR and 120-Hz frame rate with a finger touch. The frame rate can be adjusted from 85 to 385 Hz. The test chip achieves up to 20-V_{pp} noise immunity. The test chip consumes 94.5 mW with a 3.3-V supply.

Keywords : Touch-screen controller (TSC), analog front-end (AFE), noise immunity, signal-to-noise ratio (SNR), frame rate, touch-screen panel (TSP).

Student Number : 2013-30237

Contents

CHAPTER 4 AFE OF TABLET TSC WITH ENHANCED NOISE IMMUNITY 35

List of Figures

List of Tables

Chapter 1

Introduction

1.1 Motivation

As increasing use of mobile devices such as smartphone or tablet PC, touch-screen sensor becomes the most widely used input device. The touch-screen sensor does not require additional physical buttons or track point. On the surface of display, the touch-screen sensor detects a touch input by measuring resistance or capacitance variations. Hence, the touch-screen senor provides intuitive human-machine interface (HMI). Multi-touch function of the touch-screen sensor further enriches the user interface. Because the touch-screen sensor can detect input with only light touch, the user can control the device with almost zero force. In addition to the advantages in the aspect of the user interface, the touch-screen sensor provides a number of benefits as the device components. The touch-screen sensor has fine optical quality.

The thickness of the touch-screen sensor is much thinner than other input devices, enabling thin form factor of the devices. Furthermore, the touch-screen sensor can be integrated into the display, which reduces the thickness of the device extremely.

The touch-screen sensor usually consists of two main parts: touch-screen panel (TSP) and touch-screen controller (TSC). The touch-screen panel is a transparent physical sensor which can be overlaid or integrated into the display. Among a number of TSP types, a projected-capacitive TSP has been widely used in these days. The projected-capacitive TSP can be categorized into two types: self-capacitance type and mutual capacitance type. Depending on the capacitance to be sensed, the pattern and design of TSP can be varied. The TSC drives the TSP and senses the variation of capacitance by touch input. Then, the coordinate calculation of the touched point and gesture recognition are performed by the TSC.

Although the touch-screen sensor has been popularly used in the devices, a number of design issues on the touch-screen sensor have not been solved. One of the critical issues on the design of the TSC is noise immunity. The detailed description about the noise immunity and noise interference to the touch-screen sensor will be The real environment of touch sensing is very noisy. Not only display [1.1] but also charger and lamp interfere with the TSC via the TSP [1.2][1.3]. The noise interference overwhelms the capacitance signal by touch input, resulting in malfunction or false touch detection of the TSC. Hence, it is important for the TSC to be immune to such noise interference.

Another design issue on the TSC is a configurable performance. Depending on the applications or user environment, the performances of the TSC, such as signal-to-noise ratio (SNR) or frame rate, are required to be reconfigured. For example, in the noisy environment, high SNR with enhanced noise immunity is more important than high frame rate. Therefore, the configurable SNR and frame rage is essential for the TSC to provide clear touch detection in the noisy environment.

In this thesis, a design of analog front-end of the TSC with highly enhanced noise immunity is proposed. To achieve noise immunity against the severe external interference, a number of techniques applied to TX and RX blocks are introduced. In addition, the configurable SNR and frame rate is proposed in this thesis. As a result, the proposed analog front-end achieves much higher noise immunity than that of the state-of-the-art works.

1.2 Thesis Organization

This thesis is organized as follows. In Chapter 2, an overview on the touch-screen controller is described. In this chapter, the basic structure and design issues of the touch-screen controller (TSC) are explained. The role of analog front-end (AFE) of the touch-screen controller and important performance metrics are also described.

In Chapter 3, a design of AFE for smartphone TSC is presented. System architecture and implementation to achieve high SNR are described. The implementation of configurable SNR and frame rate of the AFE is explained. In addition, the relationships between design factors of the AFE, such as driving voltage or sampling cycles, and performance metrics are explored. Then, the measurement results are described to verify the performance of the proposed AFE architecture.

In Chapter 4, a design of AFE for tablet TSC is presented. The system architecture to achieve enhanced noise immunity of the AFE is mainly covered in this chapter. The implementation configurable SNR and frame rate is also explained, which is improved from that in Chapter 3. Then, the circuit implementations of the proposed architecture are explained. Finally, the measurement results are covered to demonstrate the proposed AFE.

In Chapter 5, the proposed works are summarized with conclusion of this thesis.

Chapter 2

Basic Study on Touch-Screen Controller

2.1 Touch-Screen Panel

In these days, most of touch-screen sensors use the capacitive type TSP. In the past, a resistive type TSP was widely used. But, the capacitive TSP replaces the resistive TSP owing to the capability of the multi-touch detection and high-quality of optical characteristics. There are two types of the capacitive TSP: self-capacitive and mutual-capacitive TSP. The self-capacitive TSP is composed of single-layer multiple electrodes of which capacitances increase against a touch input. On the contrary, the mutual-capacitive TSP usually consists of two layers: driving electrodes and sensing electrodes. As shown in Fig. 2.1, the capacitance between each driving elec-

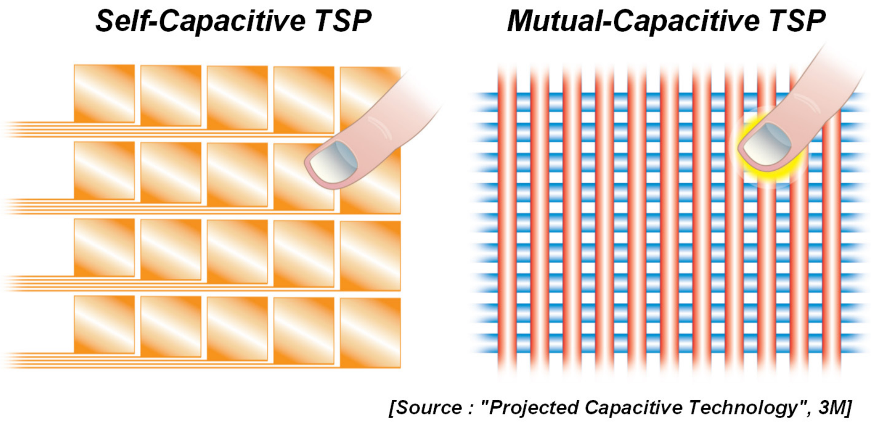

[Source : "Projected Capacitive Technology", 3M]

Fig. 2.1 Self-capacitive TSP and mutual-capcaitive TSP [2.1].

trode and sensing electrode form a mutual capacitance, and the mutual capacitance is reduced when a touch input is applied. More detailed comparison between the self-capacitive TSP and mutual-capacitive TSP is described in [2.1]-[2.3].

Of the two TSP types, the mutual-capacitive TSP is widely employed in the touch-screen sensor. Although the self-capacitive TSP provides higher touch sensitivity and tolerance to water drop, it has a critical drawback of ghost effect that cannot distinguish multi-touch input [2.4]. On the other hand, the mutual-capacitive TSP has a capability of unlimited multi-touch detection. The mutual-capacitive TSP also provides a fine electrode pitch, which enables touch detection of passive stylus. Hence, the mutual-capacitive TSP is popularly used in the touch-screen sensor in these days.

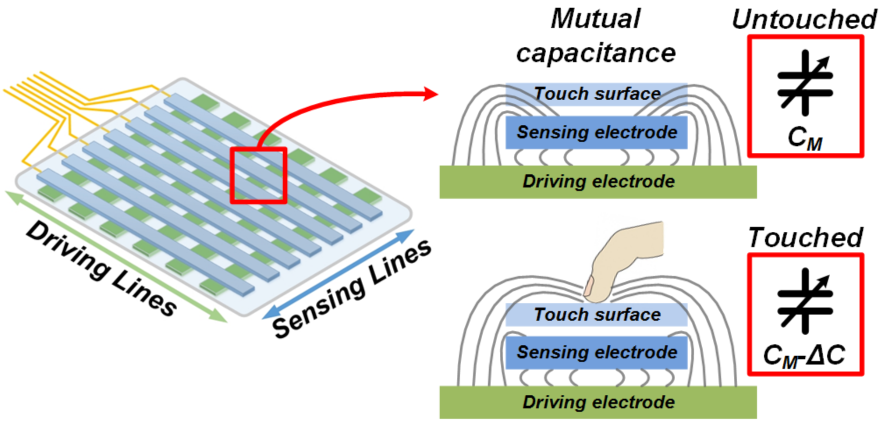

Fig. 2.2 Conceptual diagram of the mutual-capacitive TSP.

The conceptual diagram of the mutual-capacitive TSP is shown in Fig. 2.2. Depending on pattern of the TSP, the formation of mutual capacitance can be varied. In case of Mahattan-type (or bar-type) TSP, the layer of driving electrodes is below that of sensing electrodes. Hence, the mutual capacitance between the driving electrode and sensing electrode is form at each node. Compared to the mutual capacitance without touch input, the mutual capacitance with touch input is reduced because of decreased electric field between the driving electrode and sensing electrode [2.5]. The reduction of mutual capacitance against touch input can be varied depending on the electrode material or electrode pitch. In general, the mutual capacitive TSP provides capacitance variation about 5 ~ 20 % against the finger touch. The variations of the mutual capacitance at each node are sensed by the TSC, which will be explained in the next section.

2.2 Touch-Screen Controller

2.2.1 Overview on TSC

The objects of the touch-screen controller (TSC) are detection of the touch input and calculation of the touched coordinate. The TSC also supports object tracking and gesture recognition. The outputs of the TSC, such as the number of touch inputs and their coordinates, are delivered to host process of the device.

Fig. 2.3 shows the block diagram of the TSC. The TSC is composed of analog front-end (AFE) and digital back-end (DBE). In general, the driving and sensing nodes of the TSC are connected to the TSP via a flexible-printed-circuit board (FPCB). The main role of the AFE is sensing mutual capacitance of each node in the TSP. To sense the mutual capacitance, the AFE applies an excitation signal to the

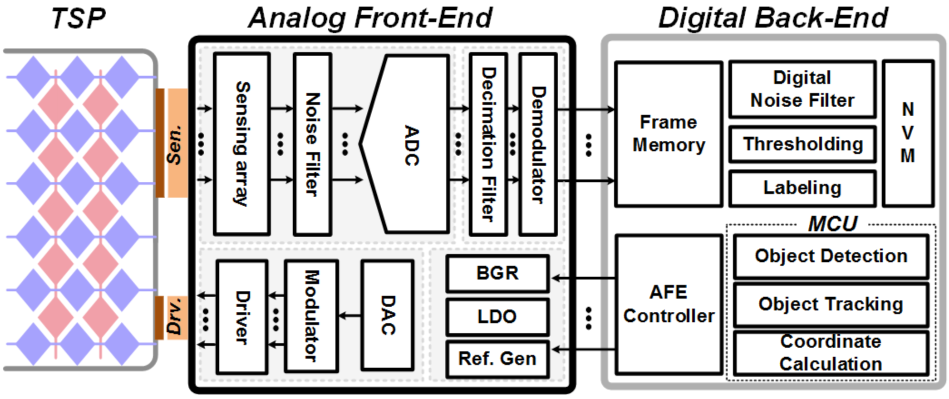

Fig. 2.3 Block diagram of the TSC.

TSP, and the mutual capacitances of each node are carried by the excitation signal. The AFE then senses the carried mutual-capacitance data. At this time, a lot of noise interference is injected through the TSP. Hence, the AFE provides a noise filtering process to prevent a distortion of the capacitance data. After that, the AFE converts the capacitance data from analog signal to digital signal using an analog-to-digital converter (ADC). The digital capacitance data are then delivered to the DBE. More details on the AFE will be explained in the next section.

Fig. 2.4 shows the signal processing flow in the DBE. The DBE stores each capacitance data of the TSP in the frame memory. Once the entire capacitance data are

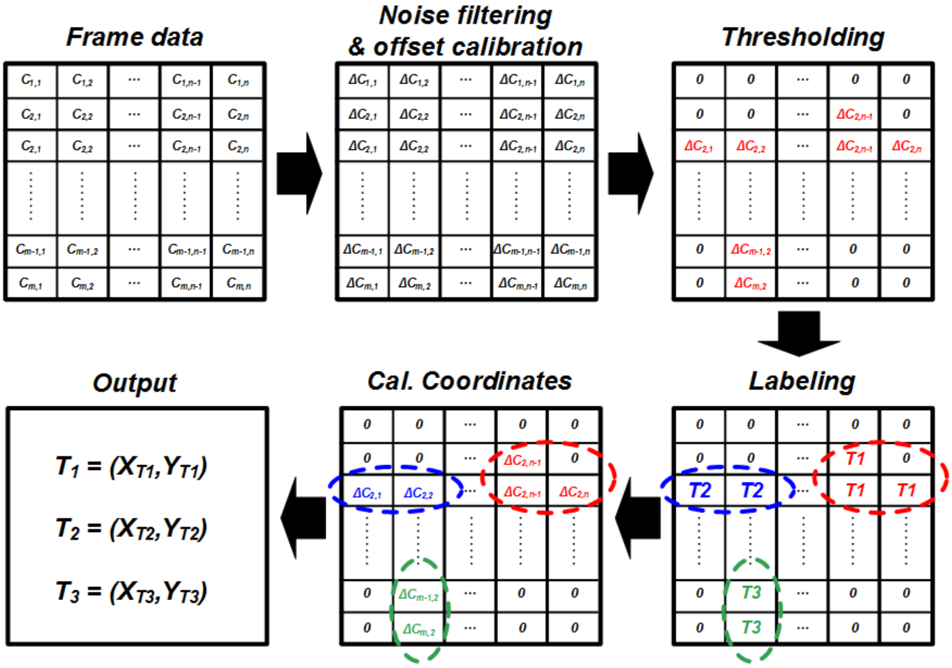

Fig. 2.4 Signal processing flow in the DBE.

acquired from the AFE, sensing of single frame data is completed. Using the frame data, the DBE performs the subsequent digital signal processing. In general, the main functions of the DBE are divided into four steps: noise filtering and offset calibration, thresholding, labeling, and firmware operations that calculate the touched coordinates by micro-controller unit (MCU). The noise filtering process provides further attenuation of the noise interference along with the offset calibration of frame data. After the calibration, the thresholding process is performed. If a capacitance value of node is smaller than a pre-determined threshold value after the offset calibration, the DBE regards the node as untouched node. Then, to reduce calculation complexity at the subsequent processes, the thresholding process makes the capacitance smaller than threshold value to zero. In the labeling process, the remaining touched nodes pair up with adjacent touched nodes in order to distinguish a large touch object. The capacitance data of each group are transferred to the MCU for calculation of the touched coordinate. Finally, the calculated touched coordinates are transmitted to the host processor.

2.3 Analog Front-End of TSC

The AFE in the TSC is core block to sense the capacitance variation of the TSP by touch input. The sensing performance of the TSC is mainly determined by the AFE. Therefore, it is important to design the AFE well for accurate detection of touch input. As described in the previous section, the main object of the AFE is sensing the mutual capacitance of each node in the TSP. Hence, the AFE is composed of two main blocks: transmitter block (TX) that applies a driving signal to the TSP and receiver block (RX) that senses the mutual capacitance modulated by the driving signal.

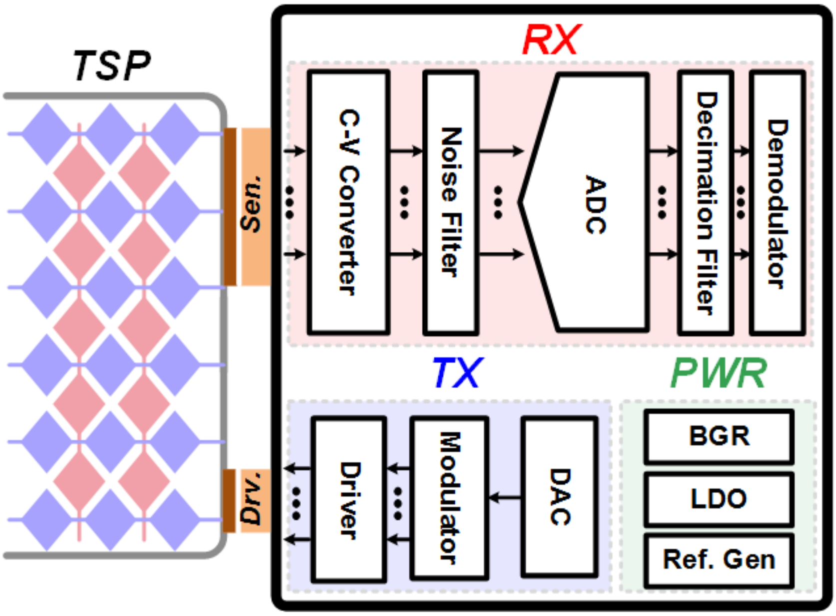

Fig. 2.5 Block diagram of the AFE.

The TX driving block usually consists of digital-to-analog converter (DAC), modulator, and driver. The DAC generates a waveform to be used as the driving signal such as sinusoidal or triangular signal. Then, the modulator encodes the waveform with a modulation sequence or performs multiplexing of the driving channels. The driver applies the modulated signal to the TSP. The parasitic capacitance of the TSP can be up to hundread-of-pF. Thus, the driver in the TX block has to provide enough driving power with consideration of the large parasitic capacitance.

The RX sensing block consists of charge-to-voltage (C-V) converter, noise filter, ADC, and demodulator unit. The capacitance signal from the TSP is charge signal that is proportional to the mutual capacitance of each node. The C-V converter then converts the charge signal to voltage signal for noise filtering and analog-to-digital conversion. After that, the noise filter suppresses the noise interference injected through the TSP. The ADC converts the analog signal to digital bitstream to deliver the capacitance data to the DBE.

2.3.1 Performance Metric

To evaluate the performance of the AFE, a number of metrics are used in the design and measurement processes. One of the most important metrics of the AFE is the signal-to-noise ratio (SNR). Because the measurement of the SNR includes both of the touch sensitivity and noise interference, the SNR well represents the performance of the AFE in the real touch environments. A certified specification or standards for measurement of the SNR have not been defined, but many works on the design of AFE for TSC use following SNR definition [2.1][2.3][2.6][2.7][2.8]. First, the touched and untouched capacitance signals can be defined as following [2.7]:

$$Signal_{Touch} = \frac{\sum_{i=1}^{100} C_{T,i}}{100},$$
$$Signal_{Untouch} = \frac{\sum_{i=1}^{100} C_{UT,i}}{100}, \tag{2.3.1}$$

where $C_{T,i}$ is capacitance of i_{th} frame with touch input and $C_{UT,i}$ is capacitance of i_{th} frame without touch input. The capacitance signal is defined as average capacitance during the measurements of 100 frames. $Signal_{Untouch}$ means the average offset of the AFE without touch input. $Signal_{Touch}$ indicates the average of touch signal along with the offset. Therefore, the capacitance difference between the touched and untouched cases is derived as following:

$$Signal_{Diff} = Signal_{Touch} - Signal_{Untouch}. \tag{2.3.2}$$

The capacitance difference $Signal_{Diff}$ means the averaged difference between the touched and untouched mutual capacitance through 100 frames. This implies the touch sensitivity and dynamic range of the AFE. Next, the noise of the sensed capacitance can be expressed as following:

$$Noise_{Touch} = \sqrt{\frac{\sum_{i=1}^{100} (C_{T,i} - Signal_{Touch})^2}{100}}. \tag{2.3.3}$$

Hence, the noise term in the SNR is the standard deviation of the sensed capacitance. Using Eq.(2.3.2) and Eq.(2.3.3), the SNR is calculated as

$$\mathrm{SNR}\ [\mathrm{dB}] = 20\log_{10}\frac{Signal_{Diff}}{Noise_{Touch}}. \tag{2.3.4}$$

Some previous works used untouched noise [2.9], but the use of touched noise in Eq.(2.3.3) is a correct approach to calculate SNR because the signal $Signal_{Diff}$ is only validate with touch input.

Another important performance metric of the AFE is frame rate. The frame rate of the AFE indicates a time step that all mutual capacitances in the TSP are sensed completely. The frame rate is also known as scan rate or refresh rate. In many applications, the TSC is required to support frame rate of at least 100 Hz. The response time can be varied depending on the implementation of the DBE, but the frame rate of the TSC is mainly determined by the AFE.

The noise immunity is another important specification for the AFE. As mentioned before, many noise sources affect the capacitance signal via the TSP. Thus, it is required for the AFE to maintain high SNR even if the noise interference is injected through the TSP. The noise immunity will be further discussed in Chapter 4.

Other specifications such as accuracy or precision are also important. But, those specifications are mainly determined by the SNR of the AFE. For this reason, the design target of the AFE focuses on the SNR, frame rate, noise immunity, and power consumption.

2.3.2 Design Issues of AFE

The SNR of the AFE greatly affects the performance of the TSC. When the AFE does not provide a sufficient SNR, many problems can occur. Fig. 2.6 shows the accuracy and precision issues by low SNR. The small capacitance variation or large noise interference obstructs the coordinate calculation, resulting in significant jitter and offset of the calculated coordinates. The jitter and offset indicates low accuracy

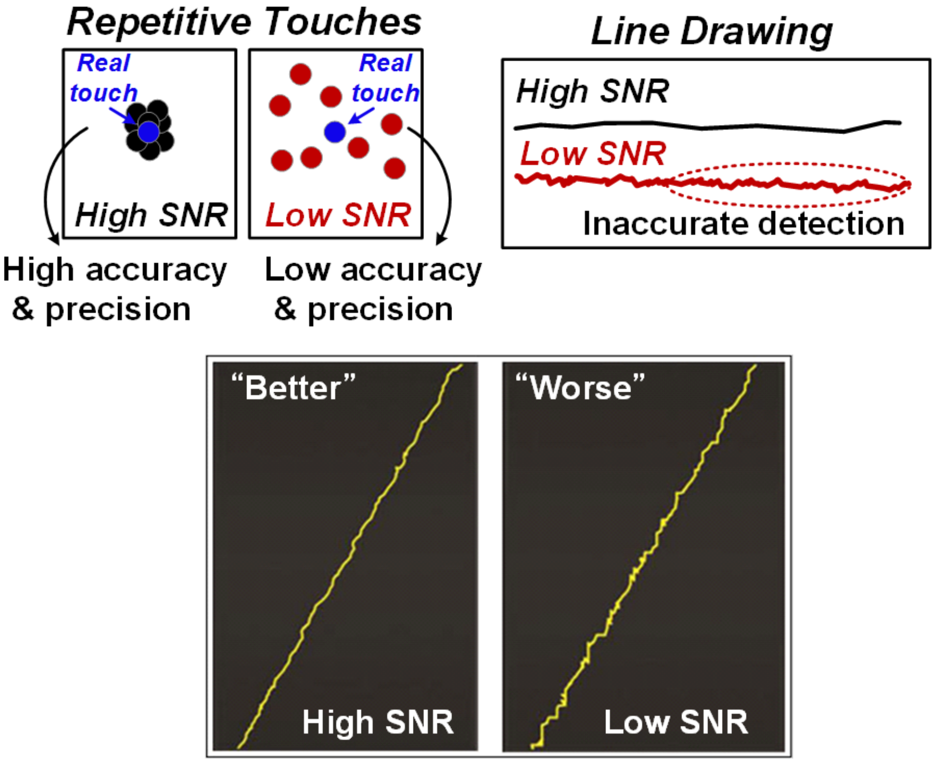

[Source : Maxim]

Fig. 2.6 Accuracy and precision issues by SNR (top) and comparison between high SNR and low SNR through the line drag test [2.10] (bottom).

and precision. The low SNR also causes inaccurate detection of line drawing. As shown in Fig. 2.6, the line drawing result with low SNR is more inaccurate than that of the high SNR case. Therefore, it is important for the AFE to achieve high SNR.

The required frame rate is usually about 100 Hz. However, as increasing the size of TSP, the number of nodes to be sensed by the AFE is also increased. Thus, the satisfaction of the required frame rate becomes more and more difficult. When the frame rate of the AFE is too low, the TSC fails to provide continuous touch detection. Fig. 2.7 shows the low frame rate issue, which results in discontinuous touch detection. At the edge of drawing, the TSC with low frame rate shows the sparse tracking points, and this causes inaccurate drawing or false gesture recognition. Thus, even if the size of TSP is increased, the AFE has to maintain the frame rate of about 100 Hz.

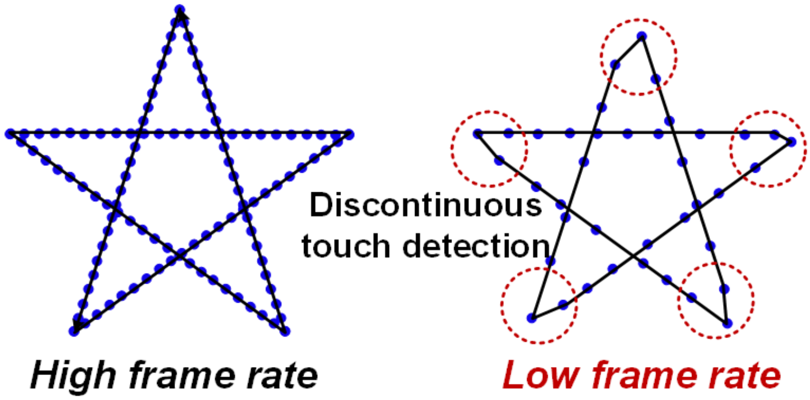

Fig. 2.7 Discontinuous touch detection by low frame rate.

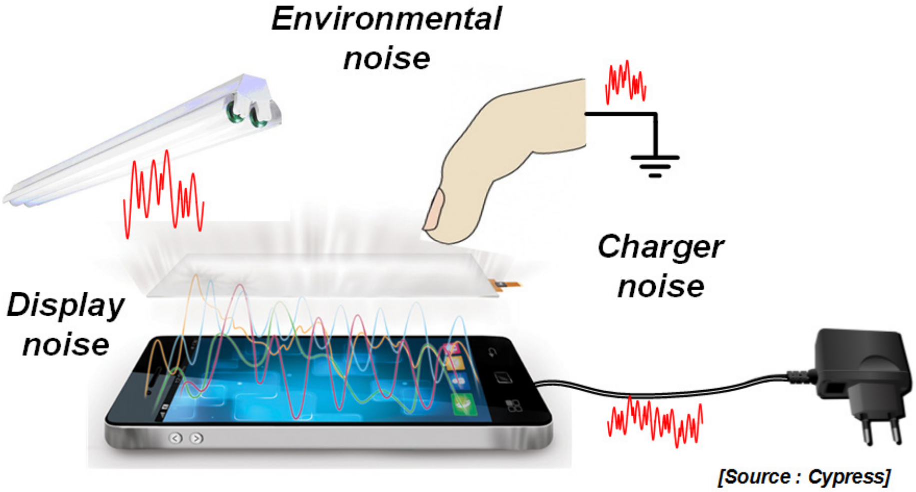

Fig. 2.8 Noise sources that affect touch detection via the TSP [2.11].

The prior works did not cover the noise immunity of the AFE in depth because the measurement of the AFE was usually done in the noise-free environment. However, the TSC is very vulnerable to the noise interference in the real environment. As shown in Fig. 2.8, the major noise sources that affect the touch sensing are display, charger, and environmental noise like lamp. Because the interference from the major noise source overwhelms the capacitance variation by the touch input, the AFE has to be immune to such noise interference. More details on the noise sources and noise filtering techniques will be explained in Charter 4.

Chapter 3

AFE of Mobile TSC with Configurable SNR and Frame Rate

3.1 Overview

With the rising demand for intuitive user interfaces in mobile devices, the mutual capacitive touch-screen sensor has become a mainstream input device. The mutual-capacitive TSP is composed of driving-channel and sensing-channel layers, which are implemented with a transparent electrode. As the form factor of mobile devices is reduced, the TSPs also become thinner by embedding the electrode layers into the cover glass or display. The reduced thickness of the TSPs, however, causes increased display noise interference due to the large coupling capacitance with the display. In addition, the TSPs are vulnerable to external interference from fluorescent lamp noise or human noise [3.1]. Environmental noise that is coupled through touched object such as charger noise [3.2] or HUM noise [3.1] also seriously affects the TSP. Therefore, the readout IC for the TSPs has to be immune to such noise interference and enhance touch sensitivity in order to achieve a high SNR. Along with an increased pixel density and size of the display, a high frame rate is also essential for the AFE [3.1].

Another requirement on the AFE is a capability of adjusting its SNR or frame rate depending on user environment or applications. The reconfiguration capability enables robust touch detection and application-specific operation. When strong noise interference from the charger is detected, the AFE increases its SNR to prevent incorrect touch detection [3.5]. On the contrary, in handwriting applications, the AFE is required to increase its frame rate to support fast touch detection and extended gesture recognition.

This chapter describes the design of a column-parallel high-SNR AFE for a mutual-capacitive TSP, which was presented in [3.3]. The TSP AFE in this work employs four techniques that mitigate the noise interference to achieve a high SNR. First, a lock-in sensing architecture is used for robustness to external noise and accurate sensing. Second, this work takes advantage of a band-pass filtering effect by the TSP and charge amplifier to suppress the TSP-induced noise. Third, a differential sensing scheme is adopted to enhance the touch sensitivity and to reject a common-mode noise. Finally, a column-parallel incremental ΔΣ ADC is employed to provide not only high frame rate and resolution but also a multiple sampling and averaging effect that further improves the noise immunity. In addition, the AFE reconfigures its frame rate and SNR according to the required touch performance by exploiting the configurable resolution of the ADC. Among the adopted techniques, this chapter mainly describes the configurable SNR and frame rate. The details of the circuit implementation are referred in [3.3].

Note that most of contents in Chapter 3 comes from [3.3][3.6]. Hence, even if the reference marks of [3.3][3.6] are not shown in this chapter, the descriptions, figures and other contents clearly come from [3.3][3.6]. It is noteworthy that the AFE described in this chapter is revised and improved from the works in [3.7]-[3.9]. Some contents in this chapter are brought from the previous works [3.7]-[3.9] without the reference marks for straightforward description. Hence, note that the contents in this chapter also come from the works in [3.7]-[3.9]. It is also noteworthy that the performance of the AFE in [3.3][3.6] was clearly improved from [3.7]-[3.9] and the main idea of the configurable SNR and frame rate was newly proposed in [3.3][3.6]. Therefore, it is evident that the work in this chapter that introduces the configurable SNR and frame rate is different from [3.7]-[3.9].

3.2 System Architecture

Fig. 3.1 shows the block diagram of the AFE. The TSP comprises multiple driving and sensing channels that are implemented with transparent electrodes such as indium-tin-oxide (ITO). The mutual capacitance C_M is a parasitic capacitance that forms between the driving channel and the sensing channel. When finger or conductive object touches the TSP, C_M is reduced, and the AFE detects the touch input by sensing the variation in C_M. To sense C_M, the AFE applies an excitation signal into each driving channel. The excitation signal is applied to only one driving channel at a time, whereas the other driving channels are shorted to ground to block the display noise interference. The excitation signals modulated by C_M are transferred to the AFE through the sensing channels of the TSP.

The column-parallel charge amplifier of the AFE converts the modulated signals of the sensing channels to voltage signals that have amplitudes proportional to the

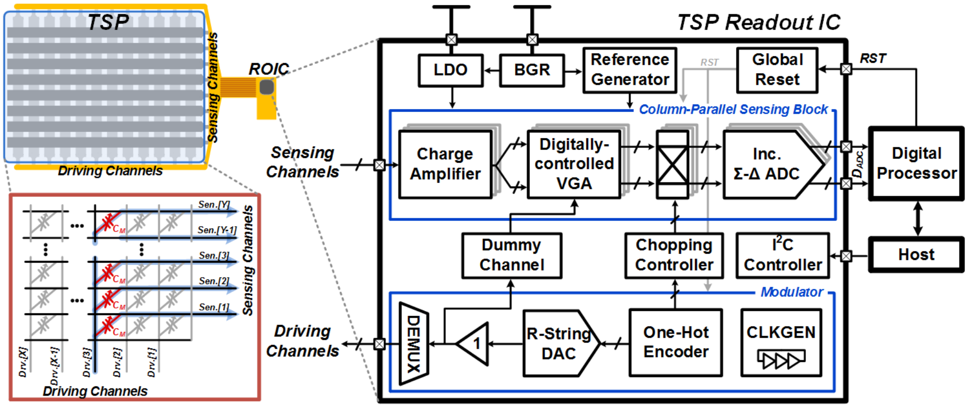

Fig. 3.1 Block diagram of the AFE in [3.3].

mutual capacitance C_M of each node. The difference between two adjacent charge-amplifier outputs is amplified by the digitally-controlled variable-gain amplifier (DVGA). A dummy channel is added to support palm detection. The chopper demodulates the DVGA output with the chopping signal generated from the modulator, and the chopping controller digitally adjusts the phase of the chopping signal.

After demodulation, the incremental ΔΣ ADCs convert the demodulated signals to digital bit streams. Previous works for TSP AFEs employed a multiplexed-ADC structure for low-power consumption and area efficiency [3.10]-[3.14]. However, in terms of the frame rate and noise performance of the TSP AFE, a column-parallel ADC offers attractive features. With the column-parallel sensing structure, the frame rate of the AFE becomes independent of the number of sensing channels, and a complex timing circuit for the multiplexer [3.11] is not required. In addition, the bandwidth requirement of the ADC can be relaxed, and it provides a good trade-off with the noise performance. For these reasons, this work adopts the column-parallel incremental ΔΣ ADCs.

The digital bit streams of the column-parallel ADC outputs are then decimated to digital values that represent the variation in C_M. Finally, the decimated data are integrated to restore the capacitance of each node at the digital processor. Gesture recognition and coordinate extraction can be performed in the digital processor. The communication between the host and the AFE is performed via the I2C controller. This work employs a low-drop-out regulator (LDO) and band-gap reference (BGR) to support a wide supply range while maintaining the regulated internal supply of 1.8 V. The reference voltages and bias currents used in the sensing blocks and the modulator are generated from the reference generator.

3.3 Configurable SNR and Frame Rate

A simplified noise model of the charge amplifier is established in Fig. 3.2(a) to investigate the noise effect by the external noise sources and the charge amplifier [3.22]. The external noise interfered with the TSP is approximated by white noise for the sake of simplicity, and the charge-amplifier noise to be considered here is the thermal noise. $\overline{v^2{}_{n,ext,i}}$ indicates the external noise sources induced through the coupling capacitor $c_{n,ext,i}$. $\overline{v^2{}_{n,ref}}$ is the reference noise of the charge amplifier, and $\overline{v^2{}_{n,OTA}}$ is the input-referred noise of the OTA. $\overline{v^2{}_{n,R1}}$ is the noise of R_{FB}. The output-referred noise power of the charge amplifier is given by

$$\overline{v^2{}_{n,CA}} \approx k^2{}_{ref}\overline{v^2{}_{n,ref}} + k^2{}_{OTA}\overline{v^2{}_{n,OTA}} + k^2{}_{R1}\overline{v^2{}_{n,R1}} + \sum_i k^2{}_{ext,i}\overline{v^2{}_{n,ext}} \tag{3.3.1}$$

where k coefficients are provided in and A_V is open-loop gain of the OTA. The

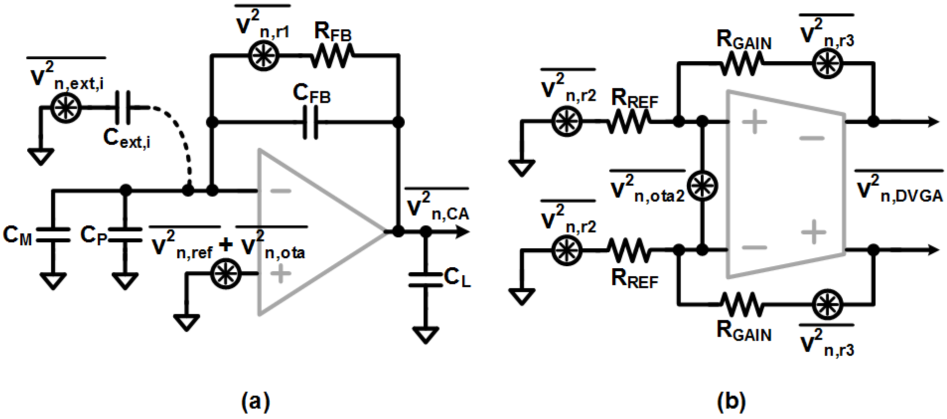

Fig. 3.2 Equivalent noise models of the (a) charge amplifier and (b) DVGA in [3.3].

Table 3.1 Noise coefficients.

${k^2}_{ref}, {k^2}_{OTA}$	$\left(\dfrac{C_P + C_{FB}}{C_{FB} + \dfrac{1}{A_V}(C_P + C_{FB})}\right)^2$
${k^2}_{ext,i}$	$\left(\dfrac{C_{ext,i}}{C_{FB} + \dfrac{1}{A_V}(C_P + C_M)}\right)^2$
${k^2}_{R1}$	$\left(\dfrac{1}{2\pi f R_{FB}(C + \dfrac{1}{A_V}C_P)}\right)^2$

noise contribution of the feedback resistor R$_{FB}$ is low-pass filtered by R$_{FB}$ and C$_{FB}$. The effects of $\overline{{v^2}_{n,ref}}$ and $\overline{{v^2}_{n,OTA}}$ are determined by the ratio between C$_P$ and C$_{FB}$. In case of the mutual-capacitive TSP, C$_P$ is much greater than C$_{FB}$ because the mutual capacitances of the inactivated driving channels behave as a parasitic capacitance. Therefore, $\overline{{v^2}_{n,ref}}$ and $\overline{{v^2}_{n,OTA}}$ are amplified and significantly affect the charge-amplifier output. For this reason, the OTA should be designed to minimize $\overline{{v^2}_{n,OTA}}$, and $\overline{{v^2}_{n,ref}}$ must be rejected by the differential sensing scheme. The contribution of the external noise source is dependent on C$_{FB}$ and C$_{ext,i}$. As the distance between the noise source and the TSP decreases due to the thin form factor, C$_{ext,i}$ increases, and the noise interference becomes worse. In the time domain, the output of the charge amplifier with the external noise sources can be calculated as follows:

$$V_{CA}(t) = -\frac{C_M}{C_{FB}}V_{EX}(t) - \sum_i \frac{C_{ext,i}}{C_{FB}}V_{n,ext,i}(t). \qquad (3.3.2)$$

where $V_{EX}(t)$ is the excitation signal, and $V_{n,ext,i}$ is the i$_{th}$ external noise source.

Eq.(3.3.1) and Eq.(3.3.2) show that larger value of C_{FB} and amplitude of V_{EX} have better noise immunity against the external noise interference. Therefore, this work sets the amplitude of the excitation signal to be as large as possible within the external supply voltage, and C_{FB} is set to approximately three times the value of C_M.

The common-mode rejection of the differential sensing scheme suppresses the reference noise of the charge amplifier and the common external noise such as the display noise. Fig. 3.2(b) shows the equivalent noise model of the DVGA, where the thermal noise is the dominant source. $\overline{v^2_{n,OTA2}}$ indicates the input-referred noise of the DVGA. $\overline{v^2_{n,R2}}$ is the noise of R_{REF}, and $\overline{v^2_{n,R3}}$ is the noise of R_{GAIN}. The output-referred noise of the DVGA, $\overline{v^2_{n,DVGA}}$, is calculated from Eq.(3.3.1) as follows:

$$\overline{v^2_{n,DVGA}} \approx 2G^2_{DVGA}(k^2_{OTA}\overline{v^2_{n,OTA}} + k^2_{R1}\overline{v^2_{n,R1}} + \overline{v^2_{n,R2}} + \frac{1}{CMRR^2}(k^2_{ref}\overline{v^2_{n,ref}} + \sum_i k^2_{ext,i}\overline{v^2_{n,ext,i}}) + \frac{1}{2}\overline{v^2_{n,OTA2}}) + 2\overline{v^2_{n,R3}} \qquad (3.3.3)$$

where CMRR is the common-mode rejection ratio of the DVGA. The reference noise of the charge amplifier and the external noise induced though the TSP are canceled out by the differential sensing scheme, and the AFE achieves high immunity to the external noise and the reference noise. It is noted that G_{DVGA} increases the touch sensitivity, whereas $\overline{v^2_{n,OTA2}}$, $\overline{v^2_{n,R1}}$, and $\overline{v^2_{n,R2}}$ are also amplified by the magnitude of G^2_{DVGA}. However, the mismatches of the DVGA can degrade the noise immunity resulting from the decreased CMRR. Fig. 3.3 shows the Monte Carlo simulation results with 500 trials. For mismatches of the devices and resistors, the DVGA achieves a sufficient CMR to attenuate the common-mode noise. Therefore, the differential sensing scheme enables the AFE to be robust to the external noise and the amplified reference noise.

Owing to the oversampling nature of the ΔΣ ADC and low-pass filtering of the decimation filter, the column-parallel incremental ΔΣ ADC provides a multiple sampling and averaging effect [3.15], which improves the noise performance of the AFE. Fig. 3.4 shows the block diagram of the equivalent noise model of the implemented ΔΣ ADC. $\overline{v^2_{n,AFE}}$ is the demodulated noise power of $\overline{v^2_{n,DVGA}}$ in Eq.(3.3.3), and $\overline{v^2_{n,ADC}}$ is the input-referred noise power of the ADC.

Because the employed CDS technique reduces the effect of the flicker noise, the thermal noise can be considered as the dominant noise source in the ADC. G_{ADC} is the effective loop gain of the ADC, and $\overline{v^2_{n,q}}$ is the quantization noise power. When the number of ADC sampling cycles is N, the i_{th} coefficient of the implemented second-order decimation filter is given by $w_i = (N-i)/(N(N+1)/2)$ [3.15]. Thus, the total noise power after decimation is calculated as follows [3.15][3.16][3.18][3.19]:

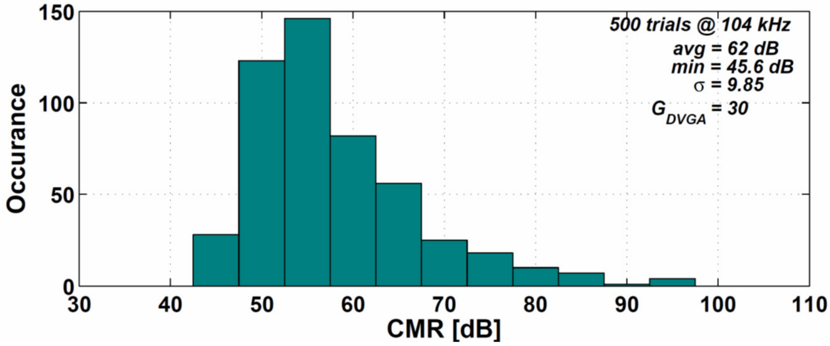

Fig. 3.3 Monte Carlo simulation results of the DVGA common-mode rejection (CMR) with 500 trials in [3.3].

$$\begin{aligned}\overline{v^2{}_{n,tot}} &= \sum_{i=0}^{N-1}\left(2\frac{N-i}{N(N+1)}\right)^2 \left(G^2{}_{ADC}\left(\overline{v^2{}_{n,AFE}}+\overline{v^2{}_{n,ADC}}\right)+\overline{v^2{}_{n,q}}\right) \\ &\approx \frac{4}{3}\left(G^2{}_{ADC}\left(\frac{\overline{v^2{}_{n,AFE}}+\overline{v^2{}_{n,ADC}}}{N}\right)+\frac{\overline{v^2{}_{n,q}}}{N}\right).\end{aligned} \tag{3.3.4}$$

The contributions of $\overline{v^2{}_{n,AFE}}$ and $\overline{v^2{}_{n,ADC}}$ are bounded to $(4/3){G_{ADC}}^2/N$ and the contribution of $\overline{v^2{}_{n,q}}$ becomes negligible as increasing *N*. Therefore, the column-parallel incremental ΔΣ ADC suppresses not only its intrinsic noise but also the demodulated input noise. It also reduces the effect of external noise that is coupled into the TSP via touch object, which cannot be rejected by the differential sensing scheme

Depending on the requirements of the application or the noise environment, either a high frame rate or a high SNR can be more desirable. In this case, the AFE is reconfigured for the desired frame rate and SNR by only adjusting the number of ADC sampling cycles *N*. The frame rate determined by the conversion time of the ADC is increased by reducing *N*. On the other hand, the SNR can be improved by increasing *N* because the total output noise power in Eq.(3.3.4) is reduced. In this way, the SNR and frame rate can be reconfigured by scaling *N*.

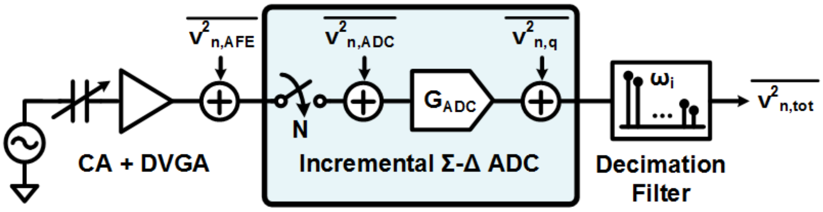

Fig. 3.4 Equivalent noise model of the incremental ΔΣ ADC with the decimation filter in [3.3].

To adjust N, this work controls the reset period T_{RST}. As the incremental ΔΣ ADC and decimation filter are reset after each conversion, N is determined by T_{RST} and sampling frequency f_s. The adjustment of f_s imposes a burden for supporting a wide operating frequency, while no additional circuit burden is placed on the adjustment of T_{RST} because the excitation and chopping signals are synchronized with the reset signal. Fig. 3.5 shows the timing diagram of scaling N according to the adjustment of T_{RST}. When a high frame rate is required, as shown in Fig. 3.5(a), T_{RST} is reduced, resulting in the increase of frame rate in accordance with the decrease in N. In contrast, if a high SNR is required, as depicted in Fig. 3.5(b), T_{RST} is increased, and the noise performance is improved in proportion to the increase. The column-parallel structure of the sensing blocks widens the scalable range of N, and this work adjusts N from 32 to 4096, which corresponds to the frame rate from 50 Hz to 6.4 kHz.

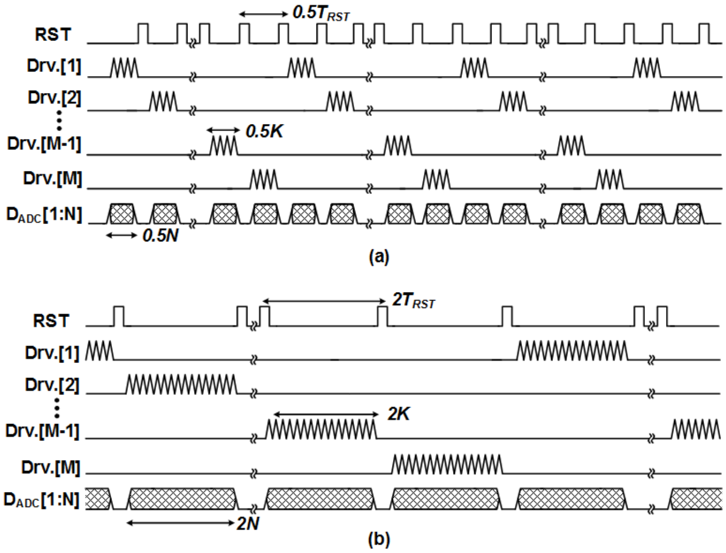

Fig. 3.5 Timing diagram for scaling the number of ADC sampling cycles in [3.3].

3.4 Measurement Results

The test chip is fabricated in a 0.18-μm CMOS process. The die micrograph of the fabricated chip is shown in Fig. 3.6. The test chip has an active area of 2.2 mm^2. The reset timing controller and decimation filter were implemented in an FPGA board. The test chip supports up to 13 driving channels and 8 sensing channels, and a 4.3-inch mutual-capacitive TSP with 12 driving channels and 8 sensing channels was used in the measurement. The touched mutual capacitance and untouched mutual capacitance of the TSP are measured to be approximately 4 pF and 4.4 pF, respectively. The test chip consumes 6.26 mW with a 3.3-V supply. The power dissipation of one channel of the sensing blocks, which consists of the charge amplifier, DVGA, chopper, and ADC is 530 μW.

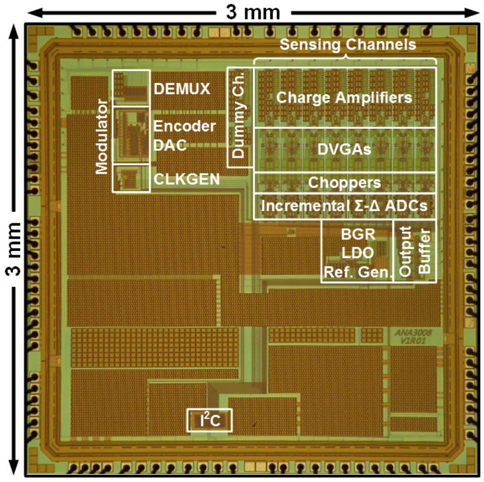

Fig. 3.6 Die micrograph of the fabricated AFE in [3.3].

Fig. 3.7 shows the measured waveforms of the charge amplifier and DVGA. The excitation signal is sequentially applied to the driving channels of the TSP, and the column-parallel charge amplifier and DVGA continuously sense the modulated excitation signal as shown in Fig. 3.7(a). After applying the excitation signal to all of the driving channels, the reset signal (RST) is activated. When the excitation signal is applied to the touched driving channel, the DVGA output has a larger output swing than that of other channels. In case of the partially touched channel, the output swing of the DVGA is smaller than that of the fully touched channel because of reduced variation in C_M. Fig. 3.7(b) shows the detailed waveforms with a touch input. The output of the charge amplifier corresponding to the touched channel, $V_{CA,Touch}$,

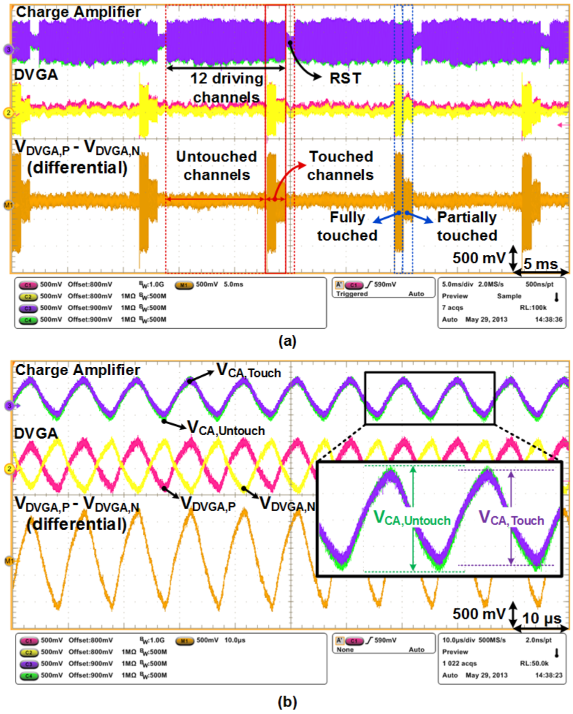

Fig. 3.7 Measured waveforms of the charge amplifier and DVGA outputs in [3.3].

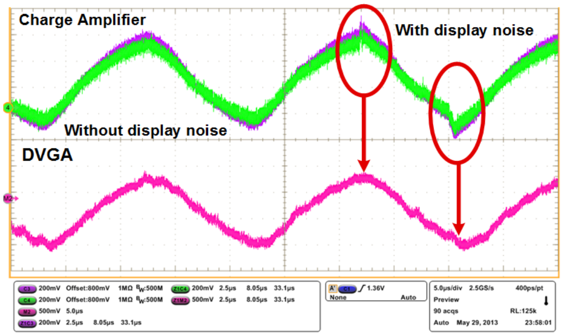

Fig. 3.8 Measured waveforms for display noise cancellation at the DVGA in [3.3].

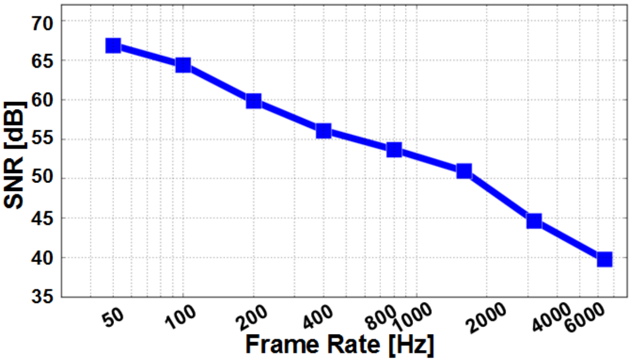

Fig. 3.9 Measured SNR versus frame rate in [3.3].

is smaller than that of the untouched channel, $V_{CA,Untouch}$. The DVGA then amplifies the difference by the magnitude of G_{DVGA}.

Fig. 3.8 shows the display noise cancellation by the differential sensing scheme. A distortion caused by the display noise appears at the outputs of the charge amplifiers. Owing to the differential sensing scheme, the display noise interference is suppressed, and the distortion disappears at the DVGA output.

Fig. 3.9 shows the measured SNR according to the frame rate. For $N = 1024$, the test chip achieves 60-dB SNR and 200-Hz frame rate. The test chip reconfigures its

SNR from 40 dB to 67 dB and its frame rate from 50 Hz to 6.4 kHz by adjusting *N*.

Fig. 3.10 shows the measured noise power versus the excitation signal swing V_{TX}. The noise power is normalized to have same touch strength for comparison. The AFE has better noise immunity as increasing $\mathrm{V_{TX}}$, and this coincides with the noise consideration in the previous section. Fig. 3.11 shows the measured SNR according to the V_{TX}. As a result, the SNR of the AFE can be improved as increasing V_{TX}, and this implies that the driving amplitude V_{TX}

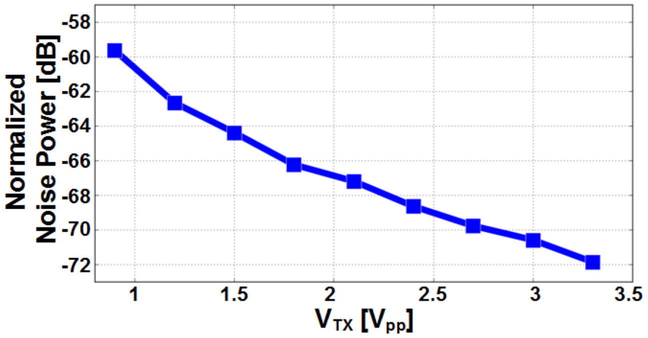

Fig. 3.10 Measured normalized noise power versus the amplitude of the TX driving signal $\mathrm{V_{TX}}$ in [3.3].

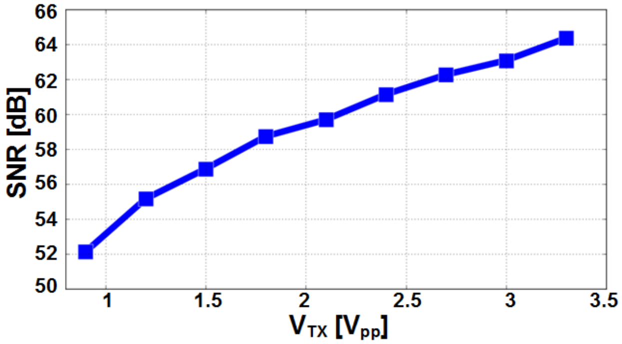

Fig. 3.11 Measured SNR versus the amplitude of the TX driving signal $\mathrm{V_{TX}}$ in [3.3].

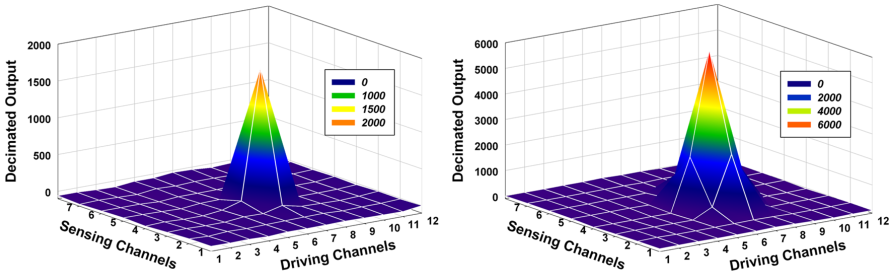

(a) 3-mm diameter metal slug **(b) 8-mm diameter metal slug**

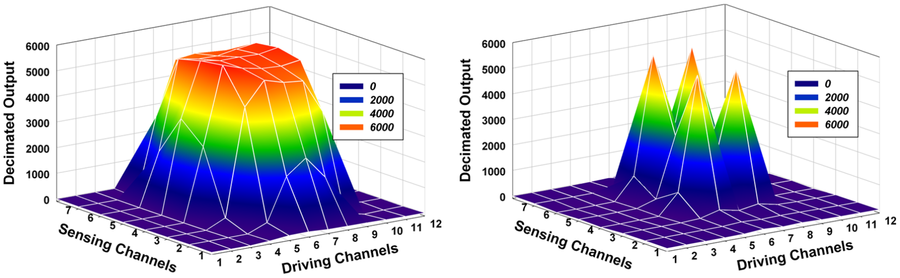

(c) 30-mm diameter metal slug **(d) four 6-mm diameter metal slugs**

Fig. 3.12 3D images of the decimated output of the AFE in [3.3].

Fig. 3.12 shows the decimated output of the test chip with different touch objects. When the TSP is touched with a 3-mm metal pillar corresponding to a stylus pen, the decimated output is depicted in Fig. 3.12(a). The output difference between the touched node and the untouched node is approximately 1800, and the measured SNR is 53 dB. When an 8-mm metal pillar touches the TSP, as shown in Fig. 3.12(b), the difference is approximately 6300, and the measured SNR is 64 dB. Fig. 3.12(c) shows palm detection with 30-mm metal pillars, and Fig. 3.12 (d) shows multi-touch detection with four 6-mm metal pillars.

Table 3.2 summarizes the performance of the AFE and provides a comparison

Table 3.2 Performance comparison in [3.3]

	T-CE 10'	ISSCC 10'	ASSCC 10'	T-CE 11'	ISSCC 12'	ISSCC 13'	ISSCC 13'	ISSCC 14'	ISSCC 14'	**This work**
Process	-	90 nm	0.18 µm	0.35 µm	90 nm	0.35 µm	0.18 µm	0.35 µm	0.18 µm	**0.18 µm**
TSP Type	Mutual	Self	Mutual	Mutual	Self	Mutual	Mutual	Dual	Mutual	**Mutual**
Channel	TX : 9 RX : 7	[1]TRX : 24	TX : 20 RX : 16	TX : 29 RX : 53	[1]TRX : 30	TX : 27 RX : 43	TX : 30 RX : 24	TX : 80 RX : 80	TX : 24 RX : 16	**TX : 12** **RX : 8**
SNR	21.3 dB	36 dB	24 dB	12.6 dB	35 dB	39 dB	55 dB	41 dB	53 dB	$N = 32$ **40 dB** $N = 1024$ **60 dB** $N = 4096$ **67 dB**
Frame Rate	-	120 Hz	65 Hz	140 Hz	120 Hz	120 Hz	240 Hz	322 Hz	160 Hz	$N = 32$ **6400 Hz** $N = 1024$ **200 Hz** $N = 4096$ **50 Hz**
Supply	-	3 V	3.3 V	3.3 V	-	3.3 V	2.5 – 3.3 V	2.6 – 3.6 V	–	**2.1 – 3.3 V**
Power	4.3 mW	12 mW	19 mW	19 mW	10.6 mW	18.7 mW	52.8 mW	21.8 mW	[3]2.6 mW	**6.26 mW**
Area	-	3.65 mm^2	[4]4 mm^2	-	6.87 mm^2	[4]10.4 mm^2	14.8 mm^2	13.7 mm^2	[4]0.46 mm^2	**[4]2.2 mm^2**

[1] TRX = TX + RX (Self-capacitive TSP).
[2] N = The number of ADC sampling cycles.
[3] Only RX power consumption.
[4] Active area.

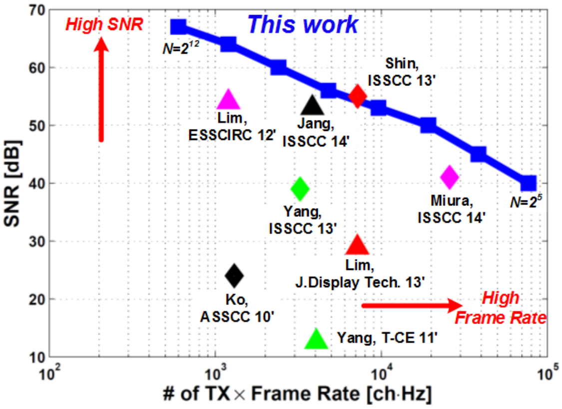

Fig. 3.13 Measured SNR versus product of the number of TX channels and the frame rate in [3.3].

with previously published works for mobile devices. In order to compare the SNR and frame rate under the same condition, a product of the number of TX channels and the measured frame rate is used as shown in Fig. 3.13. Owing to the column-parallel sensing structure, the SNR and frame rate of this work are affected by only the number of TX channels.

Chapter 4

AFE of Tablet TSC with Enhanced Noise Immunity

4.1 Overview

As increasing use of smartphones and tablet PCs, touch screen becomes main input devices as human-machine interface in these days. Owing to intuitive interface and various gesture recognitions, the touch screen has increased their applications. Besides the smartphones or tablet PCs, home appliances, such as television or refrigerator, or control system of smart cars also use the touchscreen as the input devices instead of conventional push button.

With the increased applications and advance of display, the touch screen becomes larger than 10 inch. For example, many of the tablet PCs in these day have touch screen larger than 12 inch. In case of smart cars, they employ touch screen larger than 15 inch for controlling most of the car’s control function. Therefore, touch-screen panel (TSP), which is a sensor of the touch screen, also becomes larger than 10 inch and has a number of nodes to be sensed. For this reason, touch controller for the large-size TSP has to sense much more capacitance data than that of the small-size TSP. The sensing complexity of the touch controller is increased, but the requirements of signal-to-noise ratio (SNR) or frame rate remain same with those of the touch controller for the smartphones. Therefore, design of analog front-end of the touch controller that provides the required performances and the large sensing capacity becomes more and more hard.

In addition to the large-size TSP issue, noise interference injected through the TSP remains problem for the touch controller [4.1]-[4.4]. The noise sources that mainly affect the capacitance sensing are display, lamp, and charger noise. The lamp noise, which comes from fluorescent lamp or three-wavelength lamp, locates below 50 kHz. Thus, high frequency driving signal and low-pass filter can help reject the lamp noise. As form factor of the devices becomes thinner, the display noise coupled through the TSP gets worse. The frequency of the display noise usually locates in the range from 10 to 100 kHz. In case of in-cell or on-cell TSP, the display noise affects the touch sensing severely.

The charger noise results from common-mode supply noise of the charger [4.3][4.4]. When charger provides supply to the touch controller, the voltage difference between VDD and GND is maintained, but the common-mode voltages of VDD and GND are seriously fluctuated over 10 V_{pp}. Therefore, difference between ground of touch object and the charger due to the common-mode noise makes large peak-to-peak noise that is injected to the TSP via the touch object. Compared to the lamp noise or the display noise, the charger noise shows large peak-to-peak noise and wide-band frequency distribution. Furthermore, the charger noise is locally injected through touch object, being hard to suppress using the differential sensing method.

In this chapter, highly noise-immune AFE is described with configurable SNR and frame rate [4.5]. The proposed AFE supports up to 100 TRX channels, which can cover up to 15.6-inch TSP. In order to enhance the noise immunity, a number of techniques have been employed. The TX driving block employs a multi-driving TX structure that improves the SNR. The RX sensing block adopts high-order noise filtering structure along with pre-filtering differential sensing method. The detailed explanation about the proposed AFE is described in the following sections.

It is noteworthy that most contents of this chapter were presented in [4.5]. For the sake of simplicity, the reference mark of [4.5] can be omitted in the following sections.

4.2 Design Issues by Large-Size TSP

The target number of the TSP channels of this work is 36 TX channels and 64 RX channels, which corresponds to 12.2-inch TSP used in the measurements. Compared to the AFE for the smartphone TSC described in Chapter 3, the number of nodes in the TSP is multiplied by 24 times. Likewise, as increase the size of TSP, the number of nodes to be sensed by the AFE is also increased. Fig. 4.1 shows the increase of capacitance nodes depending on the TSP size. The 5.9-inch TSP for smartphone TSC has capacitance about 500, but the 12.2-inch TSP for tablet TSC has capacitance nodes more than 2300. Hence, the AFE for the large-size TSP processes capacitance nodes more than five times compared to the AFE for the

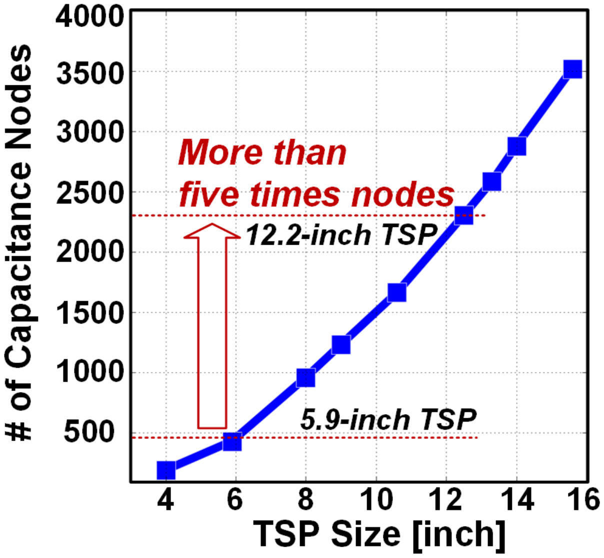

Fig. 4.1 The number of capacitance nodes versus size of TSP.

smartphone-size TSP, but the frame rate to be provided by the AFE is same as 100 Hz. Furthermore, the SNR specification of the large-size TSP is also same with that of the smartphone TSP. As a result, the AFE of the large-size TSP provides equal performance with capacitance data more than five times than that of the AFE for the smartphone TSC.

4.3 Design Issues by Noise Interference

4.3.1 Noise Interference

As briefly explored in Chapter 2, the TSP is vulnerable to external noise interference. Among a number of noise sources, the charger is the most significant noise source. Fig. 4.2 shows the charger noise injection model. The charger noise results from the different ground between the touch object and AFE. The charger delivers supply voltage and ground. Although the voltage difference between supply (VDD) and ground (GND) is constant, the common-mode noise exists between VDD and GND. The operation of the AFE without touch input is not affected by the common-mode noise of the charger. However, when touch input is applied to the TSP, the ground difference between touch object and AFE acts as noise source. It is equivalent to inject the common-mode noise of the charger through the touch object. Be-

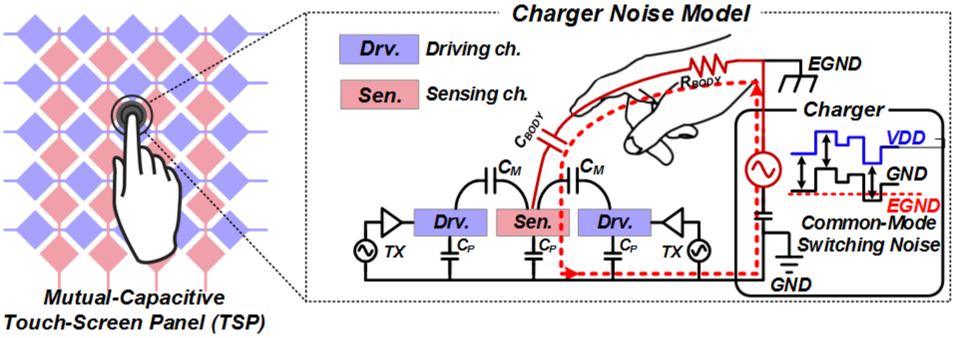

Fig. 4.2 Charger noise injection model.

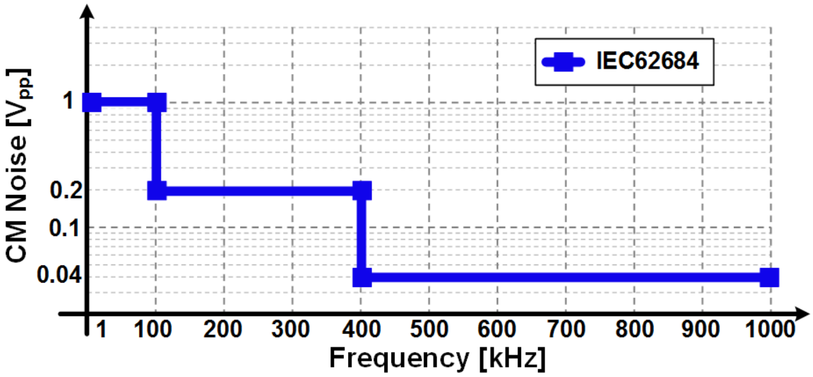

Fig. 4.3 IEC 62684 specification in [4.3].

cause the common-mode noise can be larger than 10 V_{pp} [4.2], the noise interference by the charge noise significantly affect the capacitance signal.

Fig. 4.3 shows the standards of the common-mode voltage specified by IEC 62684 [4.3]. According to IEC 62684, the charger has to provide acceptable common-mode noise of up to 1 V_{pp} in the frequency lower than 100 kHz. More relaxed specifications are applied to the frequency higher than 100 kHz. Although the IEC 62684 standard [4.3] has been presented, many manufactures of the charger do not follow the standard due to cost issue. In reality, the common-mode noise can exceed 10 V_{pp} in some non-certified chargers. Therefore, the AFE has to be capable of attenuating the charger noise in case the charger generates the severe common-mode supply noise. There are other noise sources that are injected through the touch object and distort the capacitance signal, but they can be also modeled as same with the charger noise injection model in Fig. 4.2. Therefore, those noise interferences can be dealt in the same manner with the charger noise.

The display noise is another severe noise source that distorts the capacitance signal. As the distance between the TSP and display becomes narrow by embedding the

TSP into the display, the coupled display noise into the TSP is also increased. Fig. 4.4 shows the display noise injection model. The display noise mainly results from VCOM in the display. Because the VCOM is inverted periodically, the VCOM acts as the noise source to the TSP. On the contrary to the charger noise, the VCOM noise affects all nodes in the TSP. Therefore, the display noise can be regarded as common-mode noise. In other words, the display noise affects the TSP regardless of the touch input. Using this feature, the rejection methods of the display noise have been investigated as in . The display noise rejection techniques in the prior works are covered in the next section.

In summary, the display noise is common-mode noise that affects all TSP nodes. Even if the noise amplitude is smaller than that of the charger noise, the distortion by the display noise is also significant due to the large coupling area. The noise model of other noise sources that affect the TSP commonly is same with the model in Fig. 4.4. Hence, they can be regarded as the common-mode noise like the display noise.

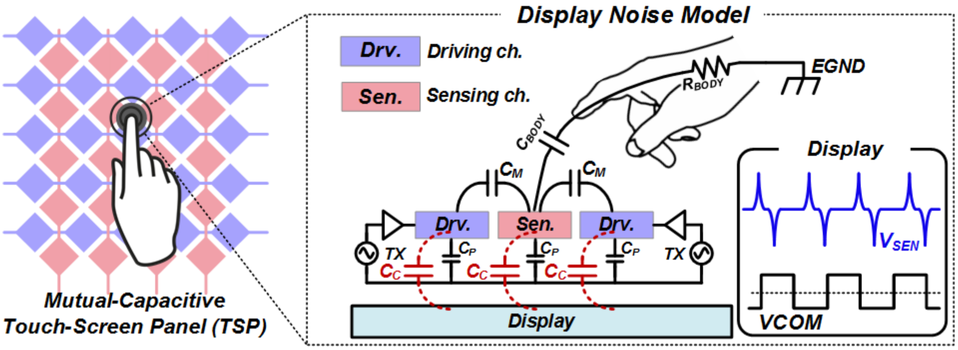

Fig. 4.4 Display noise injection model.

4.3.2 Display Noise Rejection Technique

To attenuate the display noise interference, the differential sensing technique has been widely used [4.1][4.2][4.6][4.8][4.14][4.15]-[4.19]. The differential sensing technique is based on the assumption that all electrodes of the TSP are equally affected by the display noise. In other words, a coupling capacitance $C_{C,display}$ between the display and TSP and noise interference $V_{n,display}$ can be regarded as same at each node in the TSP. Therefore, the display noise can be considered as a common-mode noise. Depending on the sequence of performing subtraction process, the differential sensing method can be categorized into two methods: pseudo-differential sensing and fully differential sensing method.

The pseudo-differential sensing method performs the differential sensing after the charge-to-voltage conversion or additional filtering. The previous works [4.1][4.2][4.6] [4.15]-[4.19] used the pseudo differential sensing method to reject the display noise. As shown in Fig. 4.5, the charge amplifier converts the capacitance signal at first, and then the differential gain amplifier performs the differential sensing. One of the advantages of the pseudo differential sensing is that a column-parallel sensing structure for improving SNR can be implemented at the same time [4.19]. When the pseudo differential sensing method is employed, the capacitance signal with display noise interference can be modeled simply as following [4.15]:

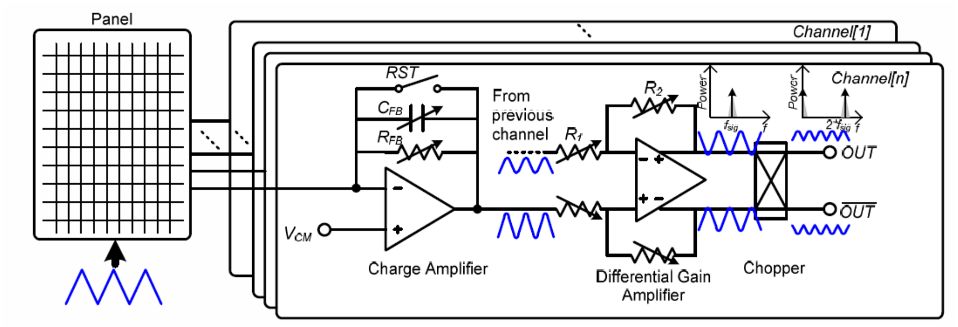

Fig. 4.5 The pseudo differential sensing method in [4.17].

$$V_{CA,1}(t) \approx \frac{C_{M,1}V_{TX}(t)+C_{C,1}V_{n,display}(t)}{C_{FB}}. \tag{4.3.1}$$

$$V_{CA,2}(t) \approx \frac{C_{M,2}V_{TX}(t)+C_{C,2}V_{n,display}(t)}{C_{FB}}. \tag{4.3.2}$$

Using Eq.(4.3.1) and Eq.(4.3.2), the output voltage of the differential sensing can be derived as following [4.15]:

$$\begin{aligned} V_{diff,p}(t)-V_{diff,m}(t) &= G_{diff}(V_{CA,1}(t)-V_{CA,2}(t)) \\ &\approx G_{diff}\frac{(C_{M,1}-C_{M,2})V_{TX}(t)}{C_{FB}}, \end{aligned} \tag{4.3.3}$$

where G_{diff} is the closed-loop gain of the differential amplifier. According to Eq.(4.3.3), the differential sensing method can cancel out the display noise $V_{n,display}$ effectively. However, the display noise rejection of the pseudo differential sensing is limited to the mismatches of the charge-to-voltage conversion blocks such as charge amplifier and the closed gain of the differential sensing amplifier.

For those reasons, the fully differential sensing method was proposed in [4.8][4.14]. The main difference between the pseudo differential sensing and the fully differential sensing is the sequence of sensing the capacitance signal. In case of the pseudo differential sensing method, the charge-to-voltage conversion is performed ahead of the differential sensing. In contrast, in the fully differential sensing method, the differential sensing is performed simultaneously with the charge-to-voltage conversion. As shown in Fig. 4.6, the charge integrator is implemented with fully differential structure. Since the mismatches of the fully differential charge integrator or charge amplifiers affect the degradation of the display noise rejection, the fully differential sensing method is superior to the pseudo differential sensing method inherently in terms of the display noise rejection. When the fully differential sensing method is employed, the capacitance signal with display noise interference can be modeled simply as following:

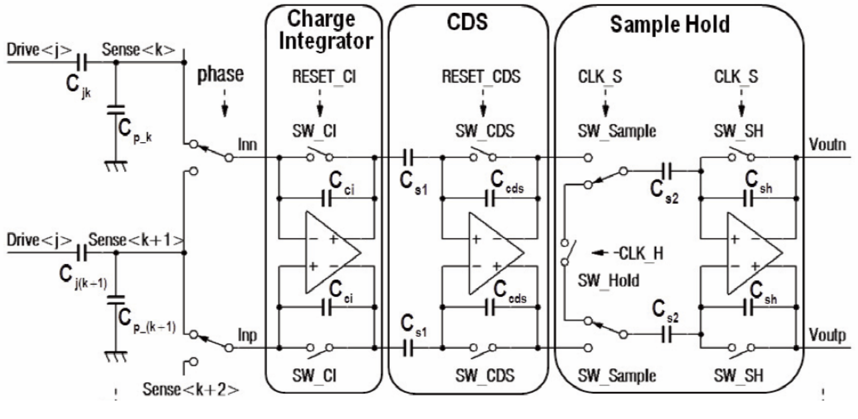

Fig. 4.6 The fully differential sensing method in [4.8]

$$
\begin{aligned}
V_{outp}(t) - V_{outm}(t) &\approx \frac{(C_{M,1} - C_{M,2})V_{TX}(t)}{C_{FB}} \\
&+ \frac{(C_{C,1} - C_{C,2})V_{n,display}(t)}{C_{FB}} \\
&= \frac{(C_{M,1} - C_{M,2})V_{TX}(t)}{C_{FB}}.
\end{aligned}
\tag{4.3.4}
$$

According to Eq.(4.3.4), the fully differential sensing method can cancel out the display noise $V_{n,display}$ as same with Eq.(4.3.3), but the gain of the capacitance signal is only determined by the feedback capacitance C_{FB}.

The fully differential sensing method provides better display noise rejection, but it has drawback that the column-parallel structure cannot be implemented with the fully differential sensing method. Hence, a multiplexing of RX sensing channel [4.8][4.14] is required to the fully differential sensing, and this may degrade the overall performance such as SNR or frame rate.

4.3.3 Charger Noise Filtering Technique

The charger noise is the worst noise source that affects the touch screen sensor. As described in the previous section, the charger delivers critical noise interference larger than 10 V_{pp}. Even worse, the frequency of the charger noise can be overlapped with the frequency of the TX driving signal. Hence, it is very difficult to maintain the touch sensing performance with existence of the charger noise interference.

One of the approaches to attenuate the charger noise is a charge interpolation integrator described in [4.2]. According to the description in [4.2], the charge interpolation integrator is composed of the phase-delay cell (PDC), noise-detecting cell (NDC), and the charge-memory cell (CMC) as shown in Fig. 4.7. When the NDC detects the charger noise interference, the PDC stops to deliver the received charge signal to the integrator. At this time, the CMC generates the charge signal that is interpolated from the stored previous charge signal, and the interpolated signal is transferred to the integrator.

The charge interpolation method in [4.2] prevents the charger noise signal to be integrated, but it has some critical drawbacks. First, the charger noise interference occurs only when the touch input is applied. Therefore, the charger noise interference is injected with the touch input at the same time. At this time, the stored charge signal in the CMC is the charge signal without touch input, and it cannot represent

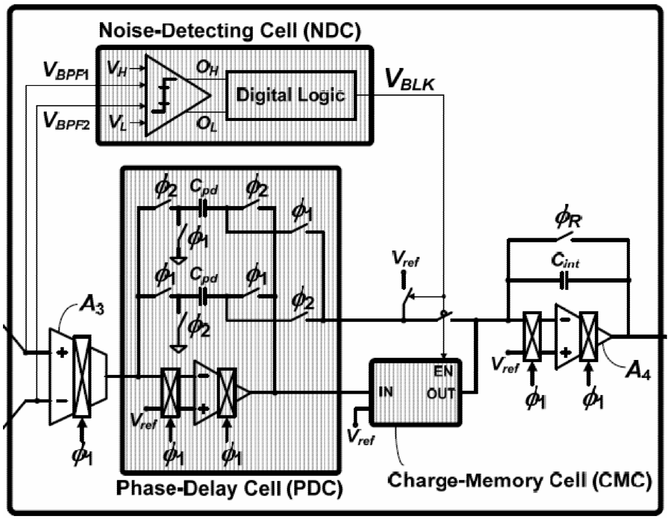

Fig. 4.7 The charge interpolation integrator in [4.2]

the touched charge signal. As a result, the interpolated charge signal is hard to recover the charge signal with touch input, and the touch controller cannot detect the touch input with charger noise interference. Second, the charge interpolation can distort the differential sensing signal. In order to restore the capacitance from the differentially sensed signal, the amplitudes of the positive differential signal and the negative differential signal have to be matched accurately. However, the charge interpolation can distort the balanced differential signal. The interpolation requires sample and hold process of the previous charge signal, and the charge loss of the sampling capacitor is inevitable, resulting in the imbalance of the differential signal.

Another approach to reduce the charger noise interference is a non-linear filtering in the digital domain as described in [4.21]. According to the description in [4.21],

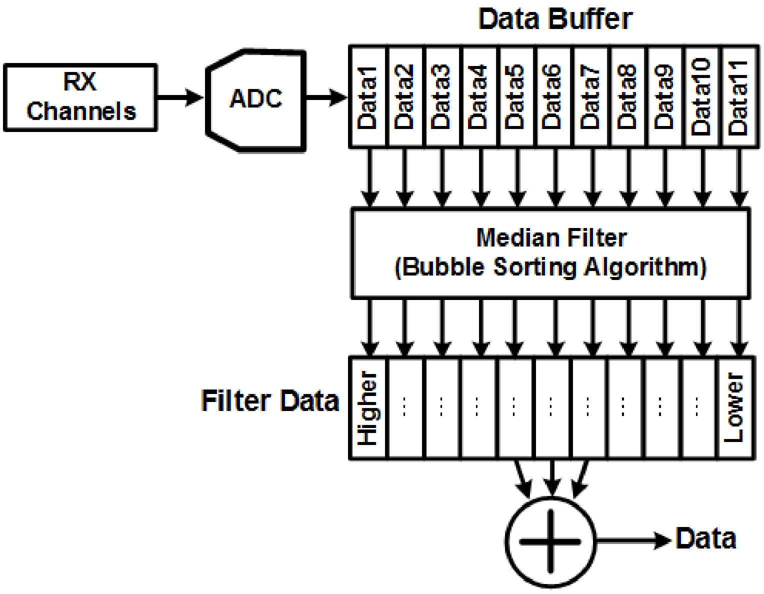

Fig. 4.8 Digital non-linear filtering for charger noise rejection in [4.21]

the digital block contains a number data buffer that stores the capacitance signal sensed by the RX sensing blocks. Then, the non-linear filter, such as median filter, sorts the data in the data buffers. Among the arranged data, the smallest data and the largest data are discarded, and the other data are averaged. Using this sequence, the influence of the charger noise interference can be reduced.

However, this non-linear filtering process in the digital domain has some problems. First, the data buffer requires large chip area. Although the smartphone TSP has small number of nodes less than 1000 nodes, the tablet TSP has many nodes larger than 2000 nodes. Thus, it is difficult to store a number of frame data, and this restricts the performance of the non-linear filtering due to the limited number of samples. Second, the digital filtering cannot prevent the saturation by the charger noise interference at the RX sensing block. The amplitude of the charger noise can be up to tens-of-volts, and the sensed charge signal is prone to be saturated at the RX sensing block. If the capacitance signal stored in the data buffer is the saturated capacitance signal, the non-linear filtering technique cannot recover the capacitance exactly.

4.3.4 High-Voltage TX Technique

As explored in the previous section, the SNR of the TSC is proportional to the amplitude of the TX driving signal. Therefore, the increase of the TX driving signal amplitude can improve the noise immunity easily. To investigate the relationship between the TX driving voltage and the SNR,

$$V_{CA}(t) \approx \frac{C_M}{C_{FB}} V_{TX}(t) + \frac{C_{C,n}}{C_{FB}} V_{n,ext}(t) \tag{4.3.5}$$

where $C_{C,n}$ is the coupling capacitance between the TSP and the noise source and $V_{n,ext}$ is the noise voltage of the external noise source. According to Eq.(4.3.5), the external noise interference affects the charge amplifier output in proportional to the factor of $\frac{C_{C,n}}{C_{FB}}$. Thus, the increase of capacitance of C_{FB} improves the noise immunity against the external noise interference $V_{n,ext}$. The increase of C_{FB} reduces the sensitivity of touch input, but the increase of V_{TX} compensates the reduced sensitivity. As a result, in the assumption that there is no limitation of increasing capacitance C_{FB}, the increases of V_{TX} can improve the SNR by attenuating the external noise interference without degradation of the sensitivity. For this reason, the amplitude of the TX driving voltage of the TSC is usually set to the maximum voltage of the fabricated CMOS process. In addition, some previous works attempted to increase the TX driving voltage using charge pump [4.22].

However, the high-voltage TX driving technique has some drawbacks. First, the high-voltage driving block requires significantly large power consumption to drive the TSP. Assuming the pulse signal driving structure, the power consumption of the TX driving block can be estimated as following:

$$P_{TX,DRV} \geq \frac{n_{TX}}{2}(C_{TX,par} + n_{RX}C_M)V^2{}_{TX}f_{TX} \tag{4.3.6}$$

where $P_{TX,DRV}$ is the total power consumption of the TX driver, $C_{TX,par}$ is the parasitic capacitance of each TX driving electrode in the TSP, f_{TX} is the frequency of the TX driving signal, and n_{TX} and n_{RX} are the number of TX and RX channels, respectively. The power consumption in Eq.(4.3.6) is proportional to the square of V_{TX}. Thus, the increase of V_{TX} by two times results in increase of the power consumption of four times. Even if the SNR can be improved using the high-voltage TX driving signal, the increase of the power consumption is critical issue. In case of 10-V TX driving signal, the power consumption of the TX driving block is about ten times than that of 3.3-V TX driving signal. Second, the high-voltage TX driving technique requires power converter such as charge pump or boost converter. The power converters require additional external peripherals such as capacitor or inductor in general, which increases the total manufacture cost. Third, the high-voltage TX driving technique needs high-voltage CMOS process, which is more expensive fabrication than normal CMOS process. Hence, the cost of the controller chip also increases inevitably.

4.3.5 Multi-Driving TX Technique

The TX driving architecture in the previous works is usually the single-driving TX structure [4.1][4.2]. The single-driving TX structure applies the driving signal to one driving channel of the TSP at a time. As shown in Fig. 4.9, each driving channel of the TSP is stimulated in sequence, and single frame of capacitance data of the TSP is reconstructed after all driving channels are stimulated. In case of the small-size TSP for smartphones, the single-driving TX structure has advantages of low power consumption and simple implementation [4.1][4.2]. In addition, the single-driving TX structure can support various TSP sizes because it can be easily configured depending on the number of TX channels. To investigate the SNR by the single-driving TX structure, a noise injection model is established as shown in Fig. 4.10. The external noise interference such as the charger noise or display noise is modeled as $\overline{v^2_{n,ext}}$, and the internal noise interference such as thermal noise or flicker noise

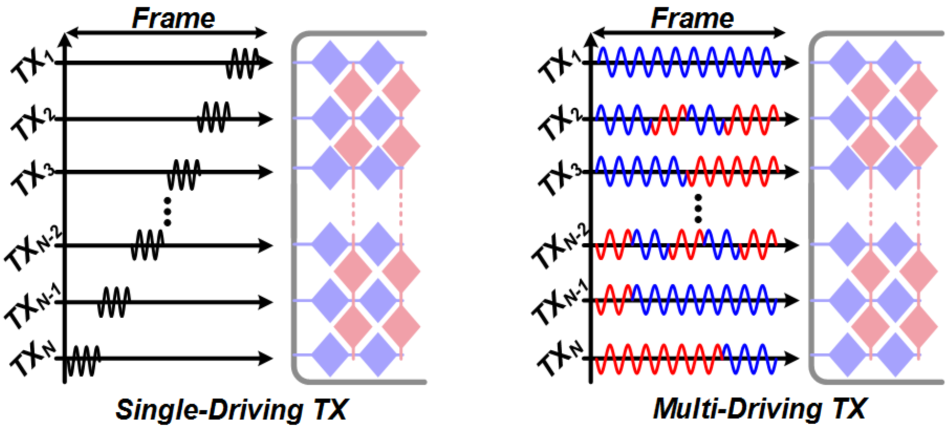

Fig. 4.9 Single-driving TX structure (left) and multi-driving TX structure (right).

of the RX sensing block is modeled as $\overline{v^2_{n,int}}$. For simplicity, both of the noise sources are regarded as additive white Gaussian noise (AWGN) [4.1]. G_{RX} is the gain of the RX sensing block. Assuming the number of TX channels is *n* and the number RX channels is *m*, the variations of the mutual capacitance in the TSP by touch input can be expressed as matrix C as following:

$$C = \begin{bmatrix} \Delta c_{(1,1)} & \cdots & \Delta c_{(1,m)} \\ \vdots & \ddots & \vdots \\ \Delta c_{(n,1)} & \cdots & \Delta c_{(n,m)} \end{bmatrix} \tag{4.3.7}$$

At this time, the single-driving TX structure can be modeled as a matrix H_{SD}.

$$H_{SD} = \begin{bmatrix} h_{(1,1)} & \cdots & h_{(1,n)} \\ \vdots & \ddots & \vdots \\ h_{(n,1)} & \cdots & h_{(n,n)} \end{bmatrix} = \begin{bmatrix} 1 & 0 & \cdots & 0 & 0 \\ 0 & 1 & \cdots & 0 & 0 \\ \vdots & \vdots & \ddots & \vdots & \vdots \\ 0 & 0 & \cdots & 1 & 0 \\ 0 & 0 & \cdots & 0 & 1 \end{bmatrix} = I \tag{4.3.8}$$

Hence, the received signal at the RX sensing block S_{SD} is expressed as following:

$$\begin{aligned} S_{SD} &= G_{RX} H_{SD} C \\ &= G_{RX} \begin{bmatrix} \Delta c_{(1,1)} & \cdots & \Delta c_{(1,m)} \\ \vdots & \ddots & \vdots \\ \Delta c_{(n,1)} & \cdots & \Delta c_{(n,m)} \end{bmatrix} = C_{SD} \end{aligned} \tag{4.3.9}$$

As a result, the variation of the mutual capacitance can be reconstructed using S_{SD}. In theoretically, the sensed capacitance signal of the single-driving TX structure is same with the variation of the mutual capacitance in the TSP. The effect of noise interference by the external noise sources and the internal noise sources in the noise injection model is derived as following:

$$\overline{N^2} = \begin{bmatrix} G^2_{RX}\overline{v^2_{n,ext}} + \overline{v^2_{n,int}} & \cdots & G^2_{RX}\overline{v^2_{n,ext}} + \overline{v^2_{n,int}} \\ \vdots & \ddots & \vdots \\ G^2_{RX}\overline{v^2_{n,ext}} + \overline{v^2_{n,int}} & \cdots & G^2_{RX}\overline{v^2_{n,ext}} + \overline{v^2_{n,int}} \end{bmatrix} \tag{4.3.10}$$

Considering the single-driving TX structure, the sensed noise power can be achieved by multiplying H_{SD} and the noise power in Eq.(4.3.10),

$$\begin{aligned} \overline{N^2_{SD,tot}} &= \left|H_{SD}\right|\overline{N^2} \\ &= \begin{bmatrix} G^2_{RX}\overline{v^2_{n,ext}} + \overline{v^2_{n,int}} & \cdots & G^2_{RX}\overline{v^2_{n,ext}} + \overline{v^2_{n,int}} \\ \vdots & \ddots & \vdots \\ G^2_{RX}\overline{v^2_{n,ext}} + \overline{v^2_{n,int}} & \cdots & G^2_{RX}\overline{v^2_{n,ext}} + \overline{v^2_{n,int}} \end{bmatrix} \end{aligned} \tag{4.3.11}$$

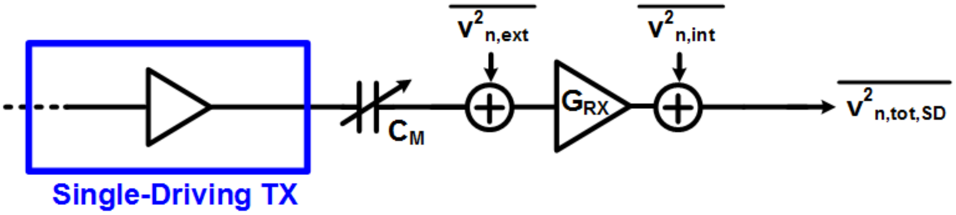

Fig. 4.10 Noise injection model of the single-driving TX structure.

Hence, the SNR can be derived from Eq.(4.3.9) and Eq.(4.3.11) as following:

$$SNR_{SD} = 20\log_{10}\frac{C_{SD}}{\sqrt{\overline{N^2}_{SD,tot}}} = 20\log_{10}\frac{C}{\sqrt{\overline{N^2}_{tot}}}. \tag{4.3.12}$$

In summary, the single-driving TX structure provides simple implementation and scalability of TX driving channels, but noise filtering or signal amplification cannot be achieved through the structure.

Another consideration of the single-driving TX structure is the frame rate. The frame rate *FR* of the AFE using the single-driving TX structure is formulated by

$$FR = k_{RX}\frac{f_{DRV}}{N_{TX}N_{DRV}}, \tag{4.3.13}$$

where f_{DRV} is the frequency of the TX driving signal, N_{DRV} is the number of TX driving signal per unit TX channel, N_{TX} is the number of TX channels in the TSP, and k_{RX} is a constant that represents the RX sensing structure (e.g 2:1 MUX or 3:2 MUX in the RX sensing structure). As investigated in [4.16], the SNR of the AFE is proportional to f_{DRV} and N_{DRV}. Therefore, the frame rate of the AFE is determined by N_{TX} when the AFE uses the single-driving TX structure given SNR specification. In other words, the increase of N_{TX} degrades the SNR of the AFE. In case of the large-size TSP over 10 inches, the SNR degradation is very serious because the number of TX channels is usually more than 30 channels. For this reason, the single-driving TX structure is widely used for the smartphone TSP applications rather than tablet TSP or large-size TSP applications.

Another TX driving structure is the multi-driving TX structure [4.4]-[4.8]. As shown in Fig. 4.9, the multi-driving TX structure applies the TX driving signal to multiple TX channels simultaneously. Compared to the single-driving TX structure, the major difference is the number of driven TX channels at a time. The single-driving TX structure stimulates only one TX channel at a time, but the multi-driving TX structure stimulates a number of TX channels. Hence, a technique that distinguishes the multiple capacitance signals modulated by the simultaneous TX driving signals is required.

As the modulation method, code-division multiplexing (CDM) [4.4]-[4.8][4.10] or orthogonal-frequency-division multiplexing (OFDM) [4.23][4.24] can be applied. Of the two modulation methods, the CDM method is widely used for the large-size TSP because the complexity of the CDM implementation can be much relaxed compared to that of the OFDM. Furthermore, the TX driving frequency range for the large-size TSP is too narrow to support sufficient number of orthogonal frequencies.

The CDM method is based on a modulation matrix that encodes the TX driving signal. Each row or column of the modulation matrix consists of orthogonal sequences, and these sequences are mutually orthogonal. When a modulation matrix H with length of n is given, the cross correlation between each row (or column) H_i is expressed as following:

$$< H_i \bullet H_j >= \begin{Bmatrix} n & i = j \\ 0 & i \neq j \end{Bmatrix} \tag{4.3.14}$$

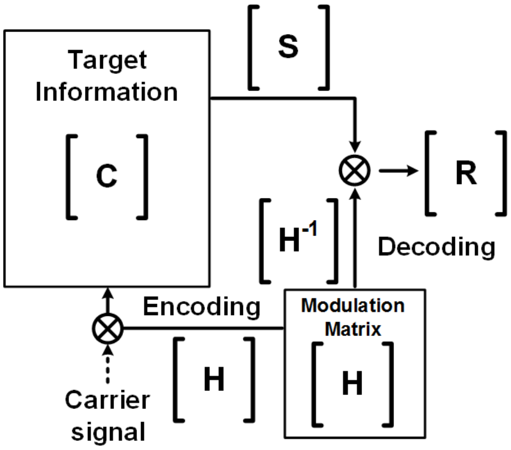

Fig. 4.11 Conceptual diagram of the code-division multiplexing (CDM) method.

Therefore, in theoretical, the encoded information can be perfectly reconstructed after a decoding process. The operational principle of the CDM is shown in Fig. 4.11. The modulation matrix H encodes a carrier signals, and then the encoded carrier signals modulates the target information C. The modulated signal S is finally decoded using the inverse matrix H^{-1}. The decoded matrix R is expressed as following:

$$\begin{aligned} R &= H^{-1}S = H^{-1}(HC) \\ &= nC \end{aligned} \tag{4.3.15}$$

According to Eq.(4.3.15), the decoded signal is n times of the target information. As a result, the CDM method can improve the signal power through the encoding and decoding processes by utilizing the orthogonal matrix. Using the CDM method, the multi-driving TX structure can reconstruct the capacitance data with the multiple TX driving signals.

More detail processes of the multi-driving TX structure are depicted in Fig. 4.12. To distinguish from the modulation and demodulation processes of the mutual capacitance, the terms of encoding and decoding are used for representing the CDM process. The amplitude-modulation (AM) of the mutual capacitance signal of the carrier signal with the CDM encoding is defined as TX modulation process. In the same way, the entire process of reconstruction of the capacitance data is defined as TX demodulation. The encoding is a process of multiplying the TX driving signal, which acts as the carrier signal, with the modulation matrix $H_{TX,RX}$. The encoded driving signal is applied to the TSP, and each capacitance data in the TSP is modulated by the encoded signal. After that, the RX sensing block senses the modulated capacitance signal $S_{TX,RX}$. The capacitance data of the TSP is reconstructed through the decoding process that multiplies $H^{-1}{}_{TX,RX}$ with the sensed signal $S_{TX,RX}$. In summary, the modulation and demodulation process can be expressed as following:

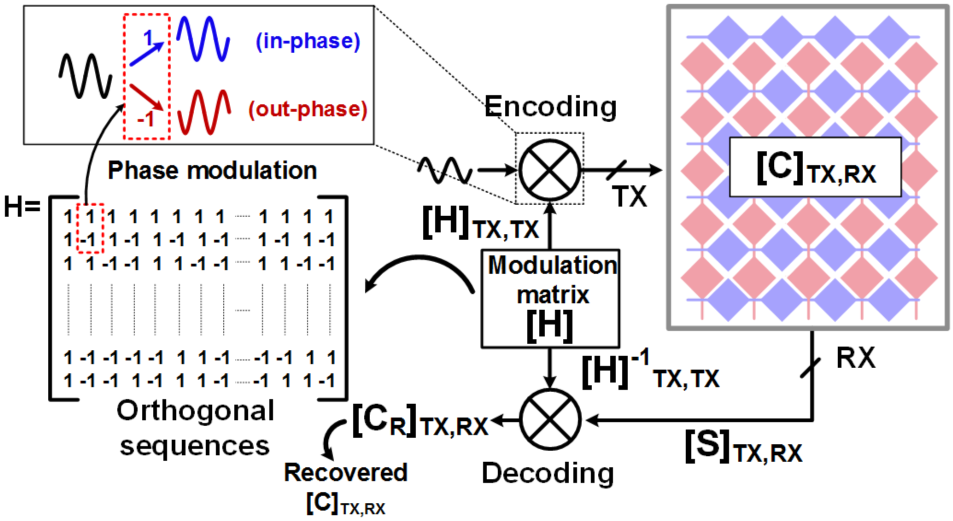

Fig. 4.12 Modulation and demodulation processes of the multi-driving TX structure.

Modulation:

$$S_{TX,RX} = H_{TX,TX} C_{TX,RX} \tag{4.3.16}$$

Demodulation:

$$\begin{aligned} C_{R,TX,RX} &= H^{-1}{}_{TX,TX} S_{TX,RX} \\ &= H^{-1}{}_{TX,TX} H_{TX,TX} C_{TX,RX} \\ &= nC_{TX,RX} \end{aligned} \tag{4.3.17}$$

At the encoding process, the TX driving signals that are going to be applied to each driving channel are converted to in-phase (+1) or out-phase (-1) signals depending on the polarity of the orthogonal sequences of $H_{TX,RX}$. The phase-encoded signals driven to the driving channels are then added at each sensing channel with modulation of the mutual capacitances at each TSP node. Assuming constant frame rate, the SNR improvement by the multi-driving TX structure using the CDM can be derived in the same manner with [4.8][4.25]. First, modulation matrix H_{MD} 's i_{th} column $H_{MD,i}$ can be defined as

$$\begin{aligned} H_{MD} &= [H_{MD,1} \quad H_{MD,2} \quad \cdots \quad H_{MD,n-1} \quad H_{MD,n}] \\ &= \begin{bmatrix} h_{MD(1,1)} & \cdots & h_{MD(1,n)} \\ \vdots & \ddots & \vdots \\ h_{MD(n,1)} & \cdots & h_{MD(n,n)} \end{bmatrix} \end{aligned} \tag{4.3.18}$$

The modulated capacitance signal sensed at the j_{th} RX sensing block according to n_{th} encoding sequence is defined as

$$S_j = \begin{bmatrix} s_{(j,1)} & s_{(j,2)} & \cdots & s_{(j,n-1)} & s_{(j,n)} \end{bmatrix}. \tag{4.3.19}$$

Using the matrix in Eq.(4.3.7), the sensed signal s_{MD} is expressed by

$$s_{MD,(j,k)} = G_{RX}\sum_{i=1}^{n} c_{(i,j)} h_{MD,(i,k)}, \tag{4.3.20}$$

where G_{RX} is the gain of the RX sensing block. In the matrix form, Eq.(4.3.20) can be rewritten as follows:

$$\begin{aligned} S_{MD} &= G_{RX}\begin{bmatrix} \sum_{i=1}^{n} c_{(i,1)} h_{MD,(i,1)} & \cdots & \sum_{i=1}^{n} c_{(i,m)} h_{MD,(i,1)} \\ \vdots & \ddots & \vdots \\ \sum_{i=1}^{n} c_{(i,1)} h_{MD,(i,n)} & \cdots & \sum_{i=1}^{n} c_{(i,m)} h_{MD,(i,n)} \end{bmatrix} \\ &= \begin{bmatrix} S_{MD,1} & \cdots & S_{MD,m} \end{bmatrix} \end{aligned} \tag{4.3.21}$$

In the same manner, the demodulation process in Eq.(4.3.17) can be derived as

$$\begin{aligned} C_{MD} &= G_{RX}\begin{bmatrix} H_{MD.1} \\ H_{MD.2} \\ \vdots \\ H_{MD,n-1} \\ H_{MD,n} \end{bmatrix} [S_{MD,1} \quad S_{MD,2} \quad \cdots \quad S_{MD,n-1} \quad S_{MD,m}] \\ &= G_{RX}\begin{bmatrix} h_{(1,1)} & \cdots & h_{(n,1)} \\ \vdots & \ddots & \vdots \\ h_{(1,n)} & \cdots & h_{(n,n)} \end{bmatrix}\begin{bmatrix} \sum_{i=1}^{n} c_{(i,1)} h_{MD,(i,1)} & \cdots & \sum_{i=1}^{n} c_{(i,m)} h_{MD,(i,1)} \\ \vdots & \ddots & \vdots \\ \sum_{i=1}^{n} c_{(i,1)} h_{MD,(i,n)} & \cdots & \sum_{i=1}^{n} c_{(i,m)} h_{MD,(i,n)} \end{bmatrix} \end{aligned}$$

$$= G_{RX}\begin{bmatrix} nc_{(1,1)} & \cdots & nc_{(n,1)} \\ \vdots & \ddots & \vdots \\ nc_{(1,m)} & \cdots & nc_{(n,m)} \end{bmatrix} = nG_{RX}C \tag{4.3.22}$$

Hence, the reconstructed capacitance signal using the multi-driving TX structure is amplified by *n* times. Compared to Eq.(4.3.9), the multi-driving TX structure can provides *n* times signal power, and this also coincides with Eq.(4.3.17).

To investigate the noise power by the multi-driving TX structure, a noise injection model of the multi-driving TX structure is also established as depicted in Fig. 4.13. The effect of noise interference by the external noise sources and the internal noise sources is same with Eq.(4.3.10). The noise power after the demodulation is derived as

$$\begin{aligned} \overline{N^2{}_{MD,tot}} &= \left|H_{MD}\right|\overline{N^2} \\ &= n\begin{bmatrix} G^2{}_{RX}\overline{v^2{}_{n,ext}} + \overline{v^2{}_{n,int}} & \cdots & G^2{}_{RX}\overline{v^2{}_{n,ext}} + \overline{v^2{}_{n,int}} \\ \vdots & \ddots & \vdots \\ G^2{}_{RX}\overline{v^2{}_{n,ext}} + \overline{v^2{}_{n,int}} & \cdots & G^2{}_{RX}\overline{v^2{}_{n,ext}} + \overline{v^2{}_{n,int}} \end{bmatrix} \end{aligned} \tag{4.3.23}$$

According to Eq.(4.3.23), the demodulated noise power of the multi-driving TX structure is *n* times of the external and internal noise power because the modulation and demodulation processes add the noise interference during a unit frame. From Eq.(4.3.23), the RMS noise of the total noise interference can be derived as

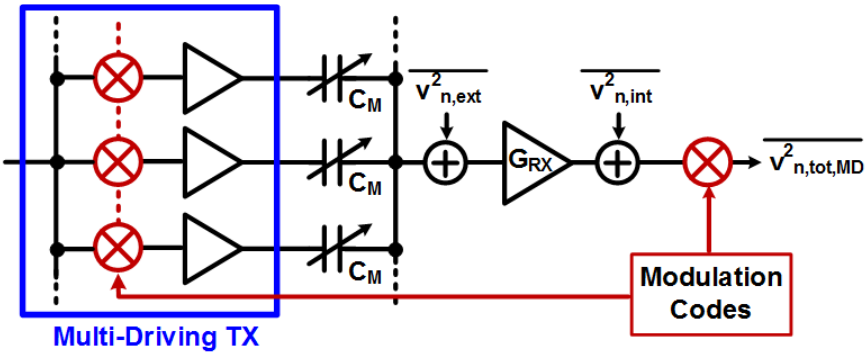

Fig. 4.13 Noise injection model of the multi-driving TX structure.

$$\begin{aligned}
&\sqrt{\overline{N^2_{MD,tot}}} \\
&= \begin{bmatrix} \sqrt{n(G^2_{RX}\overline{v^2_{n,ext}}+\overline{v^2_{n,int}})} & \cdots & \sqrt{n(G^2_{RX}\overline{v^2_{n,ext}}+\overline{v^2_{n,int}})} \\ \vdots & \ddots & \vdots \\ \sqrt{n(G^2_{RX}\overline{v^2_{n,ext}}+\overline{v^2_{n,int}})} & \cdots & \sqrt{n(G^2_{RX}\overline{v^2_{n,ext}}+\overline{v^2_{n,int}})} \end{bmatrix} \\
&= \sqrt{n}\begin{bmatrix} \sqrt{G^2_{RX}\overline{v^2_{n,ext}}+\overline{v^2_{n,int}}} & \cdots & \sqrt{G^2_{RX}\overline{v^2_{n,ext}}+\overline{v^2_{n,int}}} \\ \vdots & \ddots & \vdots \\ \sqrt{G^2_{RX}\overline{v^2_{n,ext}}+\overline{v^2_{n,int}}} & \cdots & \sqrt{G^2_{RX}\overline{v^2_{n,ext}}+\overline{v^2_{n,int}}} \end{bmatrix} \\
&= \sqrt{n}\sqrt{\overline{N^2_{tot}}}
\end{aligned} \tag{4.3.24}$$

Hence, the RMS noise is increased by $\sqrt{n}$ times through the modulation and demodulation processes of the multi-driving TX structure. Considering the increased signal power and noise power, the SNR of the multi-driving TX structure is calculated as following:

$$\begin{aligned} SNR_{MD}[dB] &= 20\log_{10}\frac{C_{MD}}{\sqrt{\overline{N^2}_{MD,tot}}} \\ &= 20\log_{10}\frac{nC}{\sqrt{n}\sqrt{\overline{N^2}_{tot}}} \\ &= 20\log_{10}\frac{C}{\sqrt{\overline{N^2}_{tot}}}\sqrt{n} \\ &= SNR_{SD} + 20\log_{10}\sqrt{n} \end{aligned} \qquad (4.3.25)$$

Compared to the SNR of the single-driving structure in Eq.(4.3.12), the multi-driving TX structure improves the SNR by the amount of $20\log_{10}\sqrt{n}$ in decibel. Eq.(4.3.25) implies that the SNR of the multi-driving TX structure is increased in proportion to the length of the modulation sequence.

In general, the number of the modulation sequence is not larger than the number of the TX channels in the TSP because of the frame-rate degradation. Thus, the SNR improvement by the multi-driving TX structure is usually bounded to the number of TX channels in the TSP. As a result, the multi-driving TX structure can increase the SNR by the amount of up to $\sqrt{n_{TX}}$ times.

In order to investigate the noise reduction by the multi-driving TX structure, a normalized RMS noise is derived with assumption that the SNR is same with that of the single-driving TX structure and the signal power and noise power are divided by n.

$$\begin{aligned}
&\frac{1}{n}\sqrt{\overline{N^2_{MD,tot}}} \\
&= \begin{bmatrix} \sqrt{G^2_{RX}\frac{\overline{v^2_{n,ext}}}{n}+\frac{\overline{v^2_{n,int}}}{n}} & \cdots & \sqrt{G^2_{RX}\frac{\overline{v^2_{n,ext}}}{n}+\frac{\overline{v^2_{n,int}}}{n}} \\ \vdots & \ddots & \vdots \\ \sqrt{G^2_{RX}\frac{\overline{v^2_{n,ext}}}{n}+\frac{\overline{v^2_{n,int}}}{n}} & \cdots & \sqrt{G^2_{RX}\frac{\overline{v^2_{n,ext}}}{n}+\frac{\overline{v^2_{n,int}}}{n}} \end{bmatrix} \\
&= \begin{bmatrix} \sqrt{G^2_{RX}\overline{v^2_{n,ext,MD}}+\overline{v^2_{n,int,MD}}} & \cdots & \sqrt{G^2_{RX}\overline{v^2_{n,ext,MD}}+\overline{v^2_{n,int,MD}}} \\ \vdots & \ddots & \vdots \\ \sqrt{G^2_{RX}\overline{v^2_{n,ext,MD}}+\overline{v^2_{n,int,MD}}} & \cdots & \sqrt{G^2_{RX}\overline{v^2_{n,ext,MD}}+\overline{v^2_{n,int,MD}}} \end{bmatrix}
\end{aligned} \tag{4.3.26}$$

According to Eq.(4.3.26), the normalized external noise power is expressed as following:

$$\overline{v^2_{n,ext,MD}} = \frac{\overline{v^2_{n,ext}}}{n}. \tag{4.3.27}$$

Likewise, the normalized internal noise power is also expressed as following:

$$\overline{v^2_{n,int,MD}} = \frac{\overline{v^2_{n,\mathrm{int}}}}{n} \tag{4.3.28}$$

Eq.(4.3.27) and Eq.(4.3.28) show that the multi-driving TX structure reduces the noise interference of the external noise source and internal noise source effectively. In qualitatively analysis, the noise interference is spread over the entire sensing time of the single frame. In other words, the influence of the noise interference on the touched node disperses over the corresponding sensing channel. The total noise power of the sensing channel is same, but the noise power of the touched node is reduced by the amount of the modulation length n.

In summary, the multi-driving TX structure provides improved SNR. Compared to the single-driving TX structure, the multi-driving TX structure can compensate the SNR degradation by increase of the number of TX channels. Hence, the AFE with the multi-driving TX structure can support the large-size TSP without the SNR degradation. In addition, the noise immunity of the AFE is also improved through using the noise spreading. The influence of the noise interference by the external noise source is spread over the single frame time, and the noise power is reduced effectively.

4.4 Proposed Architecture

The conceptual diagram of the proposed AFE is shown in Fig. 4.14. The proposed AFE is composed of three main blocks: transmitter (TX), receiver (RX), and digital processing blocks. The TX block generates the encoded driving signal that is applied to the driving channels of the TSP. The mutual capacitance of each node in the TSP is then modulated by the driving signal. The RX block of the analog front-end then senses the modulated mutual capacitance signals. After the signal amplifying and noise filtering processes in the RX block, the sensed mutual capacitances of each node are converted to digital data by analog-to-digital converter (ADC). The digital data are then delivered to the subsequent digital back-end block for labeling and touched coordinate calculation.

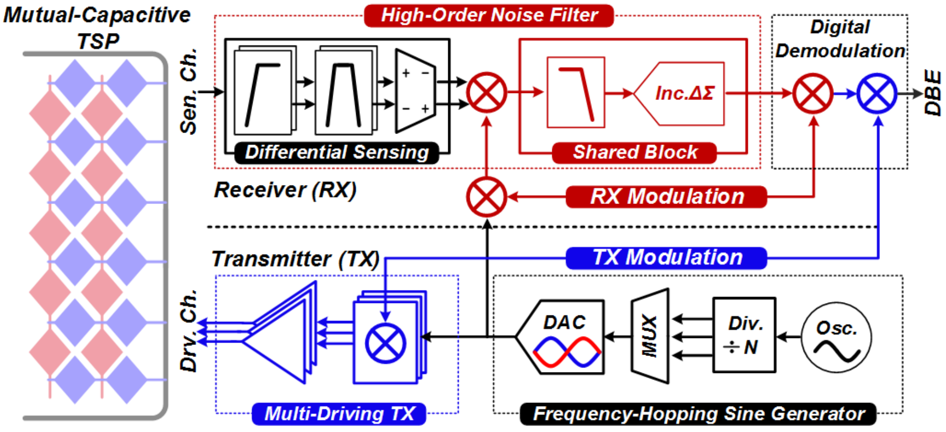

Fig. 4.14 Conceptual diagram of the proposed AFE.

4.4.1 TX Driving Architecture

The conventional TX structure of the AFE is the single-driving TX structure as described in Chapter 4.3.5. The single-driving TX structure provides simple and flexible design of the AFE, but it is vulnerable to the external noise interference. Thus, to improve the SNR and noise immunity, additional techniques that suppress the noise interference are essential. Among the several techniques that enhance the noise immunity, the high-voltage TX driving structure and the multi-driving TX structure can be considered as the TX driving structure. As described in the Chapter 4.3.4, the high-voltage TX driving technique increases the amplitude of the TX driving signal, which is proportional to the SNR of the AFE. At this time, the SNR is proportional to the amplitude of the TX driving signal V_{TX}, and the power consumption is proportional to V^2_{TX}. Therefore, the AFE can improve SNR and noise

Table 4.1 Comparison of multi-driving TX and high-voltage TX structures

	Multi-Driving TX	*High-Voltage TX*
Process	Standard CMOS	HV CMOS
SNR Improvement	$\propto \sqrt{n_{TX}}$	$\propto V_{TX}$
Power Consumption	$\propto n_{TX}$	$\propto V^2_{TX}$
Power / SNR	$\propto \sqrt{n_{TX}}$	$\propto V_{TX}$
DC-DC Converter	-	Require
Digital Demodulation	Require	-

immunity using the high-voltage TX structure. On the contrary, the multi-driving TX structure can be implemented with standard CMOS process. The SNR improvement of the multi-driving TX structure is proportional to square-root of the number of simultaneously driven TX channels. The power consumption is proportional to n_{TX} . The comparison between the multi-driving TX structure and the high-voltage TX structure is shown in Table 4.1.

Assuming that the high-voltage TX driving structure is employs in the AFE, one of the most important things to be considered is the implementation of the TX driving block. Compared to the multi-driving TX structure, the required TX driving voltage to achieve same SNR improvement is $\sqrt{n_{TX}}$ times larger than that of the multi-driving TX structure. Fig. 4.15 shows the required TX voltages depending on

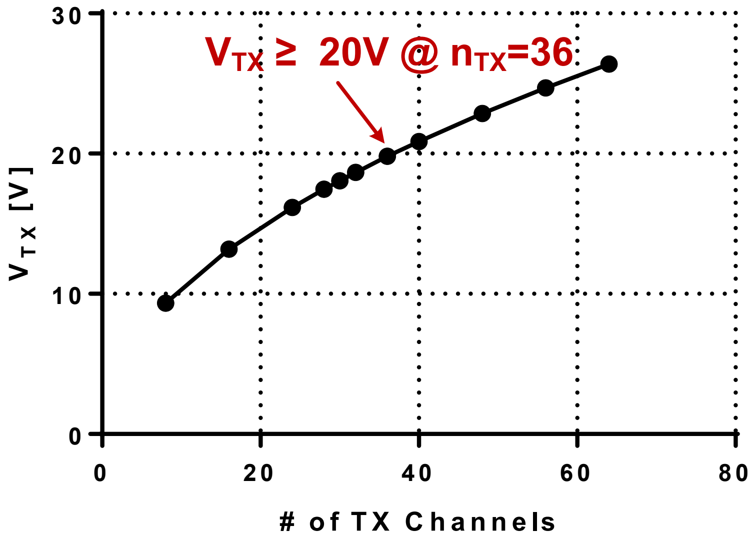

Fig. 4.15 Required TX driving voltage versus the number of TX channels.

the number of TX channel. When the driving voltage of the multi-driving TX structure is 3.3 V, the required TX voltage for the high-voltage TX structure is 20 V. In the recent technology, HV CMOS or BCDMOS processes can support the high voltage of 20 V [4.14], but those technologies are expensive and increase the cost of fabrication. The TSC has to include a non-volatile memory (NVM) such as EEPROM or embedded flash, but the HV CMOS or BCDMOS processes have a limitation of including the NVM. In addition to the technology issues, the high-voltage driver causes significant coupling noise through supply and ground rails, resulting in the degradation of the SNR.

On the contrary, the multi-driving TX structure can be implemented with standard CMOS process. Because the amplitude of the TX driving signal is same with supply voltage, the DC-DC converter or HV MOSFET are not required for the multi-driving TX structure. In addition, the NVM implementation is also possible without limitation. Therefore, the multi-driving TX structure provides more flexibility on the CMOS technology, and it can save the manufacture cost of the TSC. The coupling noise through supply or ground rails is much relaxed compared to the high-voltage TX driving structure. Another advantage of the multi-driving TX structure is the noise reduction of the RX sensing block. As explored in Eq.(4.3.28), the circuit noise of the RX sensing block can be reduced effectively using the multi-driving TX structure. The relaxed noise budget of the RX sensing block results in saving of power consumption or active area. Hence, the proposed AFE employs the multi-driving TX structure in order to enhance the SNR and noise immunity.

In addition to the multi-driving TX structure, the proposed AFE adopts the frequency-hopping sine generator. The injected noise through the TSP has a unique

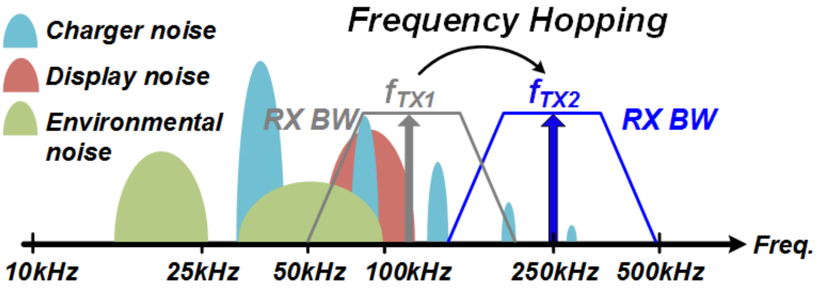

Fig. 4.16 Frequency hopping technique for noisy frequency avoidance.

frequency band. If the frequency of the TX driving signal is overlapped with the frequency band of the injected noise, it is hard to filter out the noise interference at the RX sensing block. Thus, it is desirable to separate the two frequencies as far as possible as shown in Fig. 4.16. The processes of noise frequency detection and avoidance are performed at the DBE of the TSC [4.26], and it is sufficient for the AFE to change frequency of the TX driving signal depending on control signal from the DBE. Therefore, the proposed AFE supports a number of TX driving frequencies to be controlled by the frequency hopping algorithms in the DBE.

4.4.2 RX Sensing Architecture

Although the multi-driving TX structure and the frequency hopping sine generator help reduce the noise interference injected through the TSP, it is not sufficient to be immune against the significant noise sources such as charger or display. Hence, it is essential for the RX sensing block to attenuate the noise interference as much as possible. As shown in Fig. 4.17, the suppression of the out-of-band noise is also important along with the in-band noise because the huge out-of-band noise interference affects the sensed capacitance signal. Even if the noise frequency is far from the TX driving frequency using the frequency hopping technique, the noise interference can disrupt the capacitance signal significantly by being folded into the signal band. Hence, the RX sensing block has to provide not only sensing of the capacitance sig-

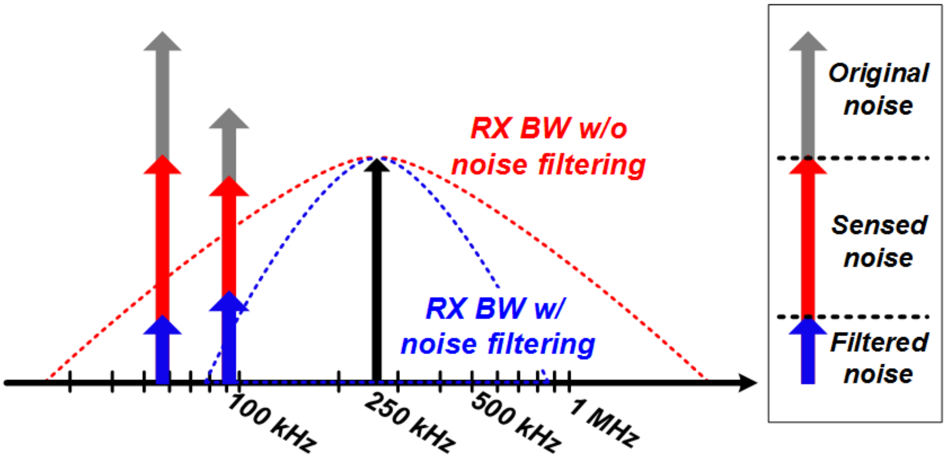

Fig. 4.17 Conceptual diagram on the effect of noise filtering at the RX sensing block.

nal but also high-order noise filtering that suppresses the severe noise interference effectively.

The proposed AFE employs the RX sensing architecture that focuses on the suppression of the noise interference. The RX sensing block adopts a high-order noise filtering structure along with the differential sensing method to improve the immunity against the TSP-injected noise. As shown in Fig. 4.18, the high-order noise filter is composed of the charge amplifier that provides 1st-order high-pass filtering and 2nd-order band-pass filter, and 3rd-order low-pass filter. The differential sensing method for suppression of the common-mode noise and enhancement of touch sensitivity is employed after the high-pass filtering and band-pass filtering processes, preventing saturation by locally injected noise. In addition to the active filters, the RX sensing block uses the incremental ΔΣ ADC with 4th-order Sinc filter. The ADC and decimation filter further improves the noise immunity through the oversampling and averaging processes as explored in the previous chapter. Therefore, the noise interference can be much suppressed through the noise filtering processes, and the RX sensing block provides enhanced noise immunity.

The differential sensing method used in the RX sensing block is pre-filtering differential sensing which performs the differential sensing after the 1st-order high-pass

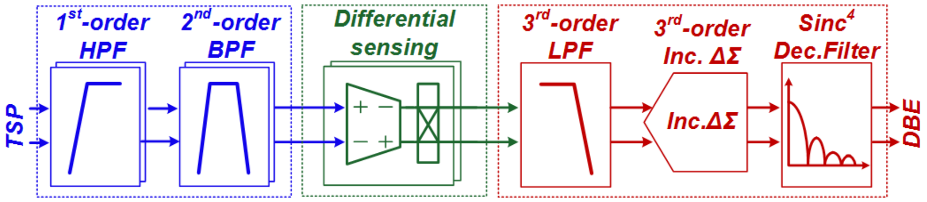

Fig. 4.18 The proposed RX sensing architecture.

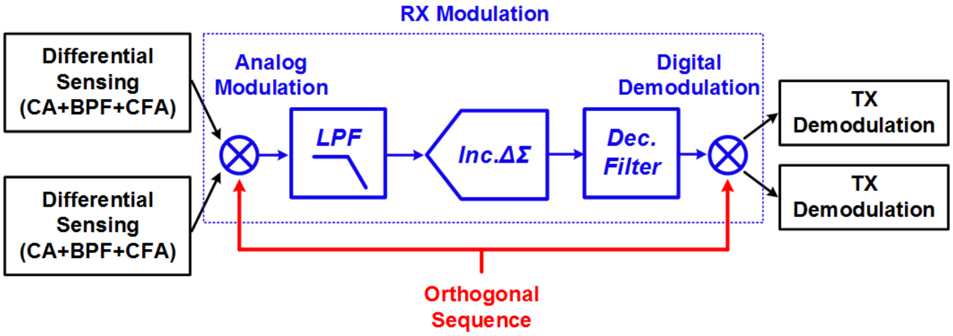

Fig. 4.19 The block diagram of the RX modulation.

filter and 2nd-order band-pass filter. The pre-filtering differential sensing method provides lower CMRR compared to the fully differential sensing methods in [4.8][4.14], but saturation by locally injected noise can be prevented by the pre-filtering process. Therefore, in order to achieve noise immunity against not only common-injection noise but also local-injection noise, the proposed AFE employs the pre-filtering differential sensing method.

As explored in the previous chapter, the column-parallel sensing structure provides high SNR and frame rate. However, the 3rd-order low-pass filter, 3rd-order incremental ΔΣ ADC, and the decimation filter require too much chip area and power consumption to be implemented as the column-parallel sensing structure. The multiplexing scheme used in [4.2][4.4] can reduce the area and power consumption, but a degradations of SNR or frame rate are inevitable. For this reason, the proposed AFE introduces another orthogonal modulation and demodulation processes into the RX sensing block. The RX modulation shares the area consuming blocks, providing reduced chip area and power consumption along with minimizing the SNR degradation compared to the conventional multiplexing scheme. Fig. 4.19 shows the block diagram of the RX modulation. The outputs of the differential sensing block of two sensing channels are modulated by the orthogonal sequence, resulting in single modulated signal. Then, single channel of the low-pass filter, ADC, and decimation filter processes the modulated signal. Therefore, the RX modulation provides 2:1 multiplexing effectively.

In the same manner with Chapter 3, the proposed AFE supports the configurable SNR and frame rate. The number of TX driving cycles per TX modulation sequence can be adjusted by on-chip frame controller. The decimation length of the ADC is also adjusted by the frame controller. As a result, the SNR and frame rate of the AFE can be controlled depending on the required specification. The difference from Chapter 3 is that the frame controller is implemented in the digital block and the configurable range is adjusted to range of practical SNR and frame rate.

The digital demodulator performs the inverse processes of the TX modulation and RX modulation. After the decimation of the ADC output stream, the RX demodulator restores column capacitance data that have been modulated by the RX modulation sequence. Finally, the entire capacitance data of each node in the TSP are recovered by multiplying the inverse matrix of the TX modulation sequences. The recovered capacitance data are then transferred to the DBE to provide labeling and calculation of the touch coordinates.

More details on the RX sensing architecture will be discussed in the following sections.

4.5 Multi-Driving TX Structure

4.5.1 Considerations for TX Modulation Sequence

In case of large-size TSP, the number of the TX channel can be larger than 30. Hence, the encoding sequence length of the TX modulation has to be also larger than 30. In the prior works, Walsh-Hadamard matrix (HM) was usually used as the encoding sequences of which rows or columns are mutually orthogonal [4.7][4.9][4.10]. However, the encoding sequence based on HM has a large code offset in the first column. As shown in Fig. 4.20, the first column of HM consists of only +1 code. Hence, the code offset of the first column is same with the length of the modulation sequence. Because the output swing of the charge amplifier in the RX sensing block is proportional to the code offset, the large code offset results cause the saturation at the charge amplifier output [4.7][4.9][4.10]. Although a large

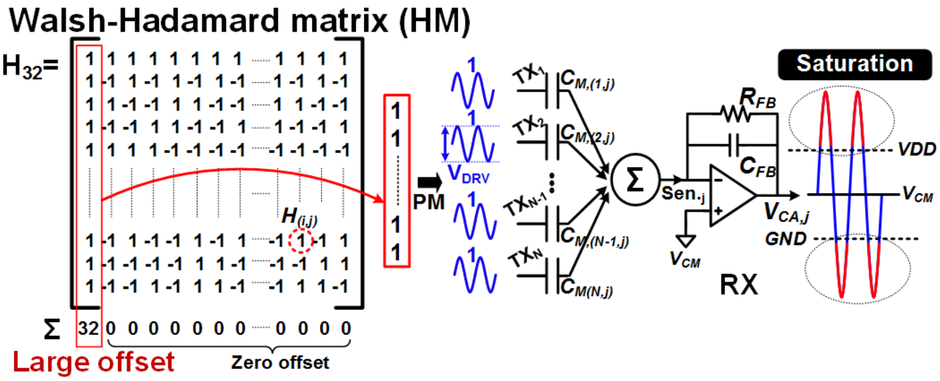

Fig. 4.20 Column offset issue in the modulation codes.

feedback capacitor of the charge amplifier can prevent the saturation by the large code offset, the required capacitance of the feedback capacitance can be up to hundreads-of-pF, which occupies too large chip area and reduces the dynamic range of the touch signal significantly. Therefore, it is important to use low-offset modulation sequence to achieve the SNR improvement through the multi-driving TX structure.

To overcome the problem of the imbalanced code offset, the previous work [4.7] drove only eight channels of the TX at a time and the first column of HM is omitted to reduce the incoming charge by the TX driving signal. This method can provide low-offset modulation and fast touch detection. However, to maximize the noise immunity against the external noise interference, it is essential to increase the number of simultaneously TX channels according to Eq.(4.3.27). In addition, further recovery process of the capacitance data is required to restore the entire capacitance data of the TSP [4.7].

4.5.2 Comparison of Modulation Sequences

In order to exploit the SNR improvement by the multi-driving TX scheme, it is important to maximize the number of TX channels driven simultaneously. As the modulation sequence, a number of orthogonal sequences or matrices can be a candidate. For comparison, the length of the modulation sequence is assumed as 32. The criteria of the comparisons are same with 1) support sequence length up to 36, 2) SNR improvement (orthogonality), and 3) low code offset. In the prior works, HM [4.7], M-sequence [4.8], and Barker sequence [4.6] were used. In addition, a regular

Hadamard matrix was also investigated in [4.10]. Other orthogonal sequences can be applied such as Gold sequence (GS).

Barker code used in [4.6] provides balanced code offset, but the length of known Barker code is limited from 2 to 13. Hence, Barker code is hard to be used in this application. The sequence length of HM is 2^m, and m=6 is required to support the modulation of 36 TX channels. Instead, a modified Hadamard matrix with length of 36 [4.11] can be applied to the TX modulation. Both of Gold sequence and M-sequence have sequence length of 2^m-1. Thus, the lengths of Gold sequence and M-sequence have to be 63 to support the 36 TX channels. As the regular Hadamard matrix, Bush-type Hadamard matrix (BHM) [4.10][4.12], which is special case of the regular Hadamard matrix, supports the sequence length of 36. For the four sequences and the equivalent sequence model of the time-interleaving structure, behavioral modeling of the modulation and demodulation process has been performed as shown in Fig. 4.21. SD-36 indicates the single-driving methods, and the SNR im-

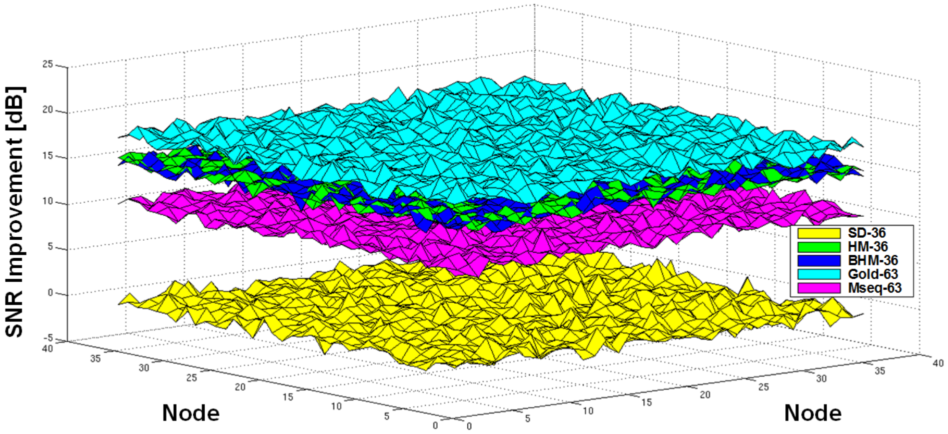

Fig. 4.21 Simulated SNR improvement depending on the modulation sequence.

provements of other sequences are normalized to the SD-36. HM-36 and BHM-36 indicate Hadamard matrix with length of 36 and Bush-type Hadamard matrix with length 36, respectively. Gold-63 and Mseq-63 indicate Gold sequence with length 63 and M-sequence with length of 63, respectively. As shown in Fig. 4.21, the SNR improvements by HM-36 and BHM-36 are about 15 dB, which accords clearly with the analysis in Eq.(4.3.25). In case of Gold-63, the SNR improvement is about 18 dB owing to the long sequence length. However, the SNR improvement of Mseq-63 is only about 11 dB. The low SNR improvement results from the large cross correlation of M-sequence compared to that of Gold sequence.

The maximum code offset of the sequences are compared as shown in Fig. 4.22. The M-sequence provides the smallest code offset of one owing to its balanced +1/-1 formation. On the contrary, HM-36 shows the largest code offset of 36. The BHM-36 provides small offset of six and the offset of Gold-63 is estimated about 14.

Based on the above discussion, it can be claimed that BHM-36 is the most suita-

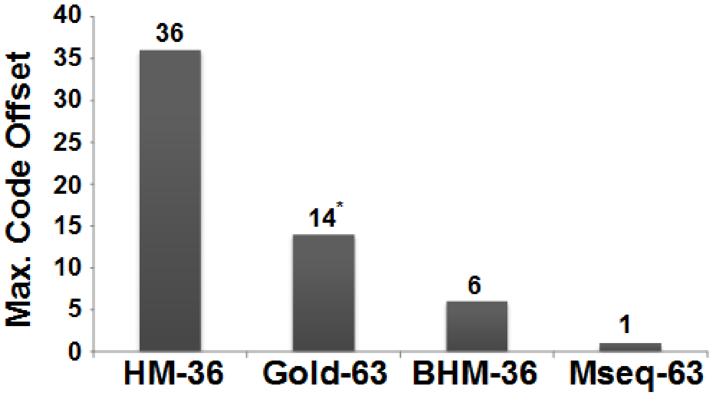

* The lowest max. offset in the number trials among $_{63}C_{36}$ cases. Lower offset can exist.

Fig. 4.22 Maximum code offset of the four sequences.

ble modulation sequence in this application. Gold-63 and Mseq-63 have too long sequence that causes a reduction of frame rate. Compared to HM-36 and BHM-36, the sequence length of Gold-63 and Mseq-63 is about 75 % longer. Hence, a reduction of frame rate is inevitable for the use of the long modulation sequences. On the other hand, BHM-36 shows small code offset of six with sequence length of 36, and the SNR improvement is also good. HM-36 shows same SNR improvement, but it has too large code offset of 36.

4.5.3 Modified Bush-Type Hadamard Matrix

According to the discussion in the previous section, this work employs Bush-type Hadamard matrix (BHM) as the modulation sequence [4.12]. BHM of length 36 (BHM-36) consists of six submatrices of which dimension is six by six as shown in Fig. 4.23(a). The configuration of the submatrices is negative-cyclic formation. Therefore, the code offset of BHM-36 is determined by the combination of each offset of the submatrices. The column offsets of the submatrices are zero except only one submatrix *A*. As shown in Fig. 4.23, the submatrix A exists in all cycles without a sign conversion. Hence, the total code offset of BHM depends on only submatrix *A*. As a result, BHM-36 provides a constant code offset of six. Fig. 4.23(b) shows BHM-36 where the white and black squares indicate +1 and -1, respectively.

The code offset of the modulation sequence can be resolved using BHM-36, but another issue remains due to the phase delay of the TX driving signal at the TSP. The resistance and capacitance of the TSP electrode cause the phase delay of the driving signal. As shown in Fig. 4.24, the submatrix A will be applied to the TX driving channels where are near or far from the RX sensing block. Then, the resistance and capacitance of the TSP signal path becomes different, resulting in different attenuation and phase delay. In case of the smartphone TSPs, the difference between the near and far paths can be negligible. However, the large-size TSPs for the tablet PC can bring about significant variation of phase delay due to the large

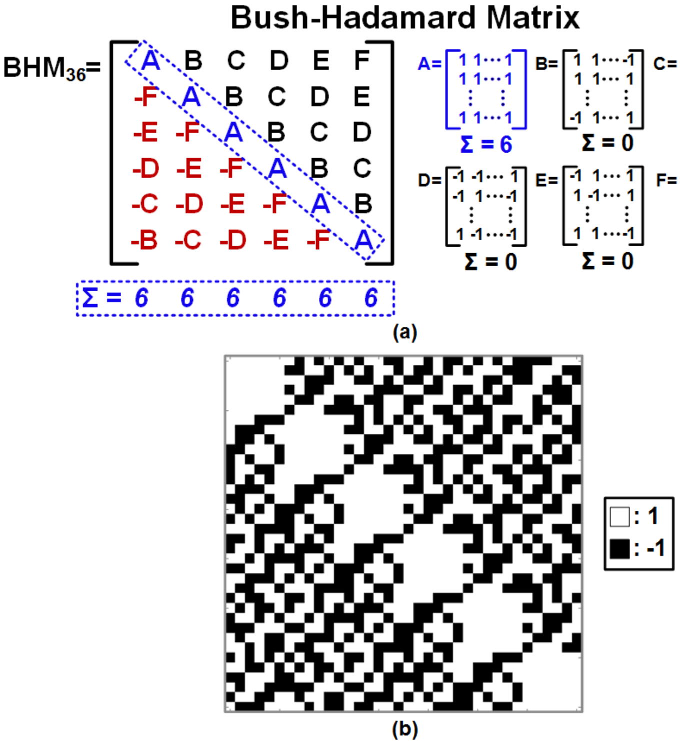

Fig. 4.23 Bush-type Hadamard matrix of length 36.

parasitic capacitance and resistance.

To resolve the phase delay issue, this work proposes a modified BHM-36 (MBHM-36). Each row of the submatrices is separated individually. And then, the rearranged submatrix combines the row from the separated submatrices. For example, the first row of each submatrix is combined to a submatrix. In the same manner, the second row of each submatrix is combined to a single submatrix. In this way, the rearranged MBHM-36 can be achieved as shown in Fig. 4.25. Owing to the balanced distribution of +1/-1, the worst phase delay variation can be much relaxed compared to that of BHM-36.

Fig. 4.26 shows the comparison of code offset between HM-36 and MBHM-36 at each column. The maximum code offset of HM-36 is 36 at the first column as ex-

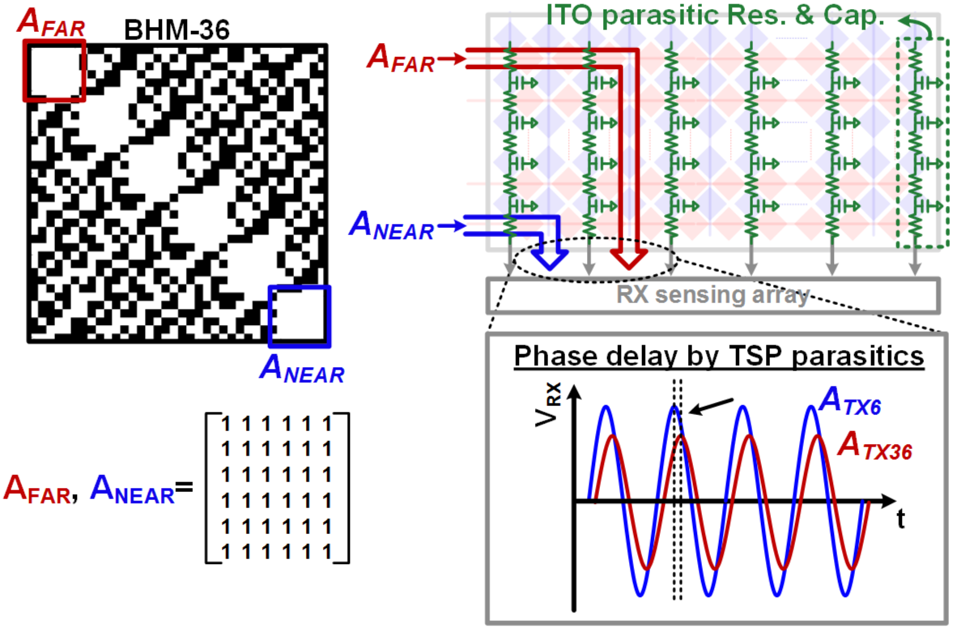

Fig. 4.24 Phase delay issue of BHM-36.

plored in Fig. 4.22. Other columns of HM-36 have offset of zero. On the contrary, MBHM-36 shows constant offset of six at all columns. In case of a partial use of MBHM-36 for driving 32 TX channels, MBHM-36 provides small offset of eight.

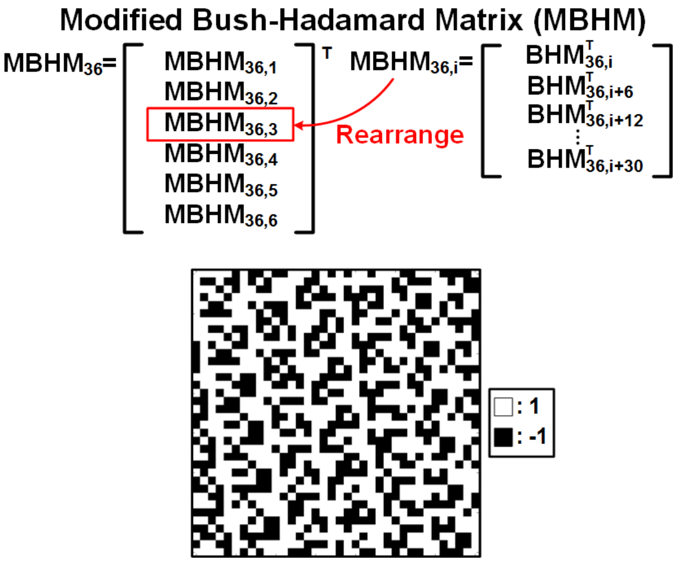

Fig. 4.25 Formation of Modified Bush-type Hadamard matrix of length 36.

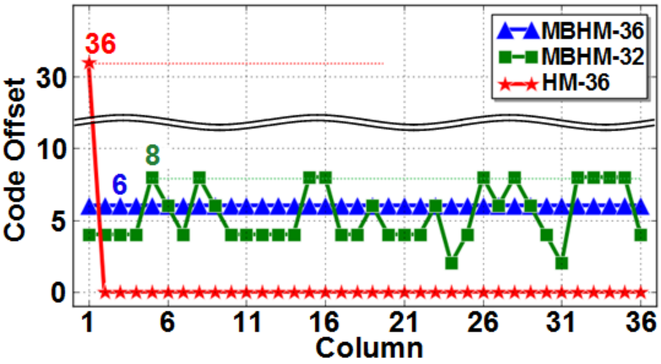

Fig. 4.26 Code offset comparison between HM-36 and MBHM-36 at each column.

4.6 Noise Filtering RX

4.6.1 Pre-Filtering Differential Sensing Method

As described in the previous chapter, there are many noise sources that affect the TSP. The noise sources can be categorized into two groups: common-mode noise source and touch-injection noise source. Fig. 4.27 shows the difference between the common-mode noise and the touch-injection noise. The display noise mainly results from VCOM noise of the display, and the VCOM noise affects all electrodes in the TSP. Thus, the display noise is regarded as the common-mode noise. The charger noise results from the different ground between the touch object and device. Thus, the charger noise only affects the touched electrode. Most of the noise interference

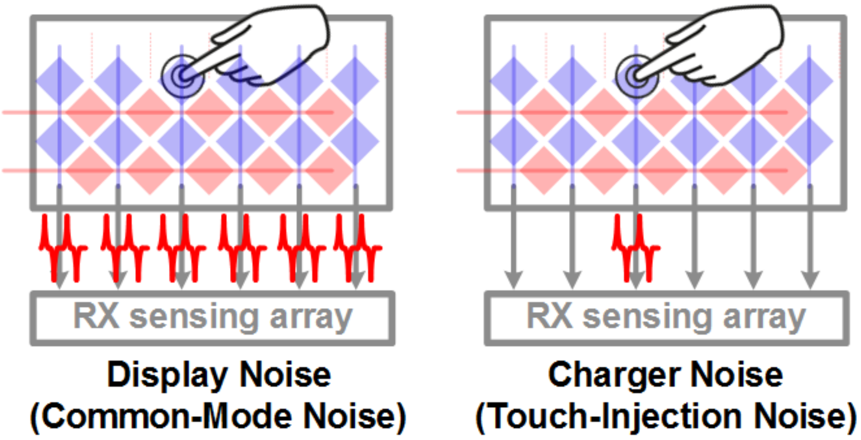

Fig. 4.27 Common-mode noise (left) versus touch-injection noise.

injected through the TSP is the touch-injection noise except the display noise.

As explored in the previous section, the differential sensing method has been widely used to reject the common-mode noise and offset of the capacitance signal. Recently, the fully differential sensing method has been also employed to enhance the rejection of the display noise [4.8][4.14]. Compared to the pseudo differential method in [4.1][4.17][4.18], the fully differential sensing method has high CMRR, providing better display noise rejection. Thus, the fully differential sensing method is superior to the pseudo differential sensing method in terms of the display noise rejection.

However, in case of the touch-injection noise, the fully differential sensing method can cause a fatal saturation at the output due to different noise interferences between two adjacent sensing channels. Fig. 4.28 shows the conceptual diagram of the saturation issue by the touch-injection noise. The high CMRR of the fully differential sensing amplifies the noise interference injected into single sensing channel, and the difference by the noise interference bring about the saturation at the differential

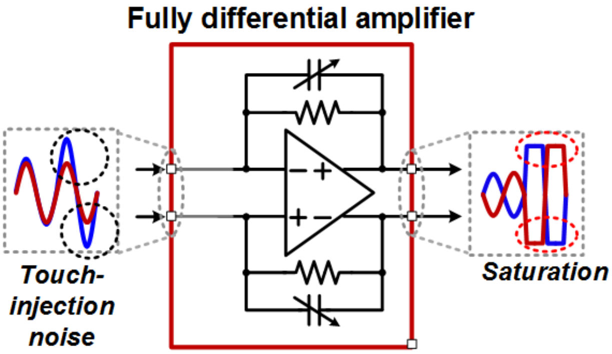

Fig. 4.28 The saturation issue of the fully differential sensing method.

amplifier. Once the capacitance signal is saturated, the following blocks are hard to recover the capacitance data. Thus, the fully differential sensing method distorts the capacitance signal significantly when the touch-injection noise affects the TSP.

In case of the pseudo differential sensing method, the saturation issue by the touch-injection noise can be relaxed slightly owing to the low CMRR and differential gain. But, the 1st-order high-pass filter in the pseudo differential sensing method is not sufficient to suppress the touch-injection noise.

For this reason, this work employs the pre-filtering differential sensing method as depicted in Fig. 4.29. The proposed pre-filtering differential sensing method consists of the charge amplifier, 2nd-order band-pass filter, and fully differential amplifier. The charge amplifier, which converts the charge signal to voltage signal, provides the 1st-order high-pass filtering [4.1][4.2]. In addition, the subsequent band-pass filter further attenuates the TSP-injected noise. Therefore, the charge amplifier and

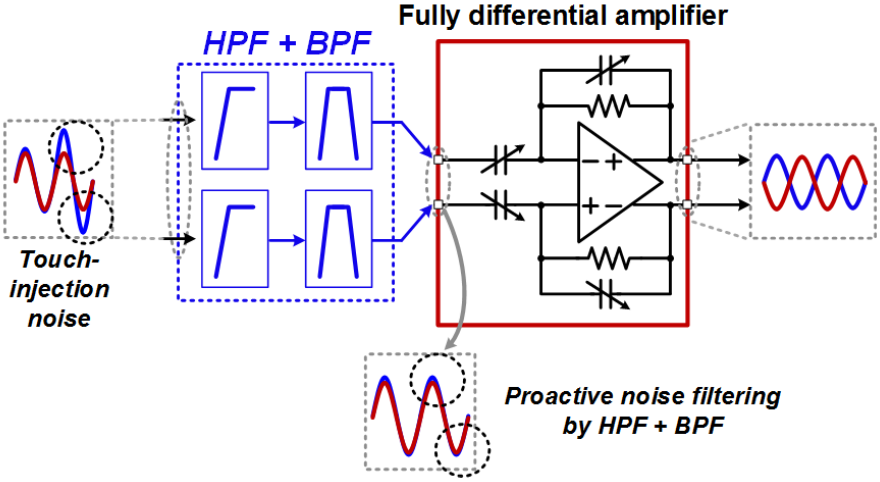

Fig. 4.29 Conceptual diagram of the pre-filtering differential sensing method.

band-pass filter provides proactive noise filtering, preventing saturation by the differential sensing. The noise filtering by the charge amplifier and band-pass filter not only suppress the touch-injection noise but also the common-mode noise. Although the CMRR of the pre-filtering differential sensing is lower than that of the fully differential sensing, the proactive filtering process can supplement the reduced noise rejection. As a result, the pre-filtering differential sensing method provides improved immunity against the common-mode noise and touch-injection noise.

4.6.2 Noise-Immune Sensing Structure

The noise sources that affect the TSP have their own frequency band. As explored in the Chapter 2, the major noise sources that affect the TSP are the display, charger, and environmental noise. It is hard to track the noise frequency in real time, but the noise interference can be filtered out coarsely using the general frequency ranges of the noise sources. For example, the environmental noise such as lamp noise usually appears at the frequency lower than 100 kHz. The display noise also appears at the frequency near 100 kHz. Hence, the sensed signal of frequency lower than 100 kHz can be regarded as the noise interference, and the noise signal is filtered out by the high-pass filter or band-pass filter. In this way, using the rough frequency range of the noise sources, the RX sensing block distinguishes the noise interference from the sensed signal, providing enhanced noise immunity.

Fig. 4.30 shows the conceptual diagram of the noise filtering process in the noise-immune sensing structure. The signal of which frequency is lower than 100 kHz is regarded as the noise interference. Since the frequency of the TX driving signal is always higher than 100 kHz, the signal power of the modulated capacitance signal is distinguished from the low-frequency noise easily. Therefore, the RX sensing block attenuates the low-frequency noise interference using the high-pass filtering and band-pass filtering processes. At this time, high-order high-pass filter may further attenuate the low-frequency noise instead of the band-pass filter. But, there are many EMI sources in the device, and a huge EMI can be coupled into the TSC.

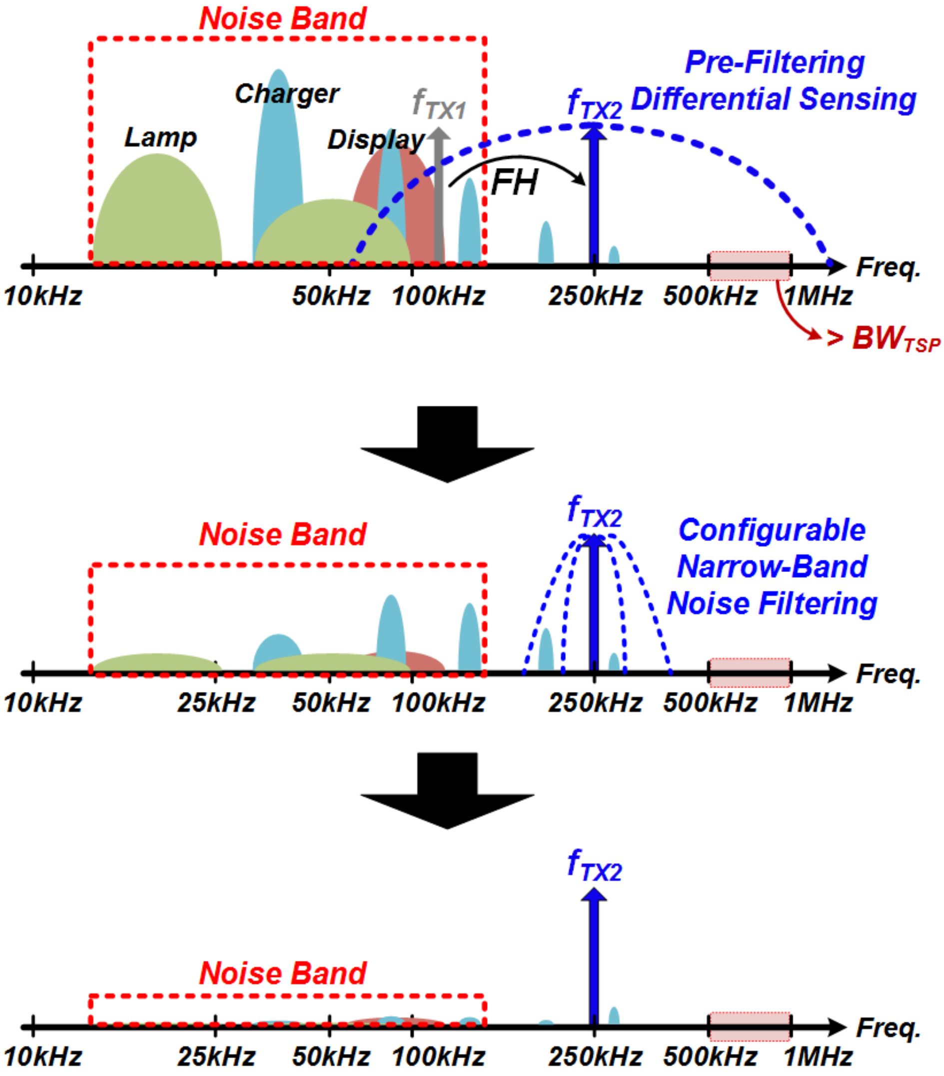

Fig. 4.30 Conceptual diagram of the noise filtering process.

EMI issue can be relaxed through well-designed shield, but unfiltered EMI noise can distort the capacitance signal. Especially, the EMI injected through the FPCB cable and signal lines between the TSP and TSC directly affects the modulated capacitance signal. In addition, the clock frequency of the DBE is usually higher than 10 MHz, and it is coupled into the AFE through the power line or substrate. Therefore, in order to suppress the high-frequency noise interference from the EMI and coupled noise from the DBE, the band-pass filtering along with the high-pass filtering is employed in the first noise suppression step.

In order to determine the order of the band-pass filter, the required noise suppression can be estimated. Of course, higher-order band-pass filter attenuates much more noise interference, but high-order filter is inefficient in terms of the power and area consumption. As shown in Fig. 4.31, assuming the frequencies of the TX driving signal are 250 and 500 kHz, the frequency ratios between the TX driving signal and the two noise-frequency bands are larger than 2.5 and 5, respectively. When up to 20-V_{pp} noise is injected through a finger (8-mm diameter), the estimated charge

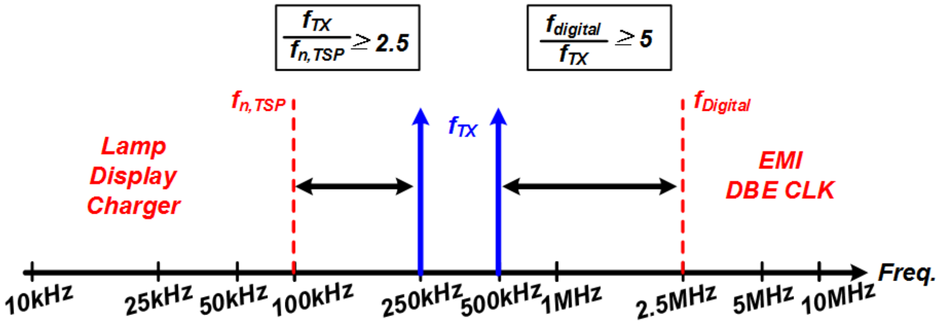

Fig. 4.31 The frequency range of the TX driving signal and noise sources.

noise Q_{noise} can be calculated as following:

$$\begin{aligned} Q_{noise} &= C_C \times V_{noise} \\ &= (2 \times 200\mathrm{fF}) \times 20\mathrm{V_{pp}} \\ &= 8\mathrm{pC} \end{aligned} \tag{4.6.1}$$

where C_C is the coupling capacitance between noise source and signal line (or TSP) and V_{noise} is the amplitude of the noise interference. Since the diameter of the touch object is set to 8 mm, it can be reasonably assumed that two nodes of the TSP are covered by the touch object. Hence, C_C is calculated as two times of the coupling capacitance of single node (~200 fF). When the feedback capacitance of the charge amplifier C_{FB} is set to 20 pF, the noise amplitude at the charge amplifier is same as

$$\begin{aligned} V_{CA,noise} &\approx \frac{Q_{noise}}{C_{FB}} \\ &= \frac{8\mathrm{pC}}{20\mathrm{pF}} = 0.4\mathrm{V_{pp}} \end{aligned} \tag{4.6.2}$$

Considering the differential sensing, the noise signal in Eq.(4.6.2) has not to be saturated at the differential sensing block. Assuming the linear range of the differential sensing output is about 1.5 $\mathrm{V_{pp}}$ and the differential gain is about 20, the acceptable noise amplitude can be estimated as following:

$$V_{Diff,\max} \le \frac{1.5\mathrm{V_{pp}}}{20} = 75\mathrm{mV_{pp}} \tag{4.6.3}$$

Hence, the required high-pass filtering order O_{HPF} by the charge amplifier and band-pass filter can be derived from Eq.(4.6.2) and Eq.(4.6.3).

$$\begin{gathered} O_{HPF} \times 20\log_{10} 2.5 \geq 20\log_{10} \frac{400\mathrm{mV_{pp}}}{75\mathrm{mV_{pp}}} \\ \Leftrightarrow O_{HPF} \geq 1.83. \end{gathered} \tag{4.6.4}$$

Therefore, the required high-pass filtering order is at least 2nd-order filtering (or 12 dB/octave). Since the charge amplifier provides high-pass filtering of 6 dB/octave, the required high-pass filtering by the band-pass filter is also 6 dB/octave. In the same manner with Eq.(4.6.4), the required low-pass filtering order O_{LPF} by the band-pass filter can be calculated. Compared to the TSP-injected noise, the EMI or clock noise coupled through the power or ground rails have much smaller coupling capacitance or peak-to-peak noise amplitude. Thus, 1st-order low-pass filtering is sufficient to suppress the high-frequency noise interference. Thus, $O_{LPF} \geq 1$ is enough condition for the band-pass filter. In summary, the charge amplifier and band-pass filter has to provide at least 12 dB/octave high-pass filtering and 6 dB/octave low-pass filtering. Therefore, it is sufficient to use the 2nd-order band-pass filter for suppression of the noise interference at the first step.

In summary, the charge amplifier and band-pass filter have to provide at least 12 dB/octave high-pass filtering and 6 dB/octave low-pass filtering. Therefore, 2nd-order band-pass filter along with the charge amplifier is employed to suppress the noise interference at the first step. Fig. 4.32 summarizes the noise filtering of the charge amplifier and band-pass filter. At the charge amplifier, the low-frequency

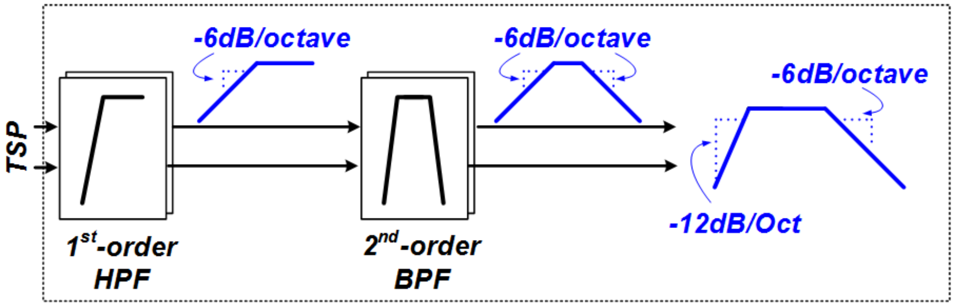

Fig. 4.32 Noise filtering by the charge amplifier and band-pass filter.

noise is suppressed by the amount of -6 dB/octave. After that, the 2nd-order band-pass filter also provides -6 dB/octave high-pass filtering along with -6 dB/octave low-pass filtering. As a result, the low-frequency noise of which frequency is lower than 100 kHz is attenuated by -12 dB/octave. The high-frequency noise by the EMI or DBE is attenuated by -6 dB/octave.

After the noise filtering processes by the charge amplifier and band-pass filter, the differential sensing amplifier rejects the common-mode noise and offset of the modulated capacitance signal. Then, the second step of the noise-immune sensing suppresses the residual noise interference. In case of the charger noise, the frequency range of the noise is too wide to be perfectly rejected at the first filtering step. Even worse, the frequency of the charger noise may be overlapped with the frequency of the TX driving signal. Fortunately, the noise interference near the TX driving frequency can be separated from the capacitance signal because the AFE knows the exact frequency of the TX driving signal. Using a narrow-band noise filter which passes only the capacitance signal, the residual noise interference can be much attenuated.

Fig. 4.33 shows the implementation of the narrow-band noise filter using a high-order band-pass filter and low-pass filter with direct conversion. The high-order band-pass filtering method has advantages of elimination of analog mixer for direct conversion [4.33] and use of digital mixer [4.30][4.31]. However, the implementation of the high-order band-pass filter requires too much area and power consumption. For example, in order to achieve 2nd-order filtering (or 12 dB/octave), 4th-order band-pass filter is required, and it consumes considerable power and area. In case of the AFE for the large-size TSP, the high-order band-pass filtering structure is not suitable due to the significant area and power consumption by multiple sensing channels. In addition, as shown in Fig. 4.34, the ADC and digital mixer has to be operated in the frequency of the TX driving signal, and it also increase the power consumption of the AFE.

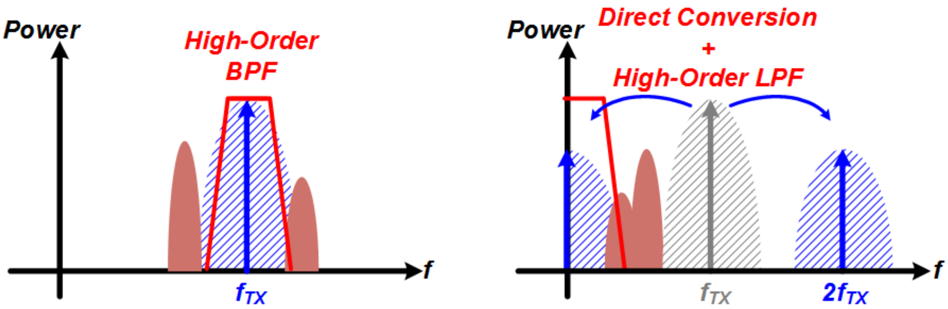

Fig. 4.33 High-order band-pass filtering (left) and low-pass filtering with down-conversion (right).

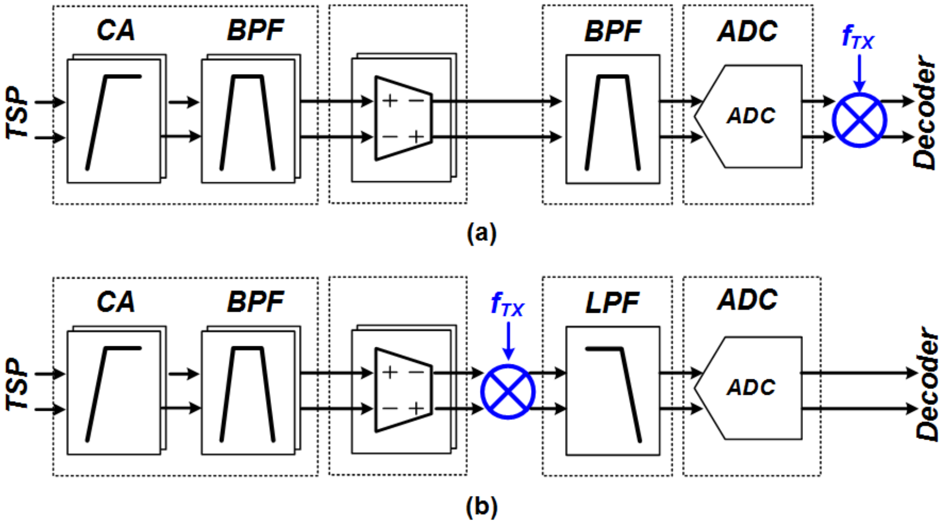

Fig. 4.34 The band-pass filter with digital down-conversion structure (top) and the low-pass filter with analog down-conversion structure (bottom).

On the contrary, the low-pass filter with direct conversion [4.1][4.15]-[4.17] only requires 2nd-order structure to provide the 12 dB/octave noise filtering. Instead of the digital mixer after the ADC, an analog mixer is added, which converts the frequency of the capacitance signal from the frequency of the TX driving signal to DC by multiplying the same frequency square-wave signal as shown in Fig. 4.34. Compared to the implementation of the band-pass filter, the low-pass filter with direct conversion can save both of the power and area consumption. In addition, the ADC and digital filter can be designed as low bandwidth because it is sufficient to process the down-converted signal. In summary, given specification on the power and area consumption, the low-pass filter with down-conversion structure attenuates much more noise interference compared to the band-pass filter structure. Hence, in order to enhance the noise immunity through the narrow-band noise filter, the low-pass filter with down-conversion structure is employed in the RX sensing structure.

To perform the down-conversion of the capacitance signal, a mixer is added ahead of the low-pass filter. There are two implementation ways of the mixer: active mixer and passive mixer. The active mixer [4.23] has advantages of low conversion loss and high sensitivity. But, in the RX sensing block, the differential sensing amplifier provides signal amplification and sufficient driving strength. Thus, it is not required to employ the active mixer such as gilbert cells. For this reason, the passive mixer is employed to provide the down-conversion process. Among a number of topologies of the passive mixer, a CMOS ring mixer is employed owing to its simple structure and capability of phase adjustment.

To investigate the effect of the direction conversion by the mixer, let’s assume that the TX driving signal is sinusoidal waveform with frequency of f_{TX}. Then, the output of the differential sensing along with the noise interference can be expressed as following:

$$\begin{aligned} V_{Diff}(t) &= \frac{\sum_i \Delta C_{M,i}}{C_{FB}} V_{DRV} \cos(2\pi f_{TX} t + \varphi) \\ &+ \frac{\sum_k C_{C,k} V_{N,k} \cos(2\pi k f_{TX} t + \varphi_k)}{C_{FB}}. \end{aligned} \tag{4.6.5}$$

where $\Delta C_{M,i}$ is the difference between adjacent mutual capacitance of i_{th} driving channel and φ is the phase delay due to the parasitic resistance and capacitance of the TSP. To investigate the noise folding effect of the down-conversion process, the noise interference $V_{N,k}$ through $C_{C,k}$ at the frequency of kf_{TX} is included in

Eq.(4.6.5). For simplicity, the frequencies of noise sources are assumed as multiple of f_{TX} and the gain of the differential sensing is set to one. Using Fourier expansion, the square-wave signal with frequency of f_{TX} can be expressed as below [4.34]

$$\begin{aligned} V_{sq}(t) &= \frac{4}{\pi}\sum_{k=1}^{\infty}\frac{\cos(2\pi(2k-1)f_{TX}+\varphi)}{(2k-1)} \\ &= \frac{4}{\pi}\left(\cos(2\pi f_{TX}+\varphi)+\frac{1}{3}\cos(6\pi f_{TX}+\varphi)+\cdots\right). \end{aligned} \tag{4.6.6}$$

At this time, duty cycle of the square-wave signal is supposed to 50 %. Using Eq.(4.6.5) and Eq.(4.6.6), the down-converted signal by the mixer can be derived as below.

$$\begin{aligned} &V_{Mixer,sq}(t) = V_{Diff}(t)\times V_{sq}(t) \\ &= \frac{4}{\pi}V_{DRV}\frac{\sum_i \Delta C_{M,i}}{C_{FB}}\cos(2\pi f_{TX}t+\varphi)\left[\sum_{k=1}^{\infty}\frac{\cos(2\pi(2k-1)f_{TX}t+\varphi_{sq})}{(2k-1)}\right] \\ &+ \frac{4}{\pi}\frac{\sum_k C_{C,k}V_{N,k}\cos(2\pi k f_{TX}t+\varphi_k)}{C_{FB}}\left[\sum_{k=1}^{\infty}\frac{\cos(2\pi(2k-1)f_{TX}t+\varphi_{sq})}{(2k-1)}\right] \\ &= \frac{2}{\pi}V_{DRV}\frac{\sum_i \Delta C_{M,i}}{C_{FB}}\cos(\varphi-\varphi_{sq}) \\ &+ \frac{2}{\pi}\frac{1}{C_{FB}}[C_{C,1}V_{N,1}\cos(\varphi-\varphi_1)+\frac{C_{C,3}V_{N,3}}{3}\cos(\varphi-\varphi_3)+\cdots]. \end{aligned} \tag{4.6.7}$$

Eq.(4.6.7) shows that the frequency of the capacitance signal is converted from f_{TX} to DC. In addition, the noise signal at the odd harmonic frequency of f_{TX} is also

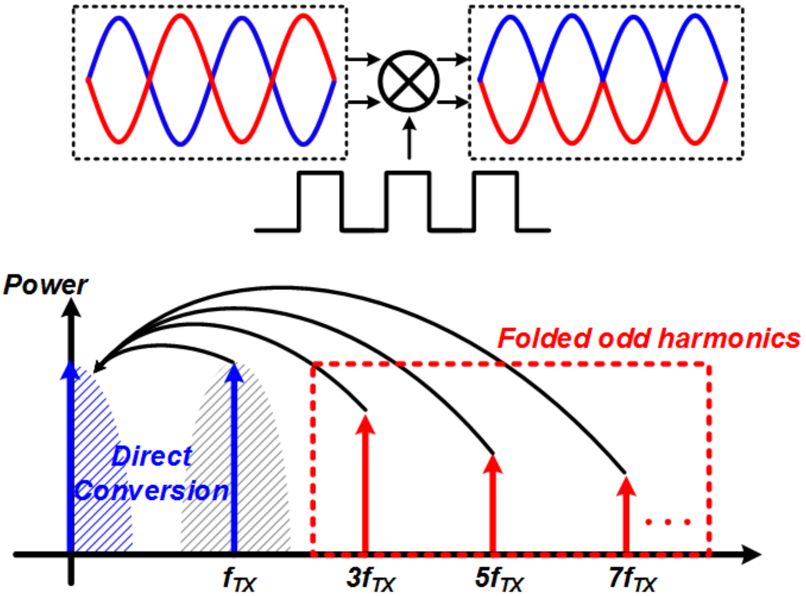

Fig. 4.35 Conceptual diagram of the direct conversion (top) and odd harmonic folding.

folded into DC. Fig. 4.35 shows the direct conversion process by the mixer and folded odd harmonic components. Noteworthy, the noise interference at the odd harmonic frequency of f_{TX} is much smaller than that of the frequency lower than 100 kHz. Furthermore, the band-pass filter ahead of the differential sensing amplifier attenuates the high-frequency noise. Therefore, even if the odd harmonic noise can be folded into the signal band, the distortion on the touch sensing in real applications is negligible.

The narrow-band low-pass filtering after the direct conversion can be implemented with high-order low-pass filter. In the previous work, an anti-aliasing filter was usually employed ahead of the ADC [4.30]. However, to achieve sufficient noise immunity of the AFE, the role of the low-pass filter has to include the suppression of the external noise interference. Although the noise interference can be attenuated by the precedent filtering processes, the noise in the frequency range from 100 kHz to 500 kHz, which is the frequency range of the TX driving signal, is not suppressed sufficiently. For this reason, high-order low-pass filtering that attenuates the residual noise interference. Compared to the precedent noise filtering, the purpose of the high-order low-pass filtering is not only prevention of the saturation but also improvement of the SNR by suppressing the noise interference.

The required order of the low-pass filter can be estimated in the same manner with Eq.(4.6.4). In the normal operation, the minimum cut-off frequency of the low-pass filter can be roughly assumed as 10 kHz because the frame rate of 100 Hz with double sampling techniques requires the signal bandwidth about 8 kHz. In case of the charger noise, the fundamental frequency can be higher than 100 kHz. At this time, the frequency gap f_N between the TX driving signal and the harmonic frequencies of the charger noise can be smaller as 50 kHz as shown in Fig. 4.36. Assuming the worst case harmonic that f_N is 50 kHz is folded into the signal band, the required order of the low-pass filter O_{LPF} can be estimated as below

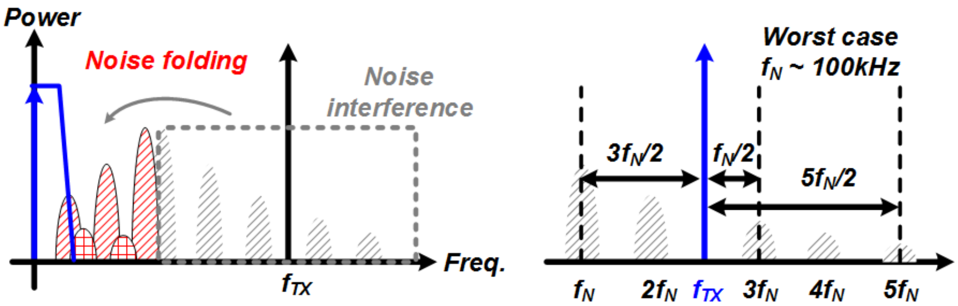

Fig. 4.36 Conceptual diagram of the noise folding issue (left) and frequency gap (right).

$$\begin{aligned} &20\log_{10}(\frac{10\text{kHz}}{50\text{kHz}})^{\text{O}_{\text{LPF}}} \le -60 \\ &\Leftrightarrow \text{O}_{\text{LPF}} \ge 4.3. \end{aligned} \tag{4.6.8}$$

The derived O_{LPF} may be divorced from the measurement results, but it is still worthwhile to know the rough O_{LPF} in order to determine the structure of the high-order low-pass filter.

Fig. 4.37 shows the possible implementations of the high-order low-ass filter. One way to implement the high-order low-pass filter is the cascade of the active low-pass filter. In general, a 2nd-order low-pass filter can be implemented as sallen-key (SK) or multi-feedback (MFB) structures. Based on the 2nd-order low-pass filter, a 3rd-order low-pass filter or 4th-order low-pass filter can be constructer with 1st-order passive filter or another 2nd-order low-pass filter, respectively. In this way, the high-order low-pass filter can be implemented ahead of the ADC as shown in Fig. 4.37(a). Because this structure suppresses the residual noise interference before the

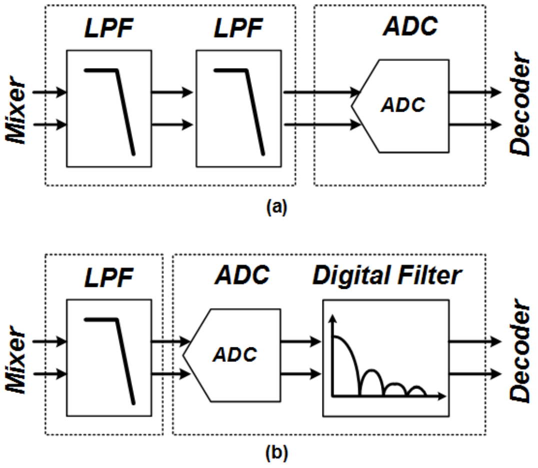

Fig. 4.37 Two possible implementations of the high-order low-pass filter.

analog-to-digital conversion, the noise aliasing issue at the ADC sampling process can be clearly resolved along with the enhancement of the noise immunity.

However, the cascaded structure of the active filter has problems of the area and power consumption. The large number of RX channels imposes a limitation of the layout area. The active filter with cut-off frequency lower than 100 kHz requires large resistors and capacitors. For example, to achieve a cut-off frequency of about 10 kHz, the 2nd-order MFB low-pass filter requires resistors and capacitors of 2 MΩ and 60 pF, respectively (820kΩ, 390kΩ, 820kΩ, 40pF, 20pF, and Q=0.5). Using MIM capacitor of 2 $fF/\mu m^2$, the capacitors used in the filter occupy at least 170×170 μm^2. As a result, it is hard to implement the narrow-band low-pass filter higher than 4th-order structure due to the limited chip area and large number of RX sensing channels.

Instead of the cascaded active filter, single active filter along with the high-order digital filter can be alternative. As shown in Fig. 4.37(b), the high-order low pass filter is composed of the single stage low-pass filter and digital low-pass filter. The analog active filter prevents noise aliasing at the ADC, and the digital filter suppresses the noise interference through its narrow-band and high-order low-pass filtering. Because the narrow-band filtering of the noise interference is mainly conducted by the digital filter, there is no need to use the high-order active filter that consumes large chip area. In addition, in case of the use of oversampling ADC such as incremental ΔΣ, the decimation filter of the ADC can perform not only quantization noise filtering but also the narrow-band noise filtering. Therefore, the adoption of the incremental ΔΣ further improves the area efficiency of the low-pass filter by sharing the decimation filter. But, the active filter for the anti-aliasing process is also required in this structure. The required order of the anti-aliasing filter be derived using the ADC sampling frequency f_{ADC}. Assuming the use of the incremental ΔΣ and f_{ADC} is 2.5 MHz, the aliased noise power should be smaller than the target noise power specification. Thus, the order of the anti-aliasing filter O_{AAF} is derived as below

$$\begin{gathered} 20\log_{10}\left(\frac{100\text{kHz}}{1.25\text{MHz}}\right)^{\mathrm{O_{AAF}}} \le -60 \\ \Leftrightarrow \mathrm{O_{AAF}} \ge 2.74. \end{gathered} \tag{4.6.9}$$

Hence, the 3rd-order low-pass filter with 100-kHz cut-off frequency is sufficient for the anti-aliasing filter. Because the cut-off frequency is about ten times compared to the 10-kHz low-pass filter, the layout area for the resistor and capacitance can be much reduced. In the same manner with above calculation, the required area for resistor and capacitor to implement the anti-aliasing filter is a quarter of the area by the 2nd-order MFB filter with 10-kHz cut-off frequency (330kΩ, 160kΩ, 330kΩ, 10pF, 5pF, and Q=0.5).

To compare the area of the two structures in Fig. 4.37, the capacitance and resistance of the active filter are calculated as shown in Fig. 4.38. The MFB low-pass structure is used to calculate the capacitance and resistance of the active filter. For a pair comparison in the noise by the resistors, the resistances of each structure are set to be equal. In addition, using the real MIM and high-poly resistor characteristics of 0.18-µm CMOS process, the required area for the capacitors and resistors are derived. The passive elements of the 2nd-order MFB filter with cut-off frequency of 10 kHz occupy about 78,600 µm^2. On the contrary, the passive elements of the same structure with cut-off frequency of 100 kHz occupy only 13,600 µm^2.

Using the estimated area of the 2nd-order MFB low-pass filter, the area of the high-order low-ass filter to be used in the RX sensing block can be also calculated. In the same manner with the calculation in Fig. 4.38, only the passive elements in the filter are included in the calculation. In case of the digital Sinc filter, the synthesized area is used for the calculation. From the result of Eq.(4.6.9), the anti-aliasing filter is assumed as 3rd-order MFB low-pass filter composed of the 50-kHz 2nd-order low-pass filter and 100-kHz 1st-order low-pass filter. Fig. 4.39 shows the estimated area of the four low-pass filter structures: 4th-order MFB low-pass filter, 6th-order MFB low-pass filter, 3rd-order AAF with 3rd-order Sinc filter, and 3rd-order AAF with 4th-order Sinc filter. The 4th-order MFB low-pass filer is cascaded structure of the two 2nd-order MFB low-pass filters. Likewise, the 6th-order MFB low-pass filter is composed of the three 2nd-order MFB low-pass filters. The required areas of the 4th-order LPF and 6th-order LPF are 157,000 µm^2 and 236,000 µm^{2,} respectively. Assuming the column pitch of the RX sensing block is 240 µm, the layout length of the filters are estimated as about 650 µm and 980 µm, respectively. The layout sizes of the high-order MFB filters are too large to be implemented in the column-parallel structure. On the other hands, the 3rd-order Sinc filter and 4th-order Sinc filter with AAF occupy only 57,500 µm^2 and 71,800 µm^2, respectively. The layout areas of the Sinc filters with AAF are reduced to more than half compared to the high-order MFB filter structures. The layout lengths of the Sinc filters are 240 µm and 300 µm, respectively. Hence, the structure of the digital Sinc filter with AAF reduces the layout area effectively, which enables the column-parallel structure [4.1][4.17] of the RX sensing block.

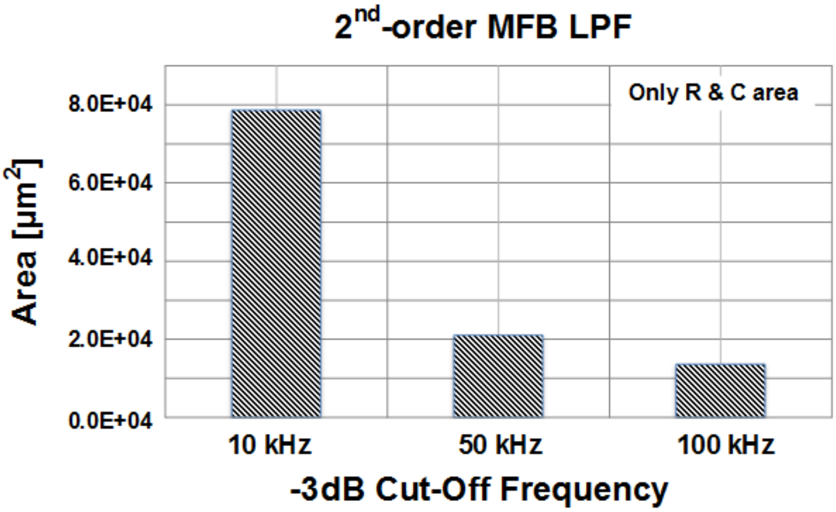

Fig. 4.38 The estimated area of R & C required for 2nd-order MFB implementation.

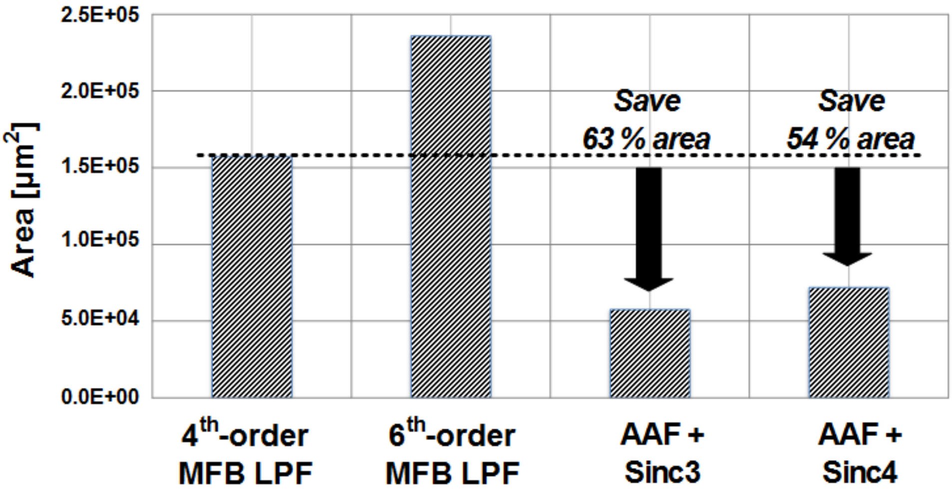

Fig. 4.39 The estimated area for implementation of the four LPF structures.

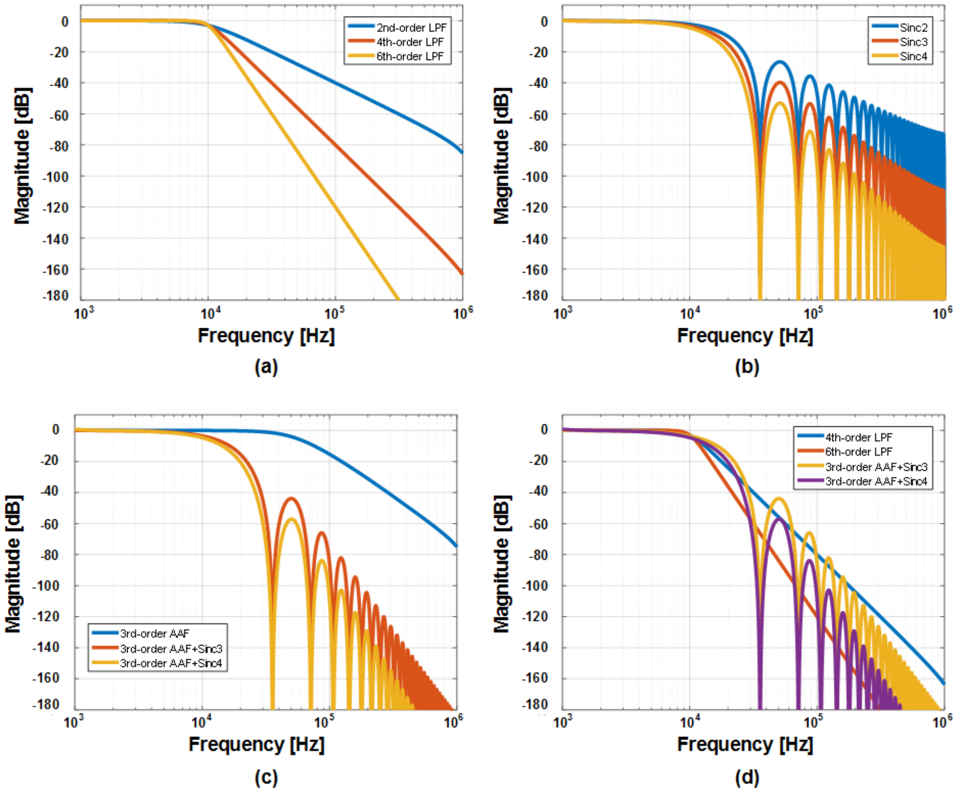

Fig. 4.40 Frequency responses of the high-order low-pass filters.

Fig. 4.40 shows the simulated frequency responses of the low-pass filtering structures. Fig. 4.40(a) shows the frequency response of the high-order MFB low-pass filter. The cut-off frequencies of the filters are set to 10 kHz. Fig. 4.40(b) shows the frequency responses of the Sinc filters. Fig. 4.40(c) shows the frequency response of the combination of the 3rd-order AAF and Sinc filter. The AAF is supposed to cascaded structure of the 2nd-order MFB low-pass filter with 50-kHz cut-off frequency and 1st-order passive RC filter with 100-kHz cut-off frequency. Among the filter structures, the structures that satisfy the specification on the low-pass filter are the active MFB filter higher than 4th-order and the Sinc filter higher than 3rd-order along with the AAF. Fig. 4.40(d) shows the comparison between the 4th-order and 6th-order MFB low-pass filter and the 3rd-order and 4th-order digital Sinc filter with the AAF. The four structures can attenuates the noise interference sufficiently, but the high-order MFB filters are hard to be implemented in the narrow column pitch of the RX sensing block. Therefore, this work employs the digital Sinc filter with AAF structures

4.6.3 Configurable SNR and Frame Rate

As explored in Chapter 3, the configurable SNR and frame rate enable the TSC to cope with various noise environments and applications. The configurable SNR and frame rate is based on the capability of scaling the sensing time. As increasing the sensing time of each capacitance, the SNR can be improved through the over-sampling and averaging effect [4.17][4.35]. Hence, the implementation of the configurable SNR and frame rate uses the scalable sensing time of each modulation sequence. When the length of the TX modulation L_{TX} and RX multiplexing factor L_{RX} are given, the frame rate of the AFE can be expressed as follows:

$$\text{Frame Rate} = \frac{1}{L_{TX} \times L_{RX} \times T_s \times (M_{ADC} + {}^{f_s}\!/_{f_{TX}})} [\text{Hz}]. \tag{4.6.10}$$

where T_s is the sampling period of the ADC and M_{ADC} is the number of sampling cycles by the ADC. The f_s/f_{TX} term is for the reset time. Usually, the frame rate of the TSC in the normal operation mode is set to about 100 Hz. In case of fast touch detection, the frame rate can be increased up to higher than 300 Hz. On the contrary, in case of the some low-end TSC, the frame rate can be reduced below 100 Hz. Thus, given range of the frame rate, the available M_{ADC} can be derived from Eq.(4.6.10). Let's assume that L_{TX} and L_{RX} are 36 and 2, respectively. When the sampling rate of the ADC is set to 2.5 MHz and the TX driving frequency is 250 kHz, the frame rate versus M_{ADC} is obtained as shown in Fig. 4.41. Depending on the number of sampling cycles, the frame rate can be scaled from 50 to 3150 Hz. The previous work in

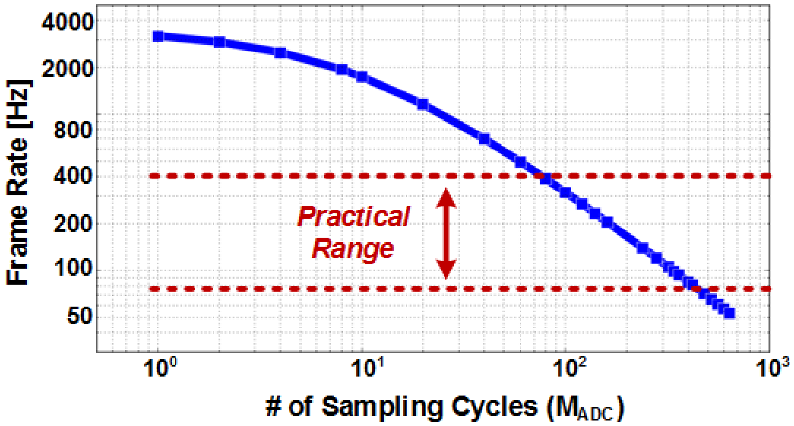

Fig. 4.41 The frame rate versus the number of sampling cycles.

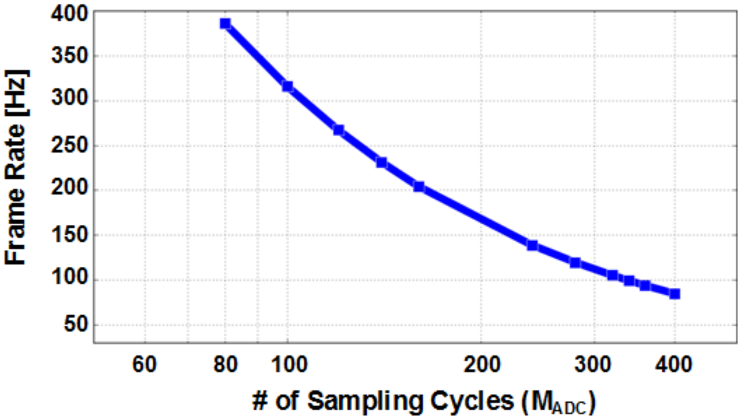

Fig. 4.42 The frame rate versus the number of sampling cycles in the practical range.

Chapter 3 used the full scalable range of M_{ADC}, but the range of the frame rate used in the real application is limited to from 100 to 300 Hz. Thus, this works only uses the practical range of the frame rate from 85 Hz to 385 Hz.

Fig. 4.42 shows the practical range of the frame rate to be used in this work. With the sampling cycles of 80, the AFE can achieve frame rate of 385 Hz. On the contrary, the frame rate can be reduced to 85 Hz by increasing the number of sampling cycles to 400.

Given the range of ADC sampling cycles, the order of the ADC can be determined. Because the incremental ΔΣ ADC operates in transient mode, the resolution by quantization error can be derived. According to [4.37], the resolution of the incremental ΔΣ ADC of single-stage architecture N_{ADC} can be expressed as

$$N_{ADC} \approx \log_2[c_1 c_2 c_3 \frac{(M_{ADC}-2)(M_{ADC}-1)M_{ADC}}{3!}] \text{ [bits]}. \tag{4.6.11}$$

where c_i is the coefficients of the ADC. Assuming that minimum resolution that prevents the distortion of sensing signal by the quantization noise is 10 bits, the required order of the ADC can be derived using Eq.(4.6.11). Fig. 4.43 shows the reso-

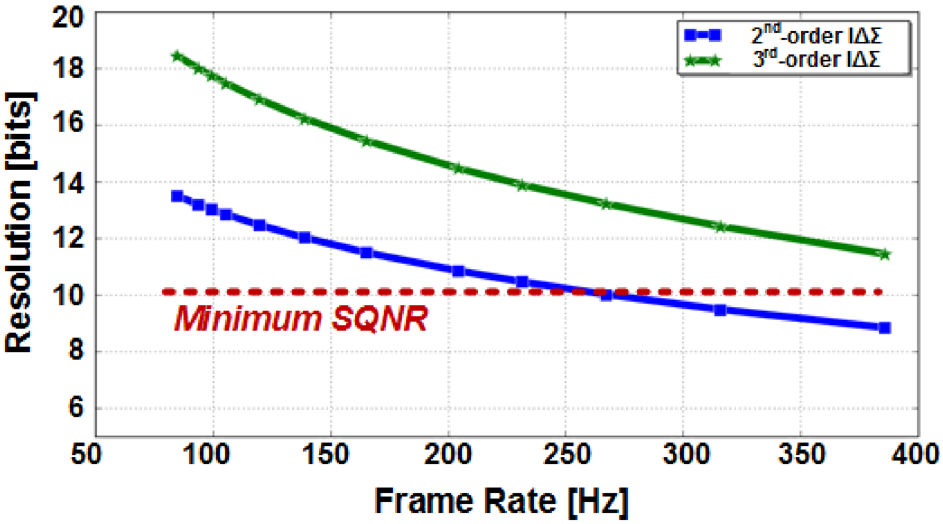

Fig. 4.43 The resolution of the ADC versus the frame rate.

lution of each order incremental ΔΣ ADCs versus the frame rate. Notice that the resolution in Fig. 4.43 considers only quantization noise of the ADC with assumption of ideal integrator. Although the 2nd-order incremental ΔΣ ADC satisfies the resolution requirement in the slow frame rate, the resolution of the ADC is lower than the minimum specification at the frame rate higher than 240 Hz. Therefore, the incremental ΔΣ ADC used in this work is designed as the 3rd-order structure, which provides more than 10 bits at all frame rates. For optimal suppression of the quantization noise, the order of Sinc filter has to be higher than that of the modulator [4.37]. Thus, the Sinc filter for decimation and low-pass filtering of noise interference is designed as 4th-order structure. This also satisfies the requirement on the decimation filter which explored in the previous section. In summary, the architectures of the ADC and its decimation filter are 3rd-order incremental ΔΣ ADC and 4th-order Sinc decimation filer.

According to Eq.(4.6.10), the scalable factor for configuration of the frame rate and SNR is M_{ADC}, which is determined by the number of TX driving cycles M_{TX} and the ratio between f_s and f_{TX}. Since f_s and f_{TX} are hard to be changed for the configuration of the frame rate and SNR, the only configuration term is M_{TX}. To investigate the capability of M_{TX} configuration, the timing diagram of the AFE is depicted in Fig. 4.44. *MBHM-36* is the TX modulation sequence and *RX mod.* is the multiplexing scheme to be discussed in the next section. The reset signal *RST* is activated at every edge of *RX mod.* signal during a unit TX driving period. Then, *RST* goes down, and the TX driving signal is applied to the TSP. At this time, the number cycles of TX driving signal applied to the TSP during low RST is M_{TX}. Therefore, M_{TX} is determined by the period of *RST* and f_{TX}. Using this relationship, M_{TX} can be defined as

$M_{TX} = f_{TX} / f_{RST} - 1$. Therefore, by scaling the period of *RST*, the configuration of the frame rate and SNR can be implemented simply.

Fig. 4.45 shows the configuration of T_{RST} and M_{TX}. In order to double M_{TX} as four, T_{RST} is multiplied by the amount of 5/3. Compared to the timing diagram in Fig. 4.44, both of M_{TX} and M_{ADC} are doubled. In this way, the AFE can adjust the frame rate from 85 Hz to 385 Hz.

The block that controls T_{RST} is be implemented with digital frame controller. At this time, the clock phases of *MBHM-36*, *RX Mod.* and *ADC* clock have to be

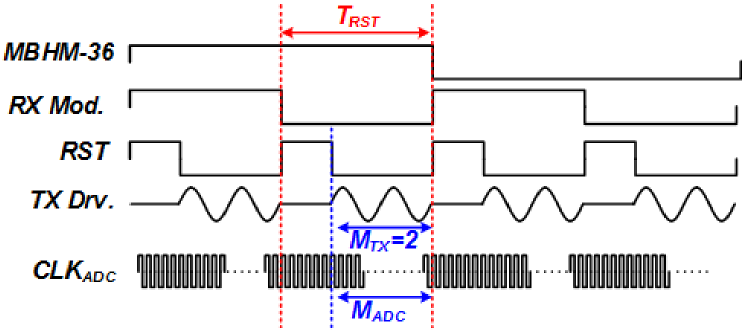

Fig. 4.44 Timing diagram of the AFE.

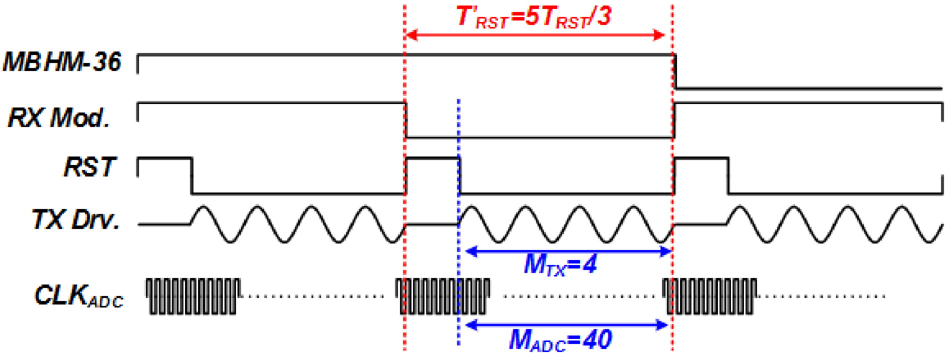

Fig. 4.45 Configuration of T_{RST} and M_{TX} for higher SNR.

aligned with *RST*. Therefore, the rising edge of *RST* plays role of trigger for other clocks such as *MBHM-36* or *RX Mod.*. As shown in Fig. 4.46(a), the phases of *RX Mod.*, TX driving signal, RST_{ADC}, and ADC outputs are aligned to the rising edges of *RST*. The frame rate controller is implemented with counter and edge generation logic as shown in Fig. 4.46(b). Depending on the programmed M_{TX}, the frame rate controller generates the reset signal *RST*.

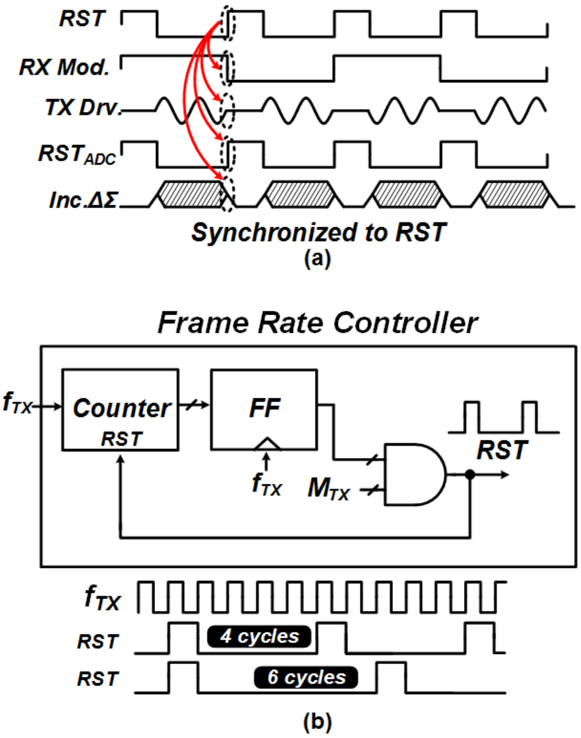

Fig. 4.46 (a) Timing relationship between RST and other clocks and (b) the implementation of the frame rate controller.

4.6.4 RX Modulation

The column-parallel RX architecture [4.1] improves the SNR of the AFE by increasing sensing time of each capacitance node [4.16]. However, in case of large-size TSP with a number TX and RX channels, the column-parallel structure requires significantly large area and power consumption. Especially, the 3rd-order low-pass filter, ADC, and its decimation filter occupy considerable area, and they are hard to be implemented with the column-parallel architecture. Fig. 4.47 shows the estimated area of each block to be implemented in the RX sensing block with assumption of the column-parallel architecture. The low-pass filter, ADC, and decimation filter occupy 75% of the entire RX area, which is much larger than that of other blocks. Therefore, it is required to share the area-consuming block along with a minimization of performance degradation by the sharing scheme.

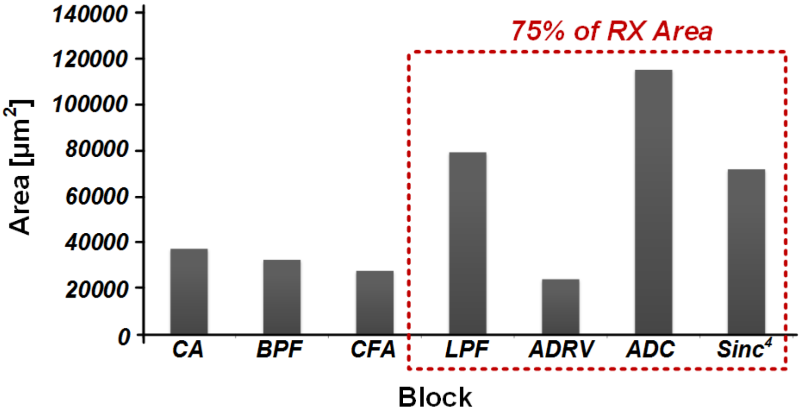

Fig. 4.47 Estimated area of each block with the column-parallel architecture.

There are two ways to share the area-consuming block: multiplexing method and modulation method. The multiplexing method has been widely used in the large-size TSP controller [4.4][4.8][4.18][4.38]. Fig. 4.48(a) shows the block diagram of the multiplexing method. A number of RX sensing channels share the low-pass filter, ADC and decimation filter with time-interleaving structure. Hence, the RX sensing time of each node is divided by the multiplexing factor *N*. Although a sample-and-hold block can store capacitance signal [4.2], the wide-band noise interference is

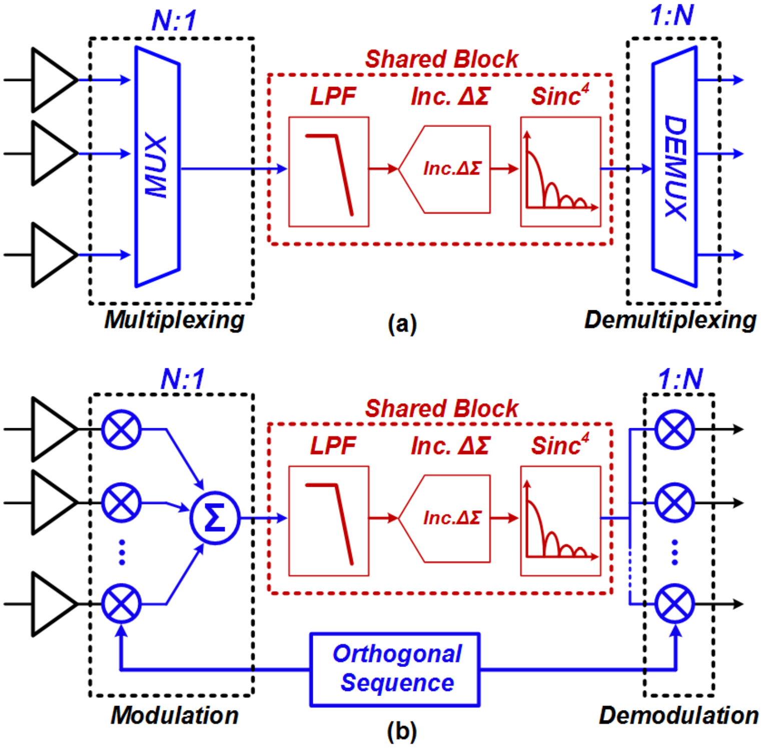

Fig. 4.48 Two implementation ways to share the large-area block: (a) multiplexing method and (b) modulation method.

aliased without attenuation by the low-pass filter. For this reason, the adoption of the sample-and-hold block is excluded in this work.

Another way to share the blocks is the modulation method. In the same manner with the TX modulation as explored in the previous section, the modulation method encodes the multiple input signals into single signal. Then, the encoded signal is processed with only single channel of the low-pass filter, ADC, and decimation filter. As the modulation code, the orthogonal sequence such as Walsh-Hadamard sequence [4.39] is used simply.

To compare the two block-sharing methods, the equivalent noise models of each method are established as shown in Fig. 4.49. The noise model of the multiplexing method in Fig. 4.49(a) consists of the direct-converted noise of the differential sensing output $\overline{v^2_{n,Diff}(f)}$, low-pass filter noise $\overline{v^2_{n,LPF}(f)}$, and the ADC noise $\overline{v^2_{n,ADC}(f)}$. The total output noise of the N_{RX} multiplexing method $\overline{v^2_{n,RX,MUX}(f)}$

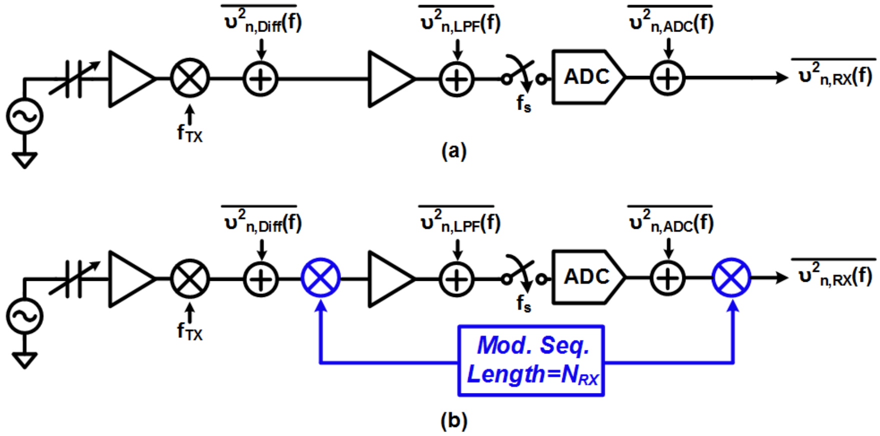

Fig. 4.49 Equivalent noise models of (a) the multiplexing method and (b) the modulation method.

can be expressed as follows:

$$\overline{v^2{}_{n,RX,MUX}(f)} = \overline{v^2{}_{n,Diff}(f)} + \overline{v^2{}_{n,LPF}(f)} + \overline{v^2{}_{n,ADC}(f)}. \tag{4.6.12}$$

When the signal power of the N_{RX} multiplexing sensing method is P_{Sig}, the SNR can be established given noise bandwidth from BW_{N1} to BW_{N2} as following

$$\begin{aligned} SNR_{MUX} &= \frac{P_{Sig}}{P_n} = \frac{P_{Sig}}{\int_{BW_{N1}}^{BW_{N2}} \overline{v^2{}_{n,RX,MUX}(f)}df} \\ &= \frac{P_{Sig}}{\int_{BW_{N1}}^{BW_{N2}} [\overline{v^2{}_{n,Diff}(f)} + \overline{v^2{}_{n,LPF}(f)} + \overline{v^2{}_{n,ADC}(f)}]df}. \end{aligned} \tag{4.6.13}$$

On the contrary, the total output noise of the modulation method with length of N_{RX} $\overline{v^2{}_{n,RX,MOD}(f)}$ is expressed as below

$$\begin{aligned} \overline{v^2{}_{n,RX,MOD}(f)} &= N_{RX} \sum_{i}^{N_{RX}} \overline{v^2{}_{n,Diff}(f)} \\ &+ N_{RX} \left[\overline{v^2{}_{n,LPF}(f)} + \overline{v^2{}_{n,ADC}(f)} \right]. \end{aligned} \tag{4.6.14}$$

Compared to the multiplexing method, the modulation method has signal power which is N_{RX} times larger than that of the multiplexing method in the same manner with the TX modulation. At this time, it is assumed that the modulation process does not saturate the output. On the contrary, the noise contributions of the low-pass filter and ADC are same with those of the multiplexing method except the direct-converted noise $\overline{v^2{}_{n,Diff}(f)}$. Hence, the SNR of the modulation method is established as

$$\begin{aligned}
SNR_{MOD} &= \frac{N^2{}_{RX} P_{Sig}}{P_n} = \frac{N^2{}_{RX} P_{Sig}}{\int_{BW_{N1}}^{BW_{N2}} \overline{v^2{}_{n,RX,MOD}(f)} df} \\
&= \frac{N^2{}_{RX} P_{Sig}}{\int_{BW_{N1}}^{BW_{N2}} [N_{RX} \sum_i^{N_{RX}} \overline{v^2{}_{n,Diff}(f)} + N_{RX} \overline{v^2{}_{n,LPF}(f)} + N_{RX} \overline{v^2{}_{n,ADC}(f)}] df} \\
&= \frac{P_{Sig}}{\int_{BW_{N1}}^{BW_{N2}} [\frac{N_{RX} \sum_i^{N_{RX}} \overline{v^2{}_{n,Diff}(f)}}{N_{RX}} + \frac{\overline{v^2{}_{n,LPF}(f)}}{N_{RX}} + \frac{\overline{v^2{}_{n,ADC}(f)}}{N_{RX}}] df}.
\end{aligned} \tag{4.6.15}$$

Eq.(4.6.15) implies that the modulation method reduces the noise contribution of the low-pass filter and ADC by the amount of N_{RX} compared to the multiplexing method in Eq.(4.6.13). Therefore, the modulation method can improve the SNR of the AFE by reducing the noise power of the low-pass filter and ADC, which minimizes the SNR degradation due to sharing the area consuming blocks. Notice that $\overline{v^2{}_{n,LPF}(f)}$ and $\overline{v^2{}_{n,ADC}(f)}$ include the effect of flicker noise and offset. Thus, the modulation method can also mitigate the low-frequency noise interference by the factor of N_{RX}.

To distinguish from the TX modulation, the modulation method applied to the RX sensing block is called as RX modulation. Using the RX modulation method, the area consumption by the shared block will be reduced. However, the reduced area will be limited because the area of sensing blocks ahead of the low-pass filter is not reduced through the modulation. In addition, the RX modulation method limits the input range of the capacitance signal due to the modulation process. Therefore, it is important to determine an optimal N_{RX}.

Fig. 4.50 shows the estimated single-channel RX area versus N_{RX}. The single-channel RX include the charge amplifier, band-pass filter, differential sensing amplifier, RX modulation unit, low-pass filter, ADC, and decimation filter. When the upper bound of the total RX area is set to 20 mm^2, the required N_{RX} is larger than one. Therefore, the RX modulation of length two is sufficient condition to satisfy the RX area constraint. Notice that the area reduction by the RX modulation decrease significantly when $\mathrm{N_{RX}}$ is larger than four. This results from the area of the charge amplifier, band-pass filter, and the differential sensing amplifier, which are not scaled by $\mathrm{N_{RX}}$. For this reason, it is efficient to choose N_{RX} between two and four.

Considering the output range of the differential sensing amplifier in normal mode, the reduction of differential gain is inevitable due to the summation at the modulation process. Then, the normalized signal power will be reduced, resulting in degradation of the SNR.

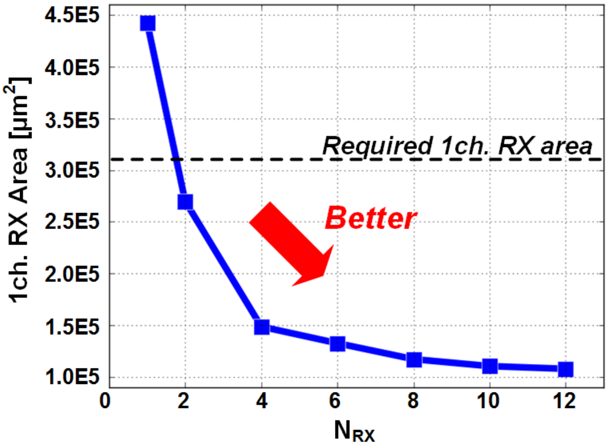

Fig. 4.50 Estimated single-channel RX area versus $\mathrm{N_{RX}}$.

To quantify the effect of RX modulation on the SNR, the normalized SNR versus N_{RX} is explored theoretically. Assuming that the noise power of $\overline{v^2_{n,LPF}(f)} + \overline{v^2_{n,ADC}(f)}$ is about half of $\overline{v^2_{n,Diff}(f)}$, then the normalized SNR can be plotted as same with Fig. 4.51. With assumption that the intrinsic noise of the RX sensing block is dominant, the highest normalized SNR can be achieved with N_{RX} between two and three. In addition, the tolerable peak-to-peak noise at the RX modulation block is reduced as increasing N_{RX}. Thus, in terms of the noise immunity, it is better to set N_{RX} as small as possible. As a result, the optimal N_{RX} in this work is set as two considering the required area reduction and noise performance.

Fig. 4.52 shows the block diagram of the RX modulation. Using the derived N_{RX} of two, the modulation sequence uses Walsh-Hadamard sequence of length two

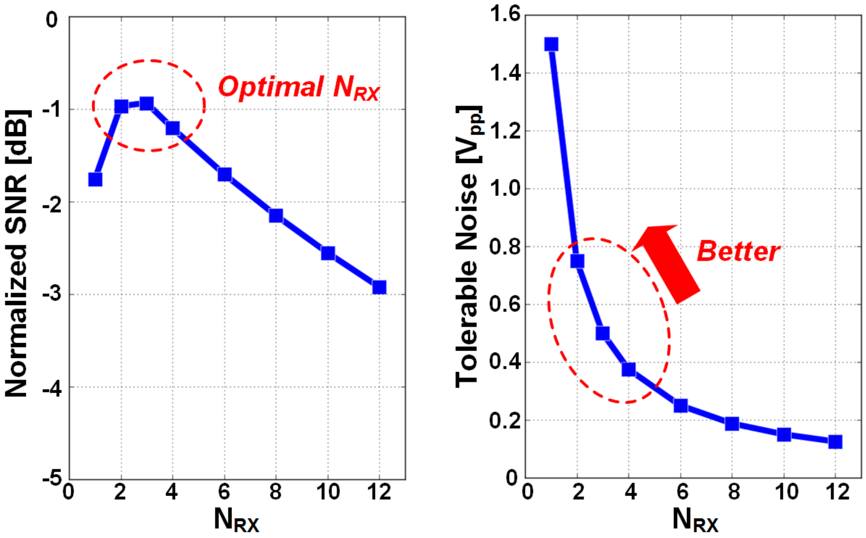

Fig. 4.51 Normalized SNR (left) and tolerable peak-to-peak noise amplitude (right) versus N_{RX}.

(HM-2). The two output of the differential sensing block are encoded with HM-2, and then the encoded signals are added at the analog adder block. The modulated signal is then passed through the low-pass filter, ADC, and decimation filter. After that, the digital demodulation block extract the two capacitance signal by decoding the ADC output with inverse HM-2 sequence.

In the prior work in [4.6], a modulation process was applied to the RX sensing channel. However, the modulation process in [4.6] occurs ahead of trans-impedance amplifier by summing multiple charge signals. Thus, it is vulnerable to the noise interference. The structure in [4.6] used the 2D modulation scheme that the RX modulation sequence cannot be chosen independently, and this imposes additional constraints. On the contrary, the proposed RX modulation method encodes the filtered capacitance data, preventing distortion during the modulation process. The modulation sequence can be chosen independently in disregard of the TX modulation sequence, relaxing the constraint on the design of the RX sensing structure.

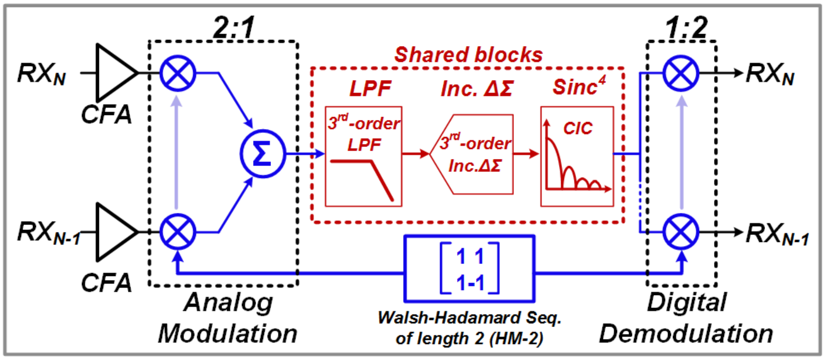

Fig. 4.52 Block diagram of the RX modulation.

4.7 Circuit Implementation

Fig. 4.53 shows the overall block diagram of the AFE. The AFE consists on the TX driving block, RX sensing block, power and reference generator, and digital block. The AFE supports up to 36 TX channels and 64 RX channels. The detail circuit implementation of each block will be discussed in the following sections.

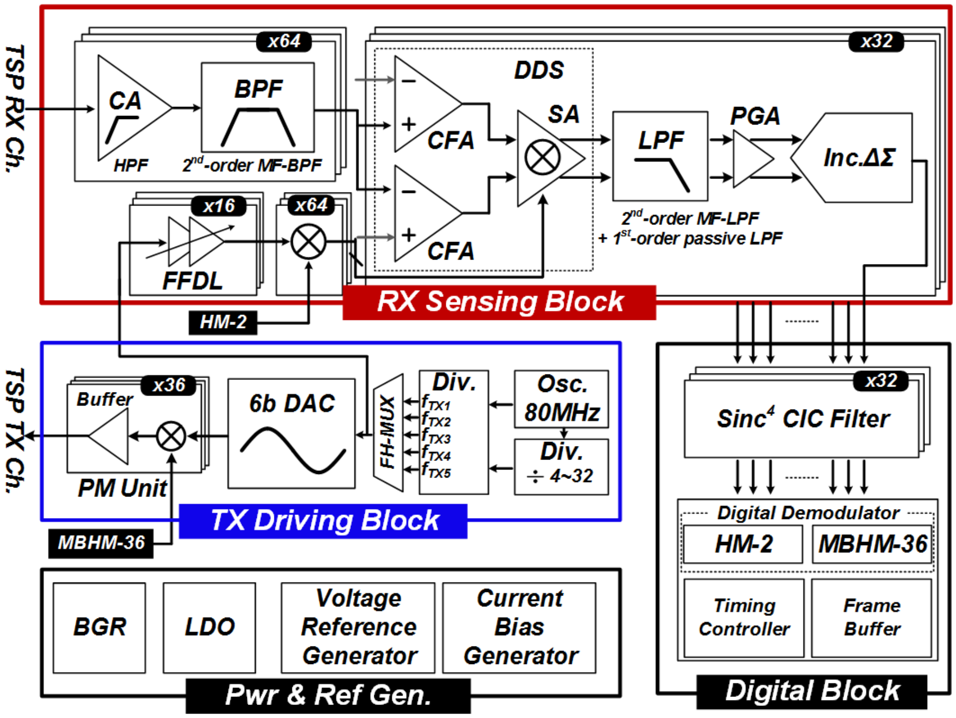

Fig. 4.53 Overall block diagram of the AFE.

4.7.1 Charge Amplifier and Band-Pass Filter

The pre-filtering differential sensing is conducted by the charge amplifier, band-pass filter, and capacitive differential amplifier. The implementation of the pre-filtering differential sensing block is shown in Fig. 4.54. The column-parallel charge amplifiers are connected to the sensing channels of the TSP. The subsequent band-pass filter is also column-parallel structure. To increase the linear output range of the charge amplifier and band-pass filter, the two blocks use higher supply voltage than those of other sensing blocks. The increased output ranges help prevent the saturation by large noise interference. After that, the capacitive feedback amplifier (CFA) performs the differential sensing with two adjacent band-pass filter outputs.

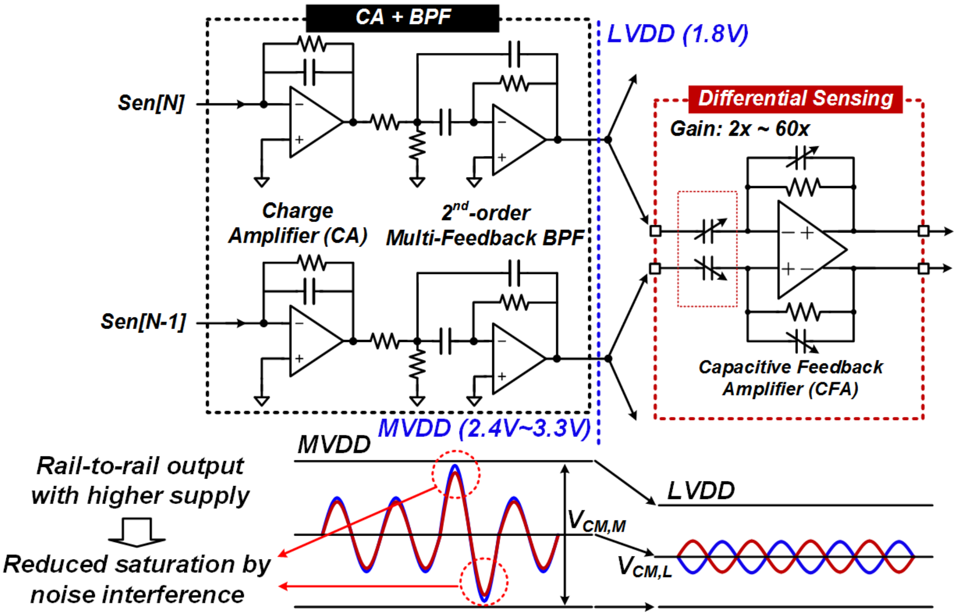

Fig. 4.54 The implementation of the pre-filtering differential sensing block.

The circuit implementation of the charge amplifier is shown in Fig. 4.55. The OTA of the charge amplifier is implemented with rail-to-rail class-AB structure [4.40]. The OTA supports wide supply range owing to the rail-to-rail input stage and use of thick-gate MOSFETs. The feedback resistor R_{FB} and capacitor C_{FB} can be configured digitally. Because R_{FB} and C_{FB} determine the cut-off frequency of the

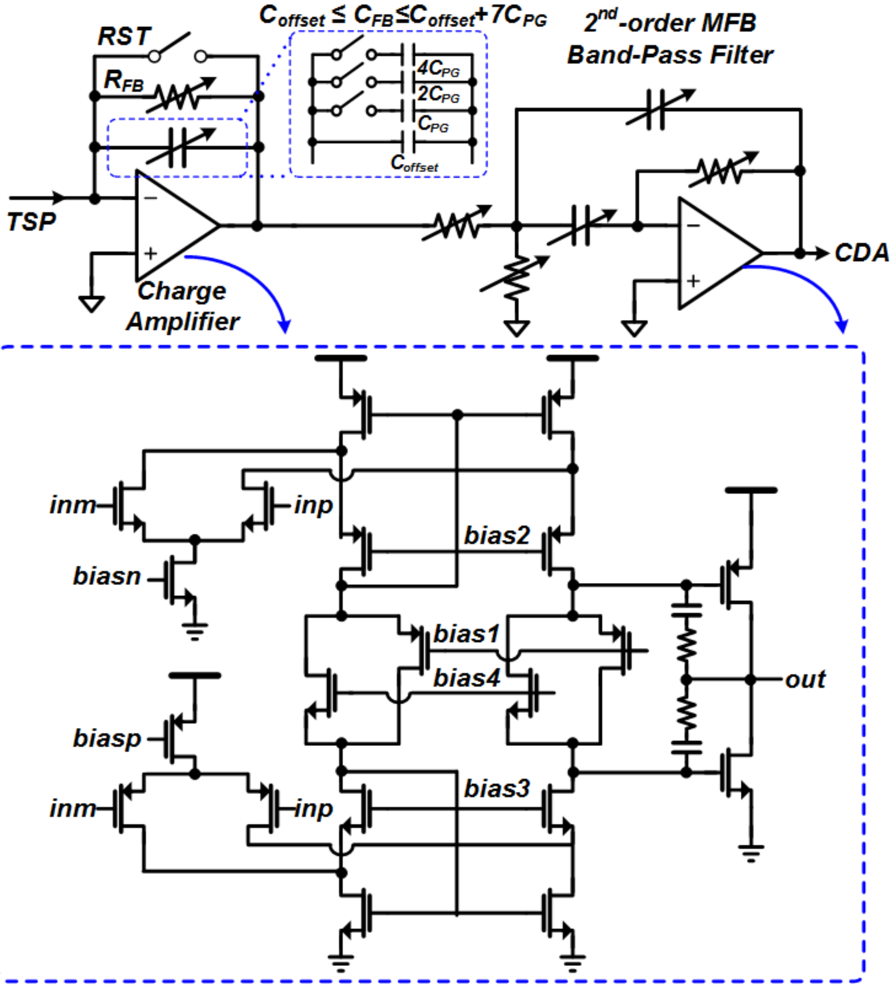

Fig. 4.55 The circuit implementation of the charge amplifier and band-pass filter.

high-pass filtering of the charge amplifier, the programmable range of R_{FB} and C_{FB} are determined with consideration of the cut-off frequency. According to Eq.(3.3.1), the noise contribution of the OTA is inversely proportional to C_{FB}. Therefore, the capacitance of C_{FB} can be increased to larger than 20 pF.

The band-pass filter is implemented with 2nd-order multiple-feedback (MFB) structure. As shown in Fig. 4.55, the band-pass filter is implemented with single-OTA structure, which OTA is same with that of the charge amplifier. The center frequency of the band-pass filter has to be equal to the frequency of the TX driving signal. Thus, the tunable range of the center frequency includes the frequency range from 100 to 500 kHz.

4.7.2 Capacitive Differential Amplifier

The capacitive differential amplifier (CDA) performs the differential sensing. Therefore, it is implemented with fully differential structure. Fig. 4.56 shows the circuit implementation of CDA. In order to support a programmable gain of G_{Diff}, the input and feedback configurations are programmable capacitor arrays. Because he gain G_{Diff}, is the capacitance ratio between C_{IN} and C_{FB}, the two capacitors are designed as 4-bit programmable capacitor array. The configurable range of G_{Diff} is from 2 to 60.

The OTA of CDA is designed as two-stage cascode OTA with rail-to-rail input stage. The difference between two band-pass filter outputs appears at the peak voltage of the input signals. Due to the capacitive configuration and fully differential structure, the input nodes of *inp* and *inm* can be changed in large swing range. For those reasons, the rail-to-rail input stage is employed. To achieve a constant-g_m input stage, the g_m-controller [4.40] implemented with the current mirror is added to the input stage.

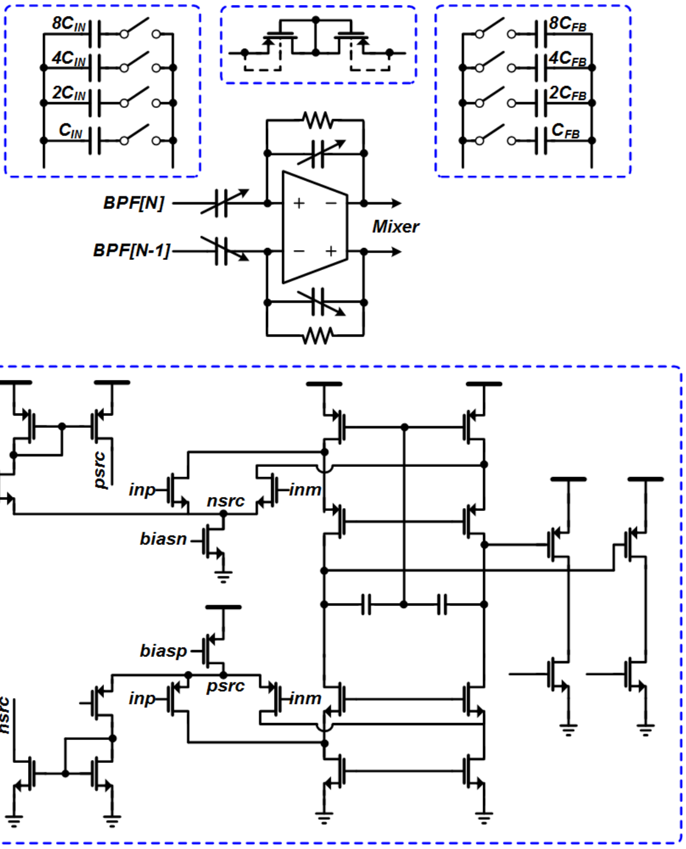

Fig. 4.56 The circuit implementation of CDA.

4.7.3 Mixer and RX Modulation

Fig. 4.57 shows the implementation of the mixer and RX modulation block. The mixer performs the direct conversion from f_{TX} to DC and encodes the down-converted signal with the RX modulation sequence. Then, the encoded signals are added at the summing amplifier. Therefore, the mixer and summing amplifier conducts the RX modulation. The RX modulated signal is then delivered to the low-pass filter and ADC.

The mixer multiplies CDA outputs with the reference signal, which frequency is same with that of the TX driving signal. At this time, the phase of CDA output and reference signal has to be aligned. However, the driving and sensing channels of the large-size TSP have parasitic resistance and capacitance. As the TX driving signal goes through the TSP, the signal is delayed due to the parasitic resistance and capacitance. Because the phase delay results in distortion at the mixer, it is important to match the relational phase between the capacitance signal and the reference signal of the mixer. Hence, this work adjusts the phase of the reference signal using the 3-bit

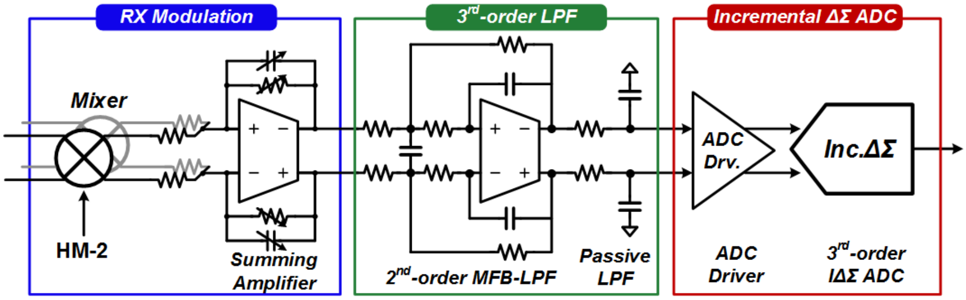

Fig. 4.57 Implementation of the mixer and RX modulation block.

delay line. Fig. 4.58 shows the implementation of the 3-bit delay line, which consists of delay cells that are implemented with flip flops. The delay lines can adjust the phase of reference signal for each four RX channels independently. Therefore, the mixer can convert the frequency of the capacitance signal to DC without the phase mismatch issue regardless of the parasitic of the TSP.

After the direct-conversion process, the RX modulation sequence based on HM-2 encodes the converted signal. Then, the summing amplifier adds the two encoded signals. To configure the gain of RX modulation, the summing amplifier is designed with programmable closed-loop gain. In addition, to provide low-pass filtering for attenuation of the high-frequency harmonic components of the encoded signal, the feedback capacitance and resistor form a low-pass filter.

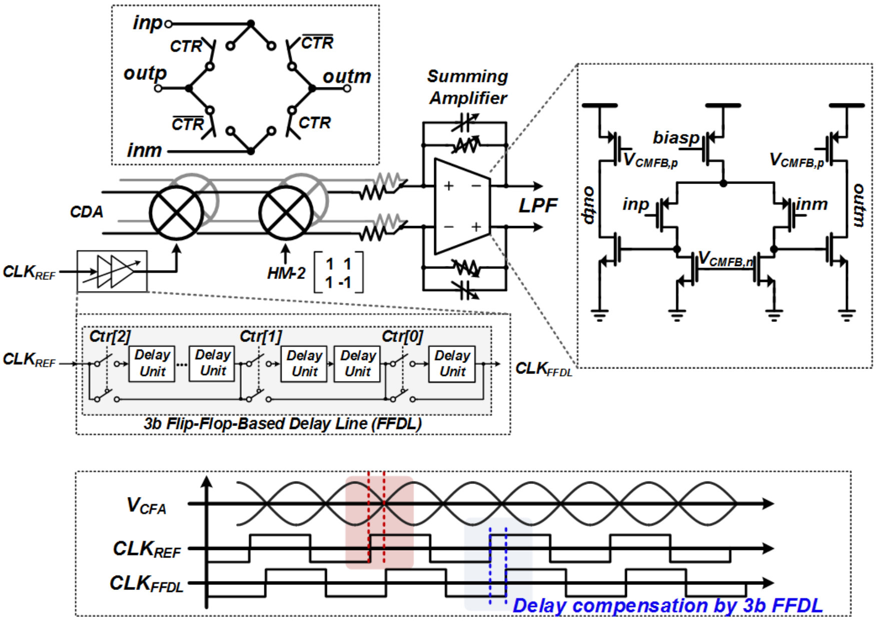

Fig. 4.58 Circuit implementation of the mixer and summing amplifier.

4.7.4 Low-Pass Filter

The 3rd-order low-pass filter is implemented with 2nd-order MFB low-pass filter and 1st-order passive RC filter. Fig. 4.59 shows the circuit implementation of the entire low-pass filter. The MFB structure can be easily implemented as fully differential structure, and the required capacitance of C_1 is halved compared to that of the single-ended structure. In addition, the MFB structure requires only one OTA for the 2nd-order filter, which reduces power consumption and area. For those reasons, this work employs the 2nd-order MFB low-pass filter. The 2nd-order MFB filter provides wide range of tunable cut-off frequency from 30 to 500 kHz. Owing to the wide tuning range, the signal bandwidth can be adjusted properly depending on the noise environment. The 1st-order RC filter further enhances the high-frequency noise attenuation. The cut-off frequency of the RC filter is higher than that of the 2nd-order MFB filter, but it is sufficient to prevent aliasing at the frequency higher than $f_s/2$.

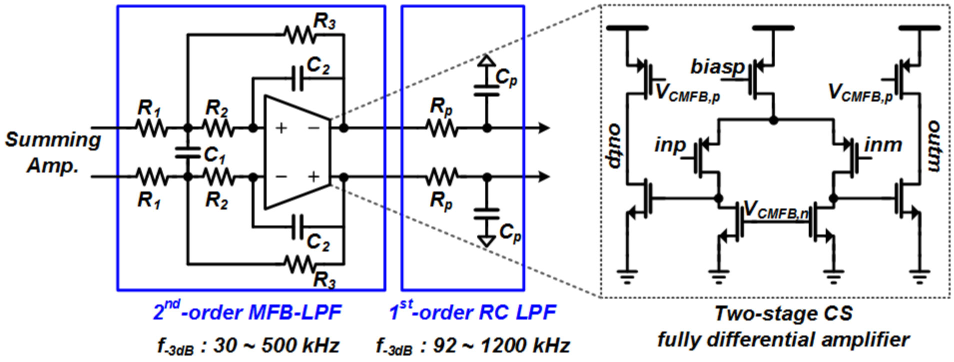

Fig. 4.59 Circuit implementation of the low-pass filter.

4.7.5 Incremental ΔΣ ADC

Fig. 4.60 shows the block diagram of the 3rd-order incremental ΔΣ ADC and Sinc^4 CIC filter. The ΔΣ modulator is implemented with cascaded-integrator-feedforward (CIFF) structure. The CIFF structure provides relatively low distortion [4.42], and the adoption of CIFF structure relaxes the dynamic range constraint of the RX modulation. Although a cascaded-integrator-feedback (CIFB) structure provides a signal transfer function of low-pass filter, the effective bandwidth of the low-pass filtering is impractical to suppress the narrow-band noise interference. Thus, the adoption of the CIFF structure is more advantageous to achieve a reduction of the distortion by the RX modulation rather than low-pass filtering by the CIFB structure.

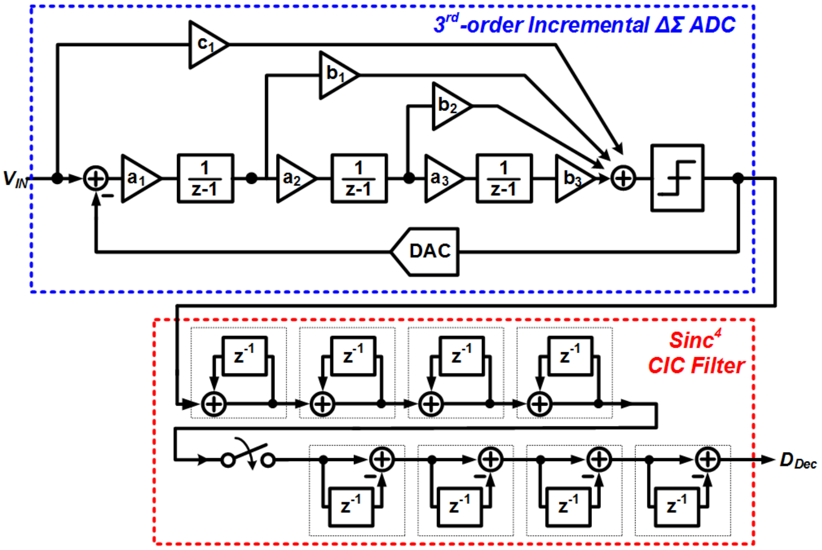

Fig. 4.60 Block diagram of the 3rd-order incremental ΔΣ ADC and Sinc^4 CIC filter.

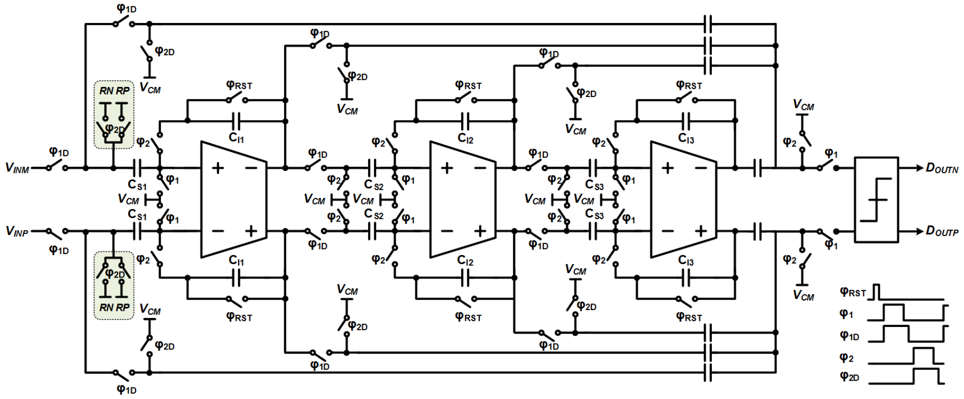

Fig. 4.61 Circuit implementation of the 3rd-order incremental ΔΣ ADC.

Each integrator of the ΔΣ modulator is implemented with a discrete-time switched-capacitor structure. Fig. 4.61 shows the circuit implementation of the ADC. The sampling frequency of the ADC is set to 2.5 MHz. The sampling capacitor of the 1st-integrator is set to 800 fF with a consideration of thermal noise effect. The implemented quantizer is based on the dynamic comparator [4.43].

4.7.6 Digital Demodulation

The demodulation processes of the TX and RX modulations are performed in the digital domain. Fig. 4.62 shows the implementation of the TX and RX demodulation block. First, the decimated data from the ADC are decoded with the inverse HM-2, which corresponds to the RX demodulation. After that, the number of capacitance data of each TX modulation sequence is doubled to 64. The capacitance data are stored in the register in sequence and the TX demodulation is performed simultaneously with the inverse MBHM-36. After the completion of all TX demodulations, total 36 × 64 capacitance data are stored in the frame buffer, which is single frame of capacitance data of the TSP. The frame data are then delivered to the digital back-end for thresholding and labeling processes.

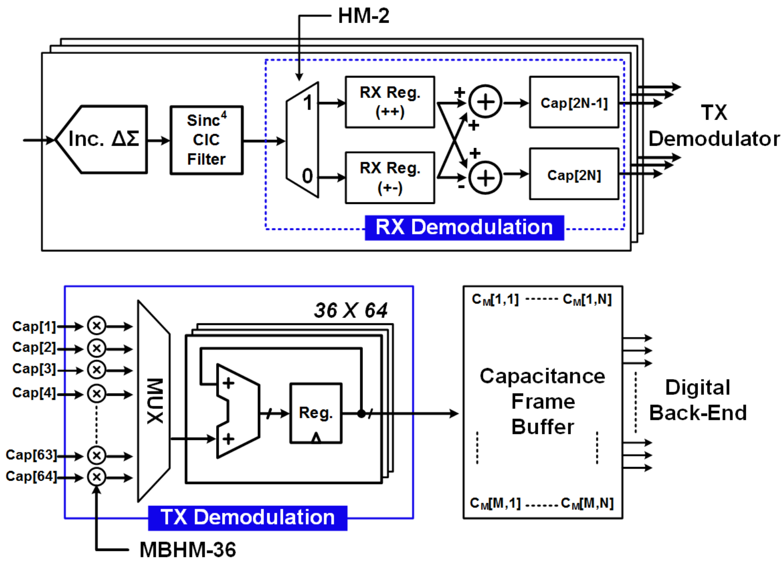

Fig. 4.62 Implementation of the digital demodulators.

4.7.7 TX Driving Block

Fig. 4.63 illustrates the block diagram of the TX driving block. The relaxation oscillator generates the system clock of 80 MHz, and the clock divider provides clocks of multiple frequencies by dividing the system clock. The subsequent frequency multiplexer (FMUX) selects one of the divided frequencies as the frequency of the TX driving signal. The 6-bit capacitive DAC generates differential sinusoidal signals of which frequency is same that of the FMUX output. The two differential-to-single (D2S) converters then make in-phase and out-phase driving signals from the DAC differential outputs. According to the TX modulation sequences of each driving channel, the encoders select one of the in-phase and the out-phase signals. The encoded signals are then fed to the driving channels of the TSP by the rail-to-rail buffer.

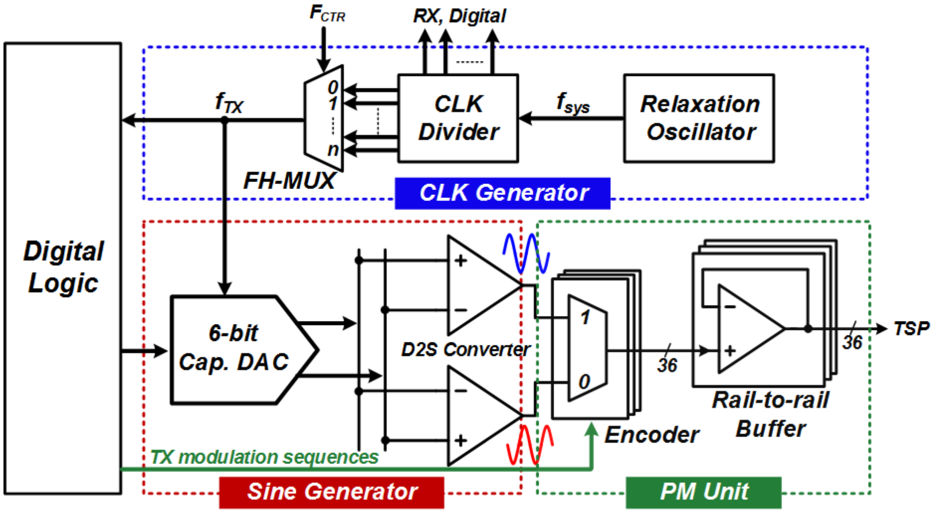

Fig. 4.63 Block diagram of the TX driving block.

4.8 Measurement Results

4.8.1 Touch-Screen Panel (TSP)

The TSP used in the measurement is a mutual-capacitive TSP. The numbers of TX and RX channels of the proposed AFE are 36 and 64, respectively. To verify the operation of the proposed AFE with entire TX and RX channels, the numbers of driving and sensing channels of the TSP were also set to 36 and 64, respectively. The screen size of the TSP was set to 12.2 inches. The electrode pattern of the TSP was designed with diamond pattern. Considering the size of the TSP and the number of TX and RX channels, the pattern pitches of the driving and sensing electrodes were set to smaller than 5 mm.. Fig. 4.64 shows the TSP used in the measurement.

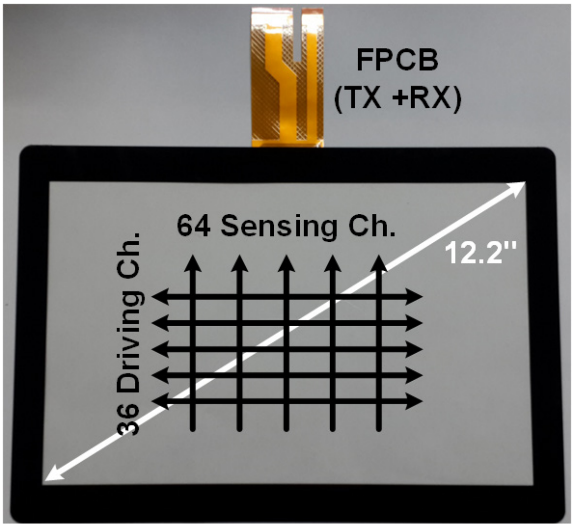

Fig. 4.64 The TSP used in the measurement.

4.8.2 Measurement Environments

Fig. 4.65 shows the measurement setup of the proposed AFE. The measurement setup was composed of the 12.2-inch TSP, evaluation board, FPGA, and noise sources. The 12.2-inch TSP was connected with the evaluation board through the FPCB cable. As the touch object, metal slugs with a number of diameters were used in the measurement. The diameters of the metal slugs are from 1 to 30 mm. The fabricated AFE was mounted on the evaluation board. The fabricated AFE was packaged with 208-pin QFN. The evaluation board was connected to the FPGA. The digital back-end was programmed in the FPGA. The demodulated capacitance data can be measured through logic analyzer or be delivered to the digital back-end in the FPGA.

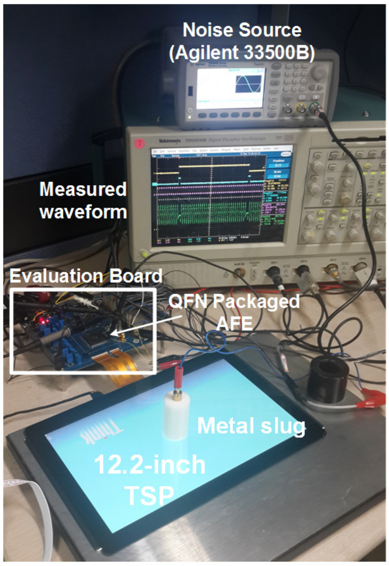

Fig. 4.65 The measurement setup of the fabricated AFE.

4.8.3 Fabricated AFE

Fig. 4.66 shows the die micrograph of the fabricated AFE. The proposed AFE was fabricated in 0.18-μm embedded flash (e-Flash) CMOS process. The total area of the fabricated AFE is 45.6 mm^2, which includes bypass capacitor and I/O pads. The active area of the AFE is about 36 mm^2. The fabricated AFE includes the TX driver of 36 channels, the RX sensing block of 64 channels, the supply generation block, the reference generation block, the digital decimation filter, the digital de-modulators for both of the TX and RX modulation, and the digital timing controller for the configurable SNR and frame rate.

The clock generator and sine generator was implemented in the TX block. The implemented modulation units of 36 channels support configurable TX channels

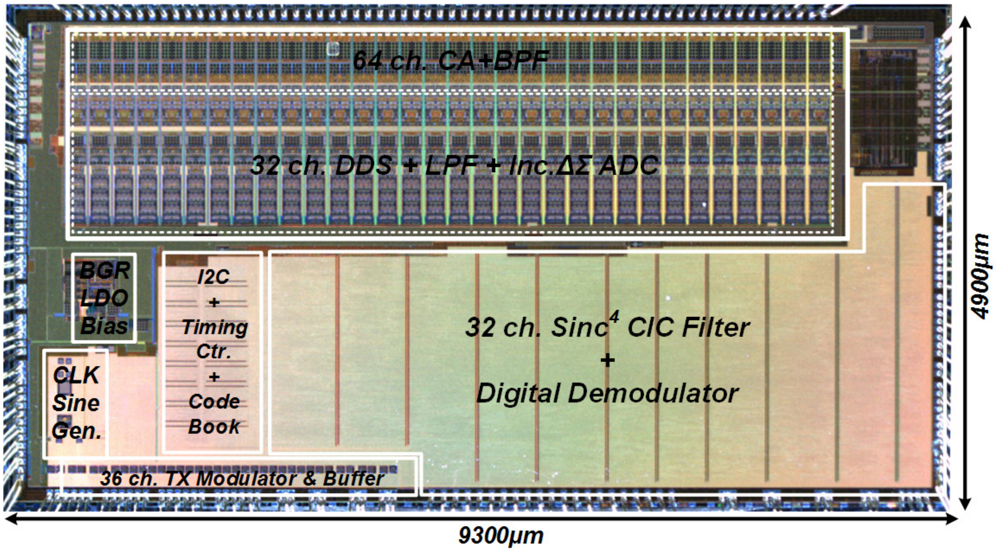

Fig. 4.66 Die micrograph of the fabricated AFE.

from 24 to 36 channels. In the RX sensing block, the CA and BPF of 64 channels were implemented. Owing to the RX modulation, the numbers of CDA, LPF, and the ADC was reduced to half of the numbers of CA and BPF. In the same manner with the TX driving block, the RX sensing block also provides configurable channels from 48 to 64 channels. The LDOs provides analog 1.8-V supply and digital 1.8-V supply. The reference voltage of the LDO comes from the BGR. All reference voltages and current biases were generated on the reference generator block.

The decimation filters of 32 channels were implemented in the digital block. Both of the RX demodulation block and the TX demodulation blocks were included in the digital block. Therefore, the output of the fabricated AFE is the demodulated capacitance variations of each node in the TSP. The timing controller for configurable SNR and frame rate was included in the digital controller. For configuration of the TX and RX sensing block, I2C was implemented. The codebook that stores the modulation matrix was also included in the digital block.

4.8.4 Operation of the Fabricated AFE

The basic operation of the fabricated AFE was verified before the measurement of SNR or noise immunity. Fig. 4.67 shows the measured waveforms of the AFE reset signal (RST), RX modulation control clock (MOD), signal clock (SCLK), and driving signal (TX). All control signals in the AFE are aligned to the RST. The SCLK is divided clock from the system clock of 80 MHz, and it is the frequency of the TX driving signal.

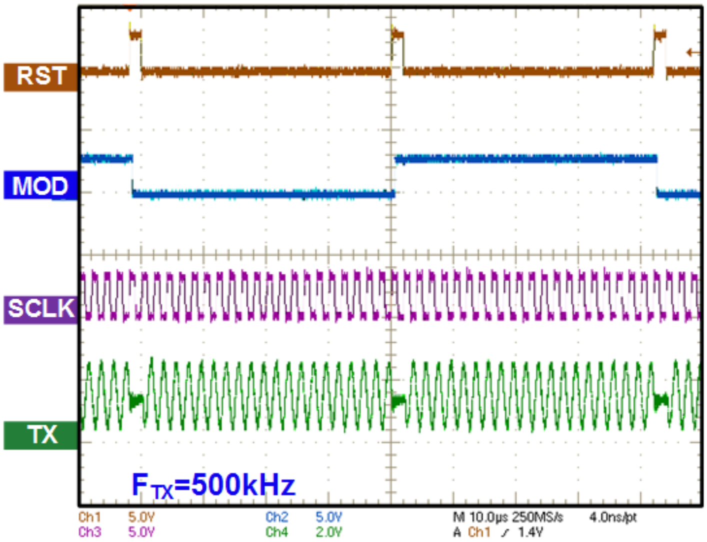

Fig. 4.67 Measured waveforms of the RST, MOD, SCLK, and driving signal.

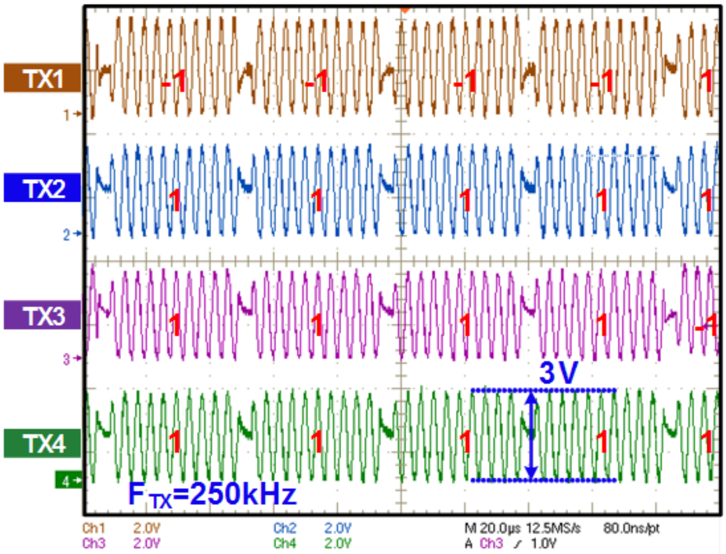

Fig. 4.68 Measured waveforms of the TX driving signals.

Fig. 4.68 shows the measured waveforms of the TX driving signals of four channels. The amplitude of the TX driving signal was set to 3 V_{pp}, and the frequency was set to 250 kHz. The four driving channels, which were not adjacent, show the phase-modulated driving signals according to the modulation matrix.

Fig. 4.69 shows the measured waveform of the RX sensing blocks. The frequency of the TX driving signal is 250 kHz. Through the CA and BPF, low-frequency noise is effectively attenuated. The waveforms of the CDA (DA) show the difference between the untouched signal and touched signal. When the probed RX channel is untouched, the differential output of DA-II is almost zero. When the probed

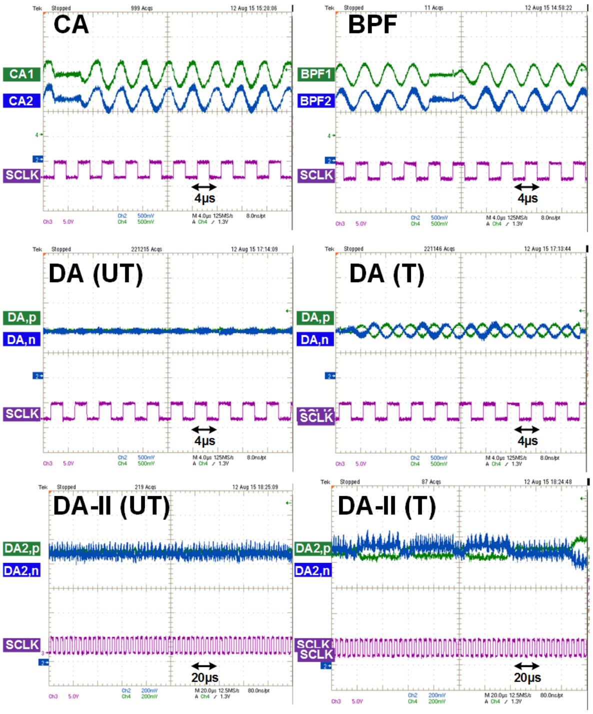

Fig. 4.69 The measured waveforms of the CA, BPF, DA, and DA-II.

RX channel is touched, the output of the DA-II is encoded with the RX modulation sequence. The spikes shown in the DA-II outputs are the result of down-conversion by the mixer, resulting in signals of which frequencies are DC and $2f_{sig}$. The high frequency signal of $2f_{sig}$ is attenuated by the following low-pass filter. Therefore, the ADC receives only the DC capacitance signal that is encoded with the RX modulation sequence.

Fig. 4.70 shows the reconstructed raw capacitance data in 3D image. To verify the multi-touch detection of up to 10 touches, two hands were touched the TSP simultaneously. Each node of the reconstructed capacitance represents the mutual-capacitance variation of corresponding TSP node. All 2304 nodes from 36 TX channels and 64 RX channels were reconstructed in order to verify the capability of TSP entire detection.

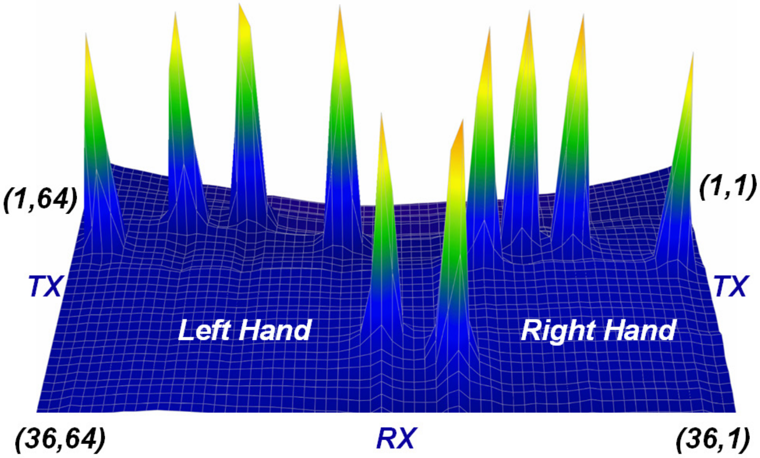

Fig. 4.70 The 3D raw capacitance image after reconstruction.

4.8.5 SNR Measurement

Using the SNR derived in Eq.(2.3.4), the SNR of the fabricated AFE was measured. The frame rate was set to 120 Hz, which is normal operation mode. The touch object was located in the center of the TSP. Fig. 4.71 shows the measured signal difference (top) and noise (bottom) by finger touch. To evaluate the SNR of the AFE, the capacitance difference between touched and untouched cases was measured, which corresponds to $Signal_{Diff}$. Then, in the presence of the touch input, the standard deviation of the capacitance signal during 100 frames was also measured. This corresponds to $Noise_{Touch}$. As a result, the measured SNR was 54 dB.

4.8.6 Configurable SNR and Frame Rate

The fabricated AFE employs the on-chip controller of the SNR and frame rate. The configurable ranges of the SNR and frame rate are determined by the number of TX driving signal cycles. The on-chip frame controller can adjust frame rate from 85

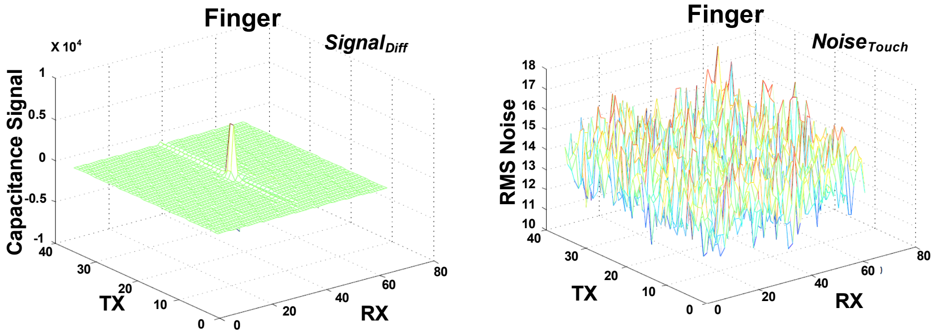

Fig. 4.71 The SNR measurement with finger touch.

to 385 Hz considering the practical range of the frame rate and SNR. Fig. 4.72 shows the measured waveforms of the reconfigured TX driving cycles to adjust the SNR and frame rate.

Using the TX driving signal of 500 kHz, frame rate of 120 Hz was achieved with 56 cycles (left figure). On the other hand, frame rate of 240 Hz was achieved with 28 cycles (right figure). In the same manner, the on-chip frame controller scales the frame rate from 85 to 385 Hz depending on the TSC requirements or noise environments.

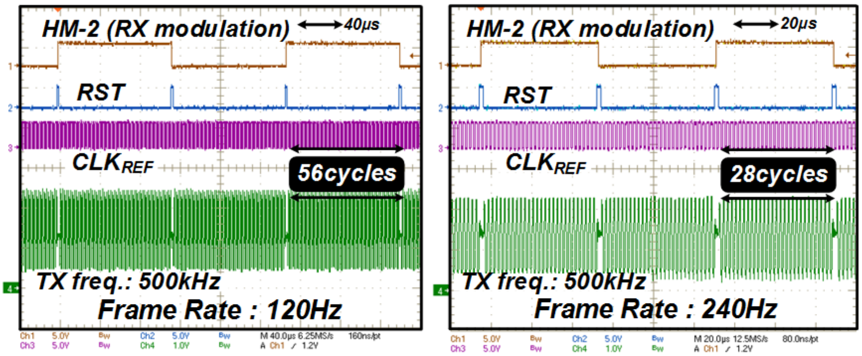

Fig. 4.72 The measured waveforms of the reconfigured cycles to adjust SNR and frame rate

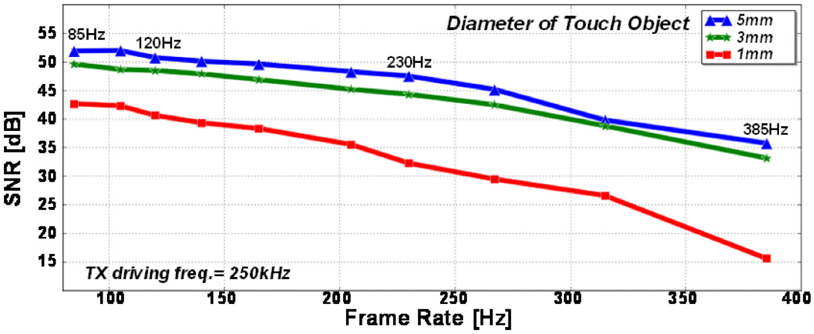

Fig. 4.73 Measured SNR versus frame rate with small diameter touch objects.

Fig. 4.73 shows the measured SNR by adjusting the frame rate. As the touch object, small diameter touch objects were used: 1-mm, 3-mm, and 5-mm diameter touch objects. As increasing the frame rate, the measured SNRs are decreased due to the reduced sampling cycles and widen filtering bandwidth. On the contrary, as decreasing the frame rate, the measured SNR are improved owing to the enhanced noise filtering. At the frame rate of 120 Hz, the measured SNRs with 1-mm diameter and 5-mm diameter touch objects were 41 dB and 51 dB, respectively.

4.8.7 Noise Immunity

The noise immunity of the AFE is the most important specification, but no previous work had investigated the noise immunity quantitatively. In the industry, each company uses their own methods to evaluate the noise immunity of the TSC [4.27]. However, the noise immunity of the AFE has not explored in the industry, too. Measurement standards or specifications have not been defined yet. Therefore, it is required to define a new method that quantifies the noise immunity of the AFE. According to the measurement method of the noise immunity of the entire TSC in [4.27], the noise immunity is defined as the occurrence of false touch by the external noise interference. Thus, in order to define the noise immunity of the AFE, two conditions on noise injection method and criteria of false touch have to be established.

In case of the noise injection method, a pulse signal or sinusoidal signal is injected through metal slug, and the amplitude and frequency of the injected signal are swept to investigate the immunity. In this work, a sinusoidal signal was used to quantify the noise immunity at each noise frequency. Considering the noise frequen-

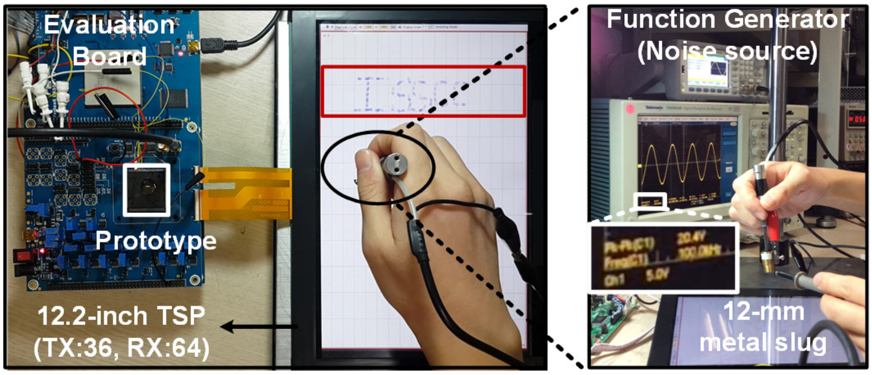

Fig. 4.74 The measurement setup for the noise immunity test.

cy in the real touch environment, the frequency of the injected signal was swept from 1 kHz to 1 MHz. The amplitude of the signal was swept from 0.1 to 20V_{pp}. The total noise interference injected to the TSP is proportional to the size of the metal slug. In order to conduct a strict noise test, a 12-mm diameter metal slug was used as finger model, which is larger than general finger model with diameter of 6 or 8 mm. Thus, the noise injection method used in this immunity test is much harsh condition than the real touch environment as shown in Fig. 4.74.

The false touch in the TSC can be defined as touch detection without real touch. The detection error usually occurs due to the noise interference. Therefore, the existence of the false touch means that the TSC fails to detect the touch input correctly in the noisy interference. In other words, the false touch detection can be regarded as the noise immunity. The noise immunity test in [4.27] also uses the false touch detection as the criterion. However, the AFE just provides the capacitance data of each node in the TSP. The false touch detection requires the digital back-end and coordinates extraction algorithms, but it cannot evaluate the performance of AFE accurately due to the dependence on the digital algorithms.

Hence, new criteria for determination of the false touch are required to the AFE. The fundamental sources of the false touch can be summarized in large variation in touch signal $Signal_{Diff}$ and significant noise interference $Noise_{Touch}$. If the variation of the touch signal exceeds the threshold of labeling process, untouched node can be as touched node and vice versa. Therefore, to prevent the false touch detection, the variation of $Signal_{Diff}$ have not to exceed the threshold value at the labeling process. There is no standard procedure to determine the threshold value at the labeling process, but the threshold is usually set depending on the noise-free touch signal $Signal_{Diff}$. Fig. 4.75 shows the thresholding procedure in the digital backend. Usually, the threshold value that determines the touch or untouch event is set to half of $Signal_{Diff}$. In this case, the variation of $Signal_{Diff}$ may be tolerable up to half of $Signal_{Diff}$. Some works like [4.28] use a hysteresis that makes a gap be-

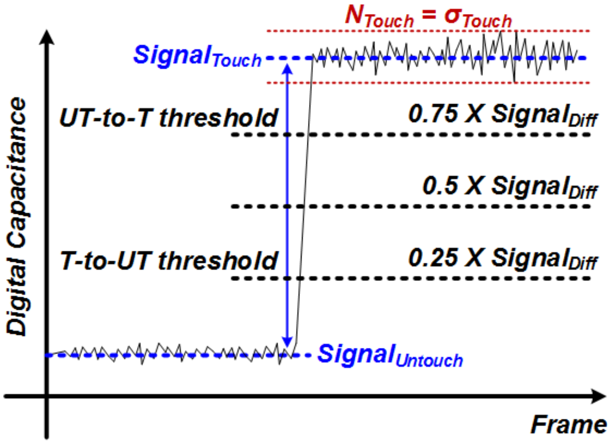

Fig. 4.75 Illustration of the thresholding procedure to determine touch and untouch events in [4.28].

tween touch-to-untouch (T-to-UT) threshold and untouch-to-touch (UT-to-T) threshold. In this case, the variation of $Signal_{Diff}$ can be tolerable with wide range, but the initial thresholds of touched and untouched events are still narrow as 75% of $Signal_{Diff}$ for touched events and 25 % of $Signal_{Diff}$ for untouched events [4.28].

Considering the above implementations of the thresholding procedure, the acceptable variation range of $Signal_{Diff}$ is set to 20 % from its nominal value as shown in Fig. 4.76. The 20 % of $Signal_{Diff}$ is very strict tolerance among the described methods. If the variation of $Signal_{Diff}$ is larger than 20 % of this nominal value, then the touch detection is regarded to fail at the given noise frequency and amplitude. By limiting the acceptable range of $Signal_{Diff}$ variation, the false touch detection by thresholding error at the labeling process can be predicted with only the AFE. Furthermore, the criterion on $Signal_{Diff}$ also compensate the SNR limitation in the noisy environment. If the significant noise interference distorts the AFE, both

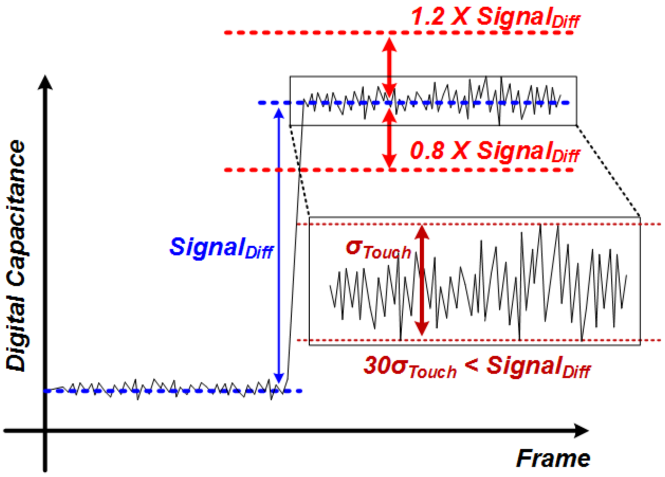

Fig. 4.76 The criteria on the noise immunity of the AFE.

of $Signal_{Diff}$ and $Noise_{Touch}$ can be increased, resulting in a constant SNR. Thus, even if the SNR is maintained (or increased), false touch detection can occur in the noisy environment. The use of only SNR cannot make up for the problem, but the criterion on $Signal_{Diff}$ can cover the fallacy of SNR.

Even though the variation $Signal_{Diff}$ is less than 20%, the false touch can occur if the noise of the capacitance signal is too large to calculate the exact touch coordinate. For this reason, another criterion is required to define the false touch detection. Owing to the criterion on $Signal_{Diff}$, the SNR can be used as representative of the noise performance at given $Signal_{Diff}$. Therefore, another criterion for the false touch detection is defined in terms of the SNR.

In order to determine a criterion on SNR that decides the false touch detection, let us assume that the capacitance data of the TSP show a normal distribution as described in [4.28]. Then, the noise of the SNR is regarded as standard deviation

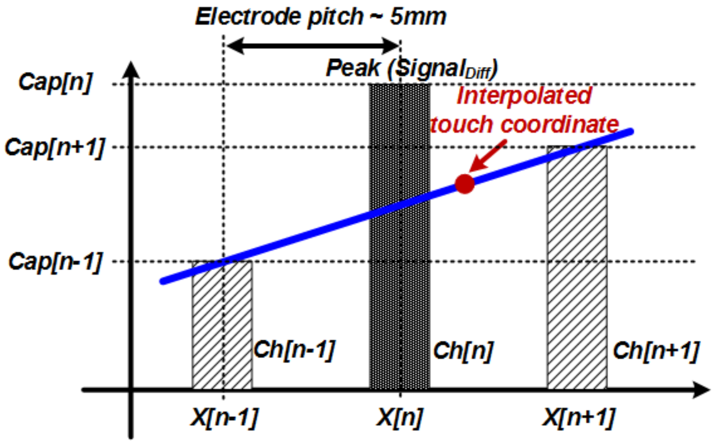

Fig. 4.77 The linear interpolation algorithms to calculate the touch coordinate in [4.29].

(σ_{Touch}) of the normal distribution. Let us explore the touch coordinate calculation [4.29]. There are many algorithms to calculate the touch coordinate. Among the calculation algorithms, a linear interpolation method is the most basic way to extract the coordinate [4.29]. At this time, the required specifications of the accuracy and precision of the TSC are usually less than 1 mm, respectively. Thus, based on the linear interpolation as described in [4.29] and the specification on the precision and accuracy, the required SNR boundary can be derived. Fig. 4.77 shows the linear interpolation algorithm. When the electrode pitch is about 5 mm, the interpolated touch coordinate can be calculated as following:

$$X_{TOUCH} = X[n] + \frac{5mm}{2} \times \left(\frac{Cap[n+1] - Cap[n-1]}{Cap[n]} \right), \tag{4.6.16}$$

where $Cap[n]$ is the sensed capacitance of $Ch[n]$ and $X[n]$ is the coordinate of $Ch[n]$. Using the 1-mm specification as described above, the false touch detection can be defined as $\Delta X_{TOUCH} > 1mm$. Then, let us assume that the $Cap[n-1]$ and $Cap[n+1]$ can be varied up to $6\sigma_{\text{Touch}}$, which includes almost peak-to-peak variation of capacitance data. Thus, the worst deviation within the acceptable precision and accuracy can be formulated as

$$\Delta X_{TOUCH} = 2.5mm \times \left(\frac{6\sigma_{Touch} - (-6\sigma_{Touch})}{Cap[n]} \right) < 1mm. \tag{4.6.17}$$

At this time, $Cap[n]$ is the peak value of the sensed capacitance, and it is same with $Signal_{T-UT}$. Therefore, Eq.(4.6.17) delivers the relationship between $Signal_{T-UT}$ and σ_{Touch} as following:

$$30\sigma_{Touch} < Signal_{T-UT}. \tag{4.6.18}$$

Hence, the acceptable range of the variation of capacitance data can be set to 1/30 times of $Signal_{T-UT}$, and this criterion guarantees the operation of TSC with the significant noise interference. As a result, the required SNR for decision of false touch detection with only AFE can be set to 30:1 using the relationship in Eq.(4.6.18). According to [4.27], the lower bound of SNR that prevent false touch detection by the noise interference is defined as 5:1 with peak-to-peak noise. In terms of the RMS noise, the equivalent SNR is about 30:1 ~ 35:1 because the peak-to-peak noise is usually larger than the RMS noise about six or seven times. In addition, many low-end TSC products in industry show the SNR of 30:1 without any noise injection. Therefore, it is reasonable to claim that the SNR of 30:1 is sufficient condition to provide correct touch detection, which is in accord with the result in the above derivation. In summary, the occurrence of false touch detection by the injected noise interference is defined as following criteria:

$$\begin{aligned}&\text{Criterion 1:}\\&\Delta Signal_{Diff} = \left(\frac{\left|Signal_{T-UT,NI} - Signal_{T-UT}\right|}{Signal_{T-UT}}\right)\times 100\% > 20\%.\\&\text{Criterion 2:}\\&SNR = \frac{Signal_{T-UT}}{\sigma_{Touch}} < 30.\end{aligned} \tag{4.6.19}$$

Using the two criteria, the noise immunity of the fabricated AFE was measured. For reference, most of the digital back-ends employ an additional digital filtering block to attenuate the noise interference, but this work evaluate the noise immunity of the AFE without any digital filtering except the decimation filter of the ADC.

Fig. 4.78 shows the measured SNR when the sinusoidal signal was injected through the metal slug of 12-mm diameter. The frequency of the injected signal was swept from 1 kHz to 1 MHz. The amplitude of the injected signal was swept from 0.01 to 20 V_{pp}. At this time, the frequency of the TX driving signal is 250 kHz. The measured SNR shows that the fabricated AFE sustains up to 20-V_{pp} noise injection without the SNR degradation in the frequency range from 1 to 100 kHz. As mentioned in the previous chapter, the frequency range from 1 to 100 kHz is the most noisy band. At the frequency of the 250 kHz, which is the frequency of the TX driv-

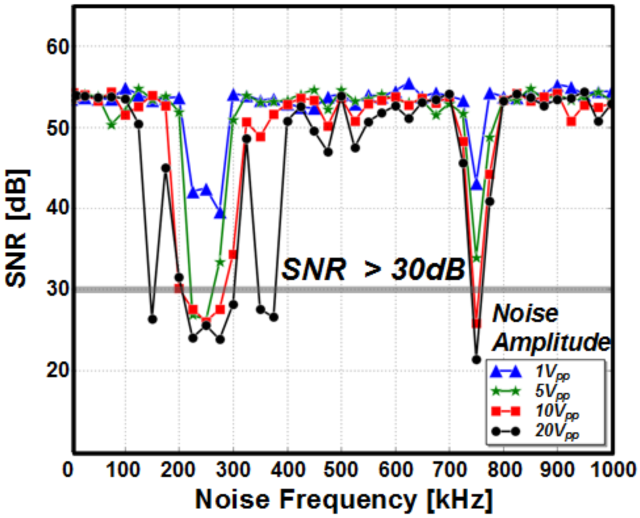

Fig. 4.78 The measured SNR versus the frequency and amplitude of the injected noise (sinusoidal signal)

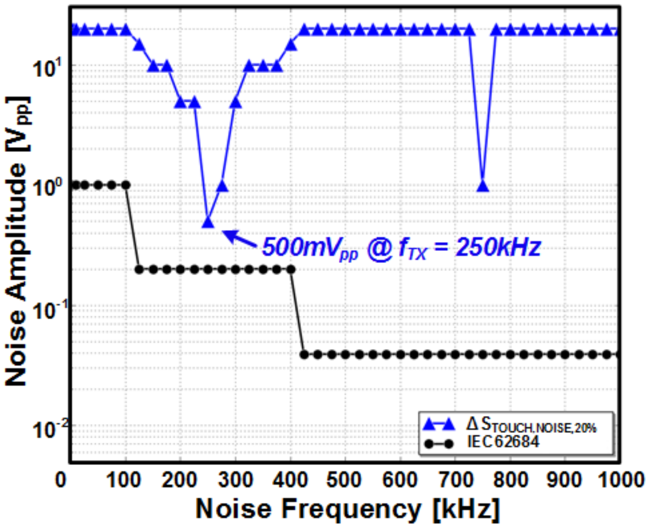

Fig. 4.79 The measured noise amplitude that satisfies the criterion on the variation of the capacitance signal depending on the frequency of the injected signal.

ing signal, the measured SNR is reduced significantly because the noise interference cannot be attenuated sufficiently. At the frequency of 750 kHz, the measured SNR is also reduced significantly. As explored in the previous section, the down-conversion process at the mixer odd harmonic components of the modulated signal. Thus, the 3^{rd}-order harmonic frequency of the TX driving signal is also folded into the signal band. However, the noise interference with frequency higher than 500 kHz is negligible compared to the frequency lower than 500 kHz. Thus, the odd harmonic folding problem at the down-conversion process does not affect the entire noise immunity of the AFE.

Fig. 4.79 shows the measured noise amplitude that satisfies the criterion on the variation of the capacitance signal. The noise injection is same with that of the SNR measurement. The acceptable noise amplitude that satisfies the criterion of the signal variation is 20 V_{pp} against the noise frequency lower than 100 kHz. Hence, the fabricated AFE fulfills the two criteria of the signal variation and SNR with respect to the noise frequency lower than 100 kHz and amplitude of up to 20 V_{pp}. The frequency range from 100 to 400 kHz, the acceptable noise amplitude is reduced to 500 mVpp. In the same manner with the SNR measurement, the acceptable noise amplitude at the 3rd-order harmonic frequency is also reduced due to the folded harmonic components. Compared to the IEC62684 standard, the smallest noise amplitude is still larger than the specified noise amplitude in the standard [4.3], which implies sufficient immunity of the fabricated AFE even in the worst case.

To quantify the immunity of the AFE against the noise interference, two figure-of-merits are newly defined: noise tolerance and noise immunity. The noise tolerance is defined as the minimum noise amplitude that satisfies both of the criteria on the occurrence of the false touch detection. In other words, the noise tolerance means the maximum noise amplitude that provides normal touch detection by the AFE. The nose tolerance was measured for each TX driving frequency concerning the frequency of the injected noise. Fig. 4.80 shows the measured noise tolerance of the TX driving frequency of 250 kHz. At the frequency lower than 100 kHz, the measure noise tolerance is 20 V_{pp}. At the frequency of 250 kHz, which is the frequency of the TX driving signal, the noise tolerance is reduced to 500 mV_{pp} due to the criterion on the signal variation as shown in Fig. 4.79. Although the noise tolerance is reduced, it is still better than that of IEC62684 specification. At the frequency of 750 kHz, which is the 3rd-order harmonic frequency of the TX driving signal,

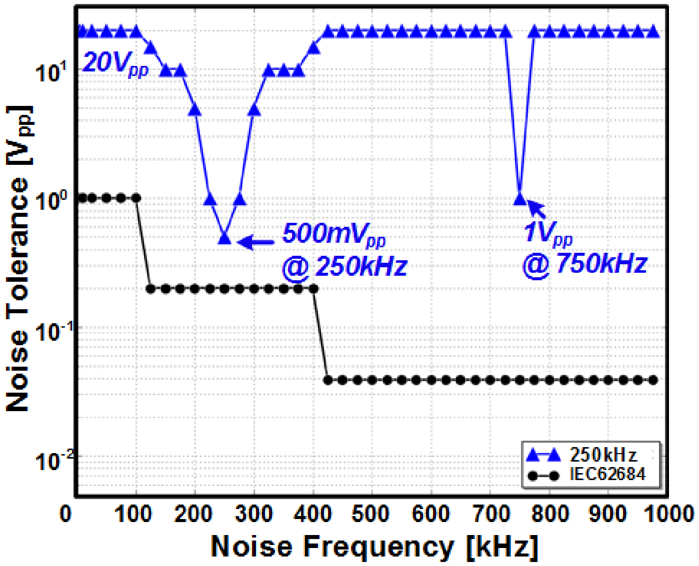

Fig. 4.80 The measured noise tolerance with the TX driving frequency of 250 kHz.

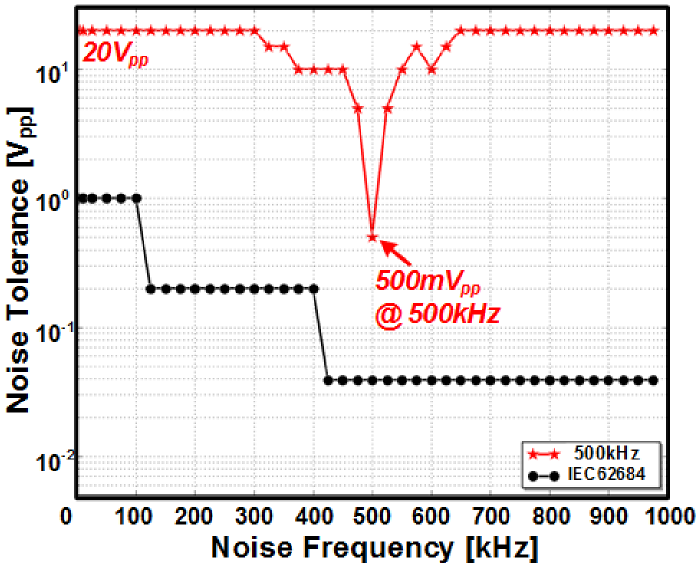

Fig. 4.81 The measured noise tolerance with the TX driving frequency of 500 kHz.

the noise tolerance is also reduced to 1 V_{pp}. This results from the down-conversion process as explained above.

In the same manner with the noise tolerance of 250-kHz TX driving frequency, the noise tolerance of 500-kHz TX driving frequency was measured as depicted in Fig. 4.81. Likewise, the noise tolerance at the frequency lower than 100 kHz is 20 V_{pp}. When the frequency of the injected noise and TX driving signal is same, the noise tolerance is reduced to 500 mVpp, which is still larger than that of IEC62684 specification.

In summary, the noise tolerance indicates the maximum noise amplitude at the given frequency without any assistance of the digital back-end. The fabricated AFE supports a number of TX driving frequencies, and the noise tolerance of each TX driving frequency shows the immunity to the external noise interference. Within the noise tolerance amplitude, the AFE can detect the touch input without malfunction such as the false touch detection. Both of the noise tolerances of the TX driving frequencies of 250 and 500 kHz are maintained with 20 V_{pp} at the frequency lower than 100 kHz. Therefore, the fabricated AFE can operate in the presence of the severe noise interference such as lamp or display noise. The fabricated AFE also maintains the high noise tolerance larger than 10 V_{pp} even at the frequency higher than 100 kHz except the TX driving frequencies.

In the TSC, which consists of the AFE and DBE, the frequency hopping technique is usually employed to avoid the noisy frequency [4.45]. Thus, it is more realistic to use a figure-of-merit that takes into account of the noisy frequency avoidance technique by the DBE. Assuming the frequency hopping technique, a noise immunity of the AFE is defined as the maximum noise tolerance at each noise frequency with the assistance of the DBE. When the frequency hopping technique is employed in the TSC, the noise immunity can be improved as increasing the number of available TX driving frequencies. Therefore, to minimize the effect of the DBE assistance, only two frequencies of 250 and 500 kHz among a number of TX driving frequencies from 100 to 500 kHz were used in the measurement of the noise immunity.

Fig. 4.82 shows the measured noise immunity of the fabricated AFE with the TX frequencies of 250 and 500 kHz. Even if the frequency of the injected noise is overlapped with the frequency of the TX driving signal, the noise immunity of the AFE can be maintained through the frequency hopping technique that changes the TX driving frequency away from the noise frequency. Because both of the noise tolerances of 250 and 500 kHz TX driving frequencies were 20 V_{pp}, the measured noise

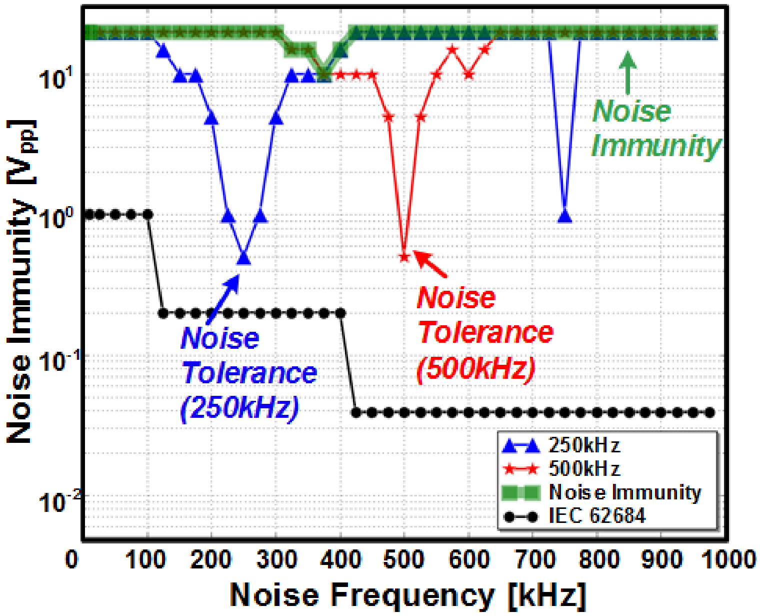

Fig. 4.82 The measured noise immunity with 250 and 500 kHz TX frequencies.

immunity was also 20 V_{pp} at the noise frequency lower than 100 kHz. In addition, 20-V_{pp} noise immunity was also achieved at the frequency higher than 500 kHz. The worst noise immunity of 10 V_{pp} was measured at the noise frequency of 375 kHz. As a result, the fabricated AFE can provide 20-V_{pp} noise immunity in the noisiest band from 1 to 100 kHz. The AFE also achieves noise immunity larger than 10 V_{pp} in the entire noise frequency band from 1 kHz to 1 MHz.

In order to investigate the noise immunity with severe condition, noise immunities with larger touch object with diameter of 30 mm and high frame rate of 315 Hz were also measured. As increasing the size of touch object, the noise interference through the touch object becomes worse due to the increased coupling capacitance. Thus, the noise immunity with large touch object is important to cope with thumb or palm touch cases. Fig. 4.83 shows the measured noise immunity with 30-mm metal slug, which corresponds to the diameter of thumb. The noise immunity at the frequency lower than 100 kHz was maintained with 20 V_{pp}. In the worst case, the measured noise immunity was 5 V_{pp} at the 375 kHz. Compared to the measurement in Fig. 4.82, the worst noise immunity drops to 5 V_{pp}, which is half of the normal condition. This coincides with the assumption that the noise interference is proportional to the size of the touch object. Although the noise immunity decreased, it is still higher than that of IEC62684 specification.

Fig. 4.84 shows the measured noise immunity with frame rate of 315 Hz. As explored in the previous section, the noise filtering at the AFE is inversely proportional to the frame rate. Thus, the attenuation of the noise interference decreased as increasing the frame rate. For this reason, the noise immunity at the high frame rate becomes worse. The measured noise immunity at the frequency lower than 100 kHz was maintained with 20 V_{pp}. However, the worst noise immunity decreased to 1 V_{pp} at the frequency higher than 400 kHz. With same frame rate, the number of sensing cycles of 500-kHz TX frequency is larger than that of 250-kHz TX frequency, and the noise attenuation of 500-kHz TX frequency is better than that of 250-kHz TX frequency. The noise immunity near the frequency of 500 kHz is mainly determined by the noise tolerance with 250-kHz TX frequency. In addition, the noise tolerance of 500-kHz TX frequency would be lower than that of 250-kHz TX frequency at the noise frequency near 500 kHz. As a result, the lowest noise immunity occurs at the frequency near 500 kHz. For this reason, Fig. 4.84 shows the lowest noise immunity of 1 V_{pp} near the frequency of 500 kHz. Nevertheless, the noise immunity is still higher than IEC62684 specification at least 20 times.

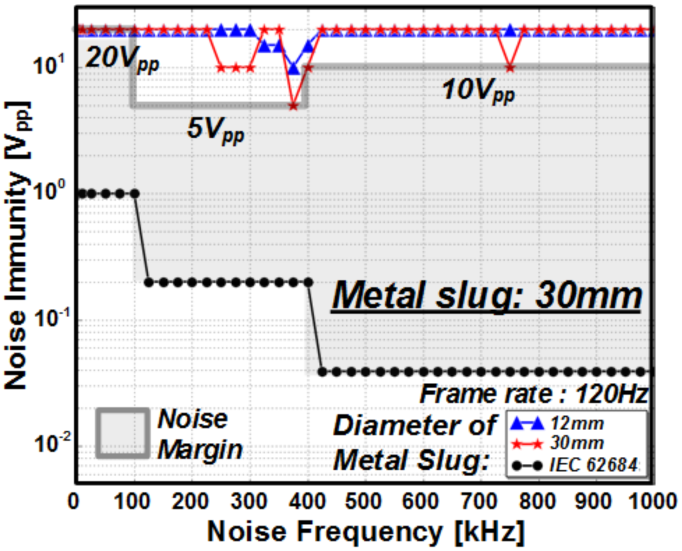

Fig. 4.83 The measured noise immunity with metal slug of 30-mm diameter

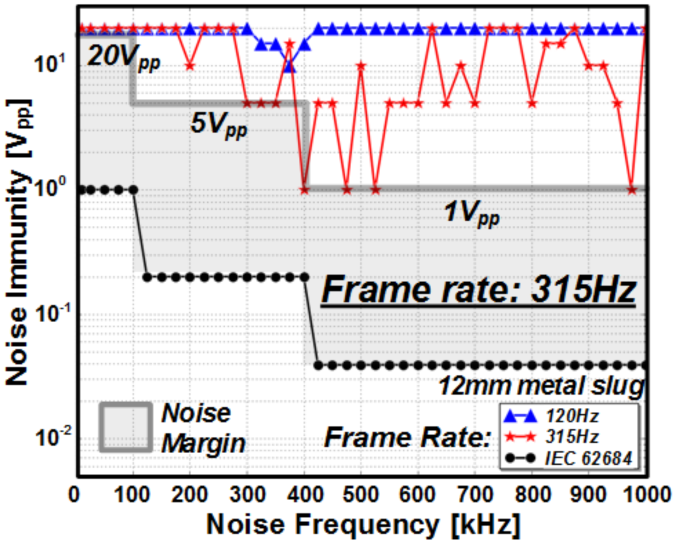

Fig. 4.84 The measured noise immunity with frame rate of 315 Hz.

4.8.8 Comparison with Other Works

Fig. 4.85 shows the comparison with other work [4.2][4.4][4.7][4.20][4.44]. The proposed AFE supports up to 36 TX channels and 64 RX channels. The configurable range of the frame rate is from 85 to 385 Hz. With a finger touch, the proposed AFE provides 54-dB SNR with 120-Hz frame rate. In case of 1-mm diameter touch object such as passive as stylus pen, the achieved SNR is 41 dB at 120-Hz frame rate. Compared to the other works, the noise immunity of the AFE is quantified for the first time, and the achieved nose immunity is up to 20 V_{pp}, which is sufficiently high to be immune against the charger or display noise. The supply of the AFE covers the practical range from 2.7 to 3.3 V. The total power consumption is 94.5 mW with a 3.3-V supply. The active area of the fabricated AFE is 36 mm^2.

		This Work	ISSCC`13 Yang	ISSCC`13 Shin	ISSCC`14 Hamaguchi	ISSCC`15 Park	ISSCC`15 Hamaguchi
Process		0.18μm	0.35μm	0.18μm	0.18μm	0.18μm	85nm
Channel		TX : 36 RX : 64	TX : 27 RX : 43	TX : 30 RX : 24	TX: 78 RX: 138	TX: 48 RX: 32	TX: 35 RX: 57
Frame Rate		85~385Hz	120Hz	240Hz	240Hz	120Hz	240Hz
SNR	Finger	54dB	39dB	55dB	56.6dB	62dB	-
	1mm Diameter	41dB	-	35dB	37.4dB	49dB	38dB
Noise Immunity	1kHz ~100kHz	$20V_{pp}$	-	-	-	-	-
	100kHz ~400kHz	$10V_{pp}$					
	400kHz ~1MHz	$20V_{pp}$					
Supply		2.7~3.3V	-	2.5~3.3V	1.8/3.3V	-	1.2/3.3V
Power		94.5mW	18.7mW	52.8mW	559.9mW	30mW	-
Area		$36mm^2$	$10.4mm^2$	$14.9mm^2$	$71.2mm^2$	$14.7mm^2$	$12.5mm^2$

Fig. 4.85 Comparison with other works.

Chapter 5

Conclusion

In this thesis, the AFEs with highly enhanced noise immunity and configurable SNR and frame rate are proposed. First, the AFE for mobile TSC provides configurable SNR and frame rate. The employed incremental ΔΣ ADC provides over-sampling and averaging effect, and it enables the configurable noise power of the AFE. The relationship between the SNR and frame rate is derived using the configurable noise power. Hence, the AFE controls the number of sampling cycles per conversion at the ADC, achieving the configurable SNR and frame rate. The test chip is fabricated in a 0.18-μm CMOS process. In the measurements with TSP of 12 × 8 channels, the fabricated AFE achieves an SNR from 40 to 67 dB and a frame rate from 50 Hz to 6.4 kHz. The fabricated AFE consumes 6.26 mW with a 3.3-V supply.

The AFE for tablet TSC provides highly enhanced noise immunity and the configurable SNR and frame rate. The multi-driving TX structure using the MBHM-36 improves the SNR and noise immunity of the AFE. The effect of the multi-driving

TX structure to the noise immunity of the AFE is investigated, and this work fully exploits the advantage of the multi-driving TX structure to achieve highly enhanced noise immunity. The proposed MBHM-36 resolves the offset and phase delay issues. In addition, the AFE achieves improved noise immunity by supporting a number of TX driving frequencies that enables the frequency hopping technique. The RX sensing block employs the pre-filtering differential sensing method to reject the common-mode noise with preventing the saturation by touch-injection noise. Using the pre-filtering differential sensing method, the AFE acquires noise immunity against both of the common-mode noise and touch-injection noise. The optimal high-order noise filtering structure is explored which suppresses the noise interference effectively. The employed RX modulation applied to the area-consuming RX blocks enables the column-parallel sensing structure without significant SNR degradation and power consumption. The AFE for the tablet TSC also provides configurable SNR and frame rate with on-chip frame-rate controller. The test chip is fabricated in a 0.18-μm CMOS process and occupies a 36-mm^2 active area. A 12.2-inch TSP with 36 TX channels and 64 RX channels was used in the measurement. The test chip achieves a 54-dB SNR and 120-Hz frame rate with a finger touch. The frame rate is able to be adjusted from 85 to 385 Hz. The test chip achieves up to 20-V_{pp} noise immunity. The test chip consumes 94.5 mW from a 3.3-V supply.

Bibliography

[1.1] K.-D. Kim *et al.*, "A fully-differential capacitive touch controller with input common-mode feedback for symmetric display noise cancellation," *in Proceeding of Symposium on VLSI*, Jun. 2014.

[1.2] J. H. Yang *et al.*, "A highly noise-immune touch controller using Filtered-Delta-Integration and a charge-interpolation technique for 10.1-inch capacitive touch-screen panels," *in IEEE ISSCC Dig. Tech. Papers*, 2013, pp. 390-391.

[1.3] H. Shin, S. Ko, H. Jang, I. Yun and K. Lee, "A 55dB SNR with 240Hz frame scan rate mutual capacitor 30×24 touch-screen panel read-out IC using code-division multiple sensing technique," *in IEEE ISSCC Dig. Tech. Papers*, 2013, pp. 388-389.

[2.1] 3M Touch Systems, “Projected Capacitive Technology,” [Online] Available : http://multimedia.3m.com/mws/media/788463O/tech-brief-projected-capacitive-technology.pdf

[2.2] Jun-Eun Park, "Design of high SNR analog front-end circuit for touch screen sensor interface", M.S. thesis, Seoul National University, Feb. 2013.

[2.3] Dong-Hyuk Lim, "Design Considerations of a Low-Noise Frontend for Capacitive Touch Screen Controllers", Ph.D. thesis, Seoul National University, Feb. 2013.

[2.4] N. Miura *et al.*, "A 1mm-pitch 80×80-channel 322Hz-frame-rate touch sensor with two-step dual-mode capacitance scan," in *IEEE ISSCC Dig. Tech. Papers*, 2014, pp. 216-217.

[2.5] T. H. Hwang, W. H. Cui, I. S. Yang and O. K. Kwon, "A highly area-efficient controller for capacitive touch screen panel systems," *IEEE Transactions on Consumer Electronics*, vol. 56, no. 2, pp. 1115-1122, May 2010.

[2.6] S. Ko *et al.*, "Low noise capacitive sensor for multi-touch mobile handset's applications," *in proceedings of A-SSCC*, Nov. 2010, pp. 1-4.

[2.7] M. Miyamoto, M. Hamaguchi and A. Nagao, "A 143×81 Mutual-Capacitance Touch-Sensing Analog Front-End With Parallel Drive and Differential Sensing Architecture," *IEEE J. Solid-State Circuits*, vol. 50, no. 1, pp. 335-343, Jan. 2015.

[2.8] J.-E. Park, D.-H. Lim and D.-K. Jeong, "A Reconfigurable 40-to-67 dB SNR, 50-to-6400 Hz Frame-Rate, Column-Parallel Readout IC for Capacitive Touch-Screen Panels," *IEEE J. Solid-State Circuits*, vol. 49, no. 10, pp. 2305-2318, Oct. 2014.

[2.9] H. Jang, H. Shin, S. Ko, I. Yun and K. Lee, "2D Coded-aperture-based ultra-compact capacitive touch-screen controller with 40 reconfigurable channels," *in IEEE ISSCC Dig. Tech. Papers*, 2014, pp. 218-219.

[2.10] T. Blankenship and T. Wang, "Projected Capacitive Touch Systems from the Controller Point of View," [Online] Available: https://www.maximintegrated.com/en/app-notes/index.mvp/id/5047.

[2.11] H. W. Klein, “Noise Immunity of Touchscreen Devices,” [Online] Available: http://www.cypress.com/file/120641/download.

[3.1] H. Shin, S. Ko, H. Jang, I. Yun and K. Lee, "A 55dB SNR with 240Hz frame scan rate mutual capacitor 30×24 touch-screen panel read-out IC using code-division multiple sensing technique," *in IEEE ISSCC Dig. Tech. Papers*, 2013, pp. 388-389.

[3.2] J. H. Yang *et al.*, "A highly noise-immune touch controller using Filtered-Delta-Integration and a charge-interpolation technique for 10.1-inch capacitive touch-screen panels," *in IEEE ISSCC Dig. Tech. Papers*, 2013, pp. 390-391.

[3.3] J.-E. Park, D.-H. Lim and D.-K. Jeong, "A Reconfigurable 40-to-67 dB SNR, 50-to-6400 Hz Frame-Rate, Column-Parallel Readout IC for Capacitive Touch-Screen Panels," *IEEE J. Solid-State Circuits*, vol. 49, no. 10, pp. 2305-2318, Oct. 2014.

[3.4] J. H. Yang, S. C. Jung, Y. S. Son, S. T. Ryu and G. H. Cho, "A Noise-Immune High-Speed Readout Circuit for In-Cell Touch Screen Panels," *IEEE Trans. Circuits and Syst. I*, vol. 60, no. 7, pp. 1800-1809, July 2013.

[3.5] V. Kremin, and A.Konovalov, “Method and apparatus for, reducing coupled noise influence in touch screen controllers,” U.S. Patent 8,947,373 B2, Oct. 20, 2010.

[3.6] J.-E. Park, D.-H. Lim and D.-K. Jeong, "A 6.3 mW high-SNR frame-rate scalable touch screen panel readout IC with column-parallel Σ-Δ ADC structure for mobile devices," *in proceedings of A-SSCC*, Nov. 2013, pp. 357-360.

[3.7] Jun-Eun Park, “Design of high SNR analog front-end circuit for touch screen sensor interface”, M.S. thesis, Seoul National University, Feb. 2013.

[3.8] Dong-Hyuk Lim, “Design Considerations of a Low-Noise Frontend for Capacitive Touch Screen Controllers”, Ph.D. thesis, Seoul National University, Feb. 2013.

[3.9] D.-H. Lim, J.-E. Park and D.-K. Jeong, "A low-noise differential front-end and its controller for capacitive touch screen panels," *in proceedings of the ESSCIRC*, Sept. 2012, pp. 237-240.

[3.10] S. Ko *et al.*, "Low noise capacitive sensor for multi-touch mobile handset's applications," *in proceedings of A-SSCC*, Nov. 2010, pp. 1-4.

[3.11] K. Lim, K.-S. Jung, C.-S. Jang, J.-S. Baek, and I.-B. Kang, “A fast and energy efficient single-chip touch controller for tablet touch applications,” *IEEE/OSA J. Display Technol.*, vol. 9, no. 7, pp. 520–526, Jul. 2013.

[3.12] J. H. Yang *et al.*, "A highly noise-immune touch controller using Filtered-Delta-Integration and a charge-interpolation technique for 10.1-inch capacitive touch-screen panels," *in IEEE ISSCC Dig. Tech. Papers*, 2013, pp. 390-391.

[3.13] H. Shin, S. Ko, H. Jang, I. Yun and K. Lee, "A 55dB SNR with 240Hz frame scan rate mutual capacitor 30×24 touch-screen panel read-out IC using code-division multiple sensing technique," *in IEEE ISSCC Dig. Tech.* Papers, 2013, pp. 388-389.

[3.14] I.-S. Yang and O.-K. Kwon, "A touch controller using differential sens,ing method for on-cell capacitive touch screen panel systems," *IEEE Transactions on Consumer Electronics*, vol. 57, no. 3, pp. 1027-1032, Aug. 2011

[3.15] Y. Chae *et al.*, “A 2.1 M pixels, 120 frame/s CMOS image sensor with column-parallel ΔΣADC architecture,” *IEEE J. Solid-State Circuits*, vol. 46, no. 1, pp. 236–247, Jan. 2011.

[3.16] A. Agah *et al.*, “A high-resolution low-power incremental ΣΔ ADC with extended range for biosensor arrays,” *IEEE J. Solid-State Circuits*, vol. 45, no. 6, pp. 1099–1110, Jun. 2010.

[3.17] R. Wu, Y. Chae, J. Huijsing, and K. A. A. Makinwa, “A 20-b ±40-mV range read-out IC with 50-nV offset and 0.04% gain error for bridge transducers,” *IEEE J. Solid-State Circuits*, vol. 47, no. 9, pp. 2152–2163, Sep. 2012.

[3.18] J. Markus, J. Silva, and G. Temes, “Theory and applications of incremental ΣΔ converters,” *IEEE Trans. Circuits Syst. I*, vol. 51, no. 4, pp. 678–690, Apr. 2004.

[3.19] V. Quiquempoix, P. Deval, A. Barreto, G. Bellini, J. Markus, J. Silva and G. Temes, “A low-power 22-bit incremental ADC,” *IEEE J. Solid-State Circuits*, vol. 41, no. 7, pp. 1562–1571, Jul. 2006.

[3.20] C. Enz and G. Temes, “Circuit techniques for reducing the effects of op-amp imperfections: Autozeroing, correlated double sampling, and chopper stabilization,” *Proc. IEEE*, vol. 84, no. 11, pp. 1584–1614, Nov. 1996.

[3.21] L. Yao, M. Steyaert and W. Sansen, “A 1-V 140- W 88-dB audio sigma-delta modulator in 90-nm CMOS,” *IEEE J. Solid-State Circuits*, vol. 39, no. 11, pp. 1809–1818, Nov. 2004.

[3.22] H. Kulah, J. Chae, N. Yazdi and K. Najafi, “Noise analysis and characterization of a sigma-delta capacitive microaccelerometer,” *IEEE J.Solid-State Circuits*, vol. 41, no. 2, pp. 352–361, Feb. 2006.

[4.1] J.-E. Park, D.-H. Lim and D.-K. Jeong, "A Reconfigurable 40-to-67 dB SNR, 50-to-6400 Hz Frame-Rate, Column-Parallel Readout IC for Capacitive Touch-Screen Panels," *IEEE J. Solid-State Circuits*, vol. 49, no. 10, pp. 2305-2318, Oct. 2014.

[4.2] J. H. Yang *et al.*, "A highly noise-immune touch controller using Filtered-Delta-Integration and a charge-interpolation technique for 10.1-inch capacitive touch-screen panels," *in IEEE ISSCC Dig. Tech. Papers*, 2013, pp. 390-391.

[4.3] Interoperability Specifications of Common External Power Supply (EPS) for Use with Data-Enabled Mobile Telephones, IEC 62684, Edition 1.0, 2011.

[4.4] H. Shin, S. Ko, H. Jang, I. Yun and K. Lee, "A 55dB SNR with 240Hz frame scan rate mutual capacitor 30×24 touch-screen panel read-out IC using code-division multiple sensing technique," *in IEEE ISSCC Dig. Tech.* Papers, 2013, pp. 388-389.

[4.5] J.-E. Park, J. Park, Y.-H. Hwang, J. Oh and D.-K. Jeong, " A 100-TRX-channel configurable 85-to-385Hz-frame-rate analog front-end for touch controller with highly enhanced noise immunity of 20Vpp," *in IEEE ISSCC Dig. Tech. Papers*, 2016, pp. 210-211.

[4.6] H. Jang, H. Shin, S. Ko, I. Yun and K. Lee, "2D Coded-aperture-based ultra-compact capacitive touch-screen controller with 40 reconfigurable channels," *in IEEE ISSCC Dig. Tech. Papers*, 2014, pp. 218-219.

[4.7] C. Park *et al.*, "A Pen-Pressure-Sensitive Capacitive Touch System Using Electrically Coupled Resonance Pen," *IEEE J. Solid-State Circuits*, vol. 51, no. 1, pp. 168-176, Jan. 2016.

[4.8] M. Miyamoto, M. Hamaguchi and A. Nagao, "A 143×81 Mutual-Capacitance Touch-Sensing Analog Front-End With Parallel Drive and Differential Sensing Architecture," *IEEE J. Solid-State Circuits*, vol. 50, no. 1, pp. 335-343, Jan. 2015.

[4.9] J. K. Park, C.J. Lee, D.Y. Kim, J. H. Chun and J. T. Kim, "Application of 4k-order Hadamard matrices to simultaneous driving capacitive touch systems," IEEE International Conference on Consumer Electronics (ICCE), 2015, pp. 564-565.

[4.10] J. K. Park, C. J. Lee, J. H. Kim, J. H. Chun and J. T. Kim, "Application of weighing matrices to simultaneous driving technique for capacitive touch sensors," *IEEE Trans. Consumer Elec.*, vol. 61, no. 2, pp. 261-269, May 2015.

[4.11] Tonchev, Vladimir D., “Hadamard matrices of order 36 with automorphisms of order 17,” Nagoya Math. J. 104 (1986), 163-174.

[4.12] Z. Janko, "The Existence of a Bush-type Hadamard Matrix of Order 36 and Two New Infinite Classes of Symmetric Designs," in Journal of Combinatorial Theory, Series A, vol.95, no.2, pp.360-364, Aug. 2001.

[4.13] J. Lee, D. Yeo, H. Kwon, B. Kim and H. Park, "An LCD-VCOM-Noise Resilient Mutual-Capacitive Touch-Sensor IC Chip With a Low-Voltage

Driving Signal," *in IEEE Sensors Journal*, vol. 15, no. 8, pp. 4595-4602, Aug. 2015.

[4.14] K.-D. Kim *et al.*, "A fully-differential capacitive touch controller with input common-mode feedback for symmetric display noise cancellation," *in in Proceeding of Symposium on VLSI*, Jun. 2014, pp.1-2.

[4.15] Jun-Eun Park, “Design of high SNR analog front-end circuit for touch screen sensor interface”, M.S. thesis, Seoul National University, Feb. 2013.

[4.16] Dong-Hyuk Lim, “Design Considerations of a Low-Noise Frontend for Capacitive Touch Screen Controllers”, Ph.D. thesis, Seoul National University, Feb. 2013.

[4.17] D.-H. Lim, J.-E. Park and D.-K. Jeong, "A low-noise differential front-end and its controller for capacitive touch screen panels," *in proceedings of the ESSCIRC*, Sept. 2012, pp. 237-240.

[4.18] I.-S. Yang and O.-K. Kwon, "A touch controller using differential sens,ing method for on-cell capacitive touch screen panel systems," *IEEE Transactions on Consumer Electronics*, vol. 57, no. 3, pp. 1027-1032, Aug. 2011.

[4.19] J.-E. Park, D.-H. Lim and D.-K. Jeong, "A 6.3 mW high-SNR frame-rate scalable touch screen panel readout IC with column-parallel Σ-Δ ADC structure for mobile devices," *in proceedings of A-SSCC*, Nov. 2013, pp. 357-360.

[4.20] M. Hamaguchi, A. Nagao and M. Miyamoto, "A 240Hz-reporting-rate 143×81 mutual-capacitance touch-sensing analog front-end IC with 37dB SNR for 1mm-diameter stylus," *in IEEE ISSCC Dig. Tech. Papers*, 2014, pp. 214-215.

[4.21] V. Kremin and A. Konovalov, “Method and apparatus for reducing coupled noise influence in touch screen controllers,” U.S. Patent application 2011/0115729 A1, May 2011.

[4.22] J.-M. Baek, D.-J. Seo, J.-H. Chun, and K.-W. Kwon, "A Dual Charge Pump for Quiescent Touch Sensor Power Supply," *IEEE Trans. Circuits and Syst. II, Exp. Briefs*, vol. 59, no. 11, pp. 780-784, Nov. 2012.

[4.23] S. Ko, H. Shin, H. Jang, I. Yun and K. Lee, "A 70dB SNR capacitive touch screen panel readout IC using capacitor-less trans-impedance amplifier and coded Orthogonal Frequency-Division Multiple Sensing scheme*," in Proceeding of Symposium on VLSI*, Jun. 2013, pp. C216-C217.

[4.24] M. G. A. Mohamed, A. N. Ragheb, H. Hassan and H. Kim, "OFDM and TDM based sensing method for large projected mutual-capacitance touch screens," *in Proceeding of IEEE International Conference on Consumer Electronics (ICCE)*, 2016, pp. 192-195.

[4.25] S. Heo *et al.*, "72 dB SNR, 240 Hz Frame Rate Readout IC With Differential Continuous-Mode Parallel Architecture for Larger Touch-Screen Panel Applications," in *IEEE Trans. Circuits and Syst. I*, vol. 63, no. 7, pp. 960-971, July 2016.

[4.26] Sean Erik O`connor and Wayne Carl Westerman, “Noise detection in multi-touch sensors,” U.S. Patent application 7643011 B2, Jan. 2010.

[4.27] H. W. Klein, “Noise Immunity of Touchscreen Devices,” [Online] Available: http://www.cypress.com/file/120641/download.

[4.28] Silicon Labs, “Understanding capacitive sensing signal to noise ratios and setting reliable thresholds,” [Online] Available: https://www.silabs.com /Support%20Documents/TechnicalDocs/AN367.pdf

[4.29] T. O’Connor, “mTouch™ Projected Capacitive Touch Screen Sensing Theory of Operation,” [Online] Available: https://www.microchip.com/ stellent/groups/techpub_sg/documents/devicedoc/en550192.pdf

[4.30] S.P. Hotelling and C.H. Krah, “Touch Controller with Improved Analog Front End,” U.S. Patent 8,031,094 B2, Oct. 4, 2011.

[4.31] W.R. Krenik and A. Dabak, “Touch-Sensitive Interface and Method Using Orthogonal Signaling,” U.S. Patent 2012/0056841 A1, Mar. 8, 2012.

[4.32] C. C. Enz and G. C. Temes, "Circuit techniques for reducing the effects of op-amp imperfections: autozeroing, correlated double sampling, and chopper stabilization," *in Proceedings of the IEEE*, vol. 84, no. 11, pp. 1584-1614, Nov 1996.

[4.33] B. Razavi, "Design considerations for direct-conversion receivers," in *IEEE Trans. Circuits and Syst. II*, vol. 44, no. 6, pp. 428-435, Jun 1997.

[4.34] Alan V. Oppenheim and Ronald W. Schafer, "Discrete-Time Signal Processing," Pearson Education, 2010.

[4.35] Y. Chae *et al.*, “A 2.1 M pixels, 120 frame/s CMOS image sensor with column-parallel ΔΣADC architecture,” *IEEE J. Solid-State Circuits*, vol. 46, no. 1, pp. 236–247, Jan. 2011.

[4.36] T. C. Caldwell and D. A. Johns, "Incremental Data Converters at Low Oversampling Ratios," *IEEE Trans. Circuits and Syst. I*, vol. 57, no. 7, pp. 1525-1537, July 2010.

[4.37] J. Markus, J. Silva, and G. Temes, "Theory and applications of incremental ΣΔ converters, " *IEEE Trans. Circuits Syst. I*, vol. 51, no. 4, pp. 678–690, Apr. 2004.

[4.38] K. Lim, K. S. Jung, C. S. Jang, J. S. Baek and I. B. Kang, "A Fast and Energy Efficient Single-Chip Touch Controller for Tablet Touch Applications," *IEEE/OSA J. Display Technol.*, vol. 9, no. 7, pp. 520-526, July 2013.

[4.39] K. J. Horadam, "Hadamard matrices and their applications," Princeton University Press, 2007.

[4.40] R. Hogervorst, J. P. Tero, R. G. H. Eschauzier and J. H. Huijsing, "A compact power-efficient 3 V CMOS rail-to-rail input/output operational amplifier for VLSI cell libraries," *IEEE J. Solid-State Circuits*, vol. 29, no. 12, pp. 1505-1513, Dec 1994.

[4.41] T. Kuehl, “Using the infinite-gain, MFB filter topology in fully differential active filters,” [Online] Available: http://www.ti.com/lit/an/slyt343/slyt343.pdf.

[4.42] J. Markus, P. Deval, V. Quiquempoix, J. Silva and G. C. Temes, "Incremental Delta-Sigma Structures for DC Measurement: an Overview," *in Proceeding of IEEE CICC*, 2006, pp. 41-48.

[4.43] L. Yao, M. Steyaert, and W. Sansen, "A 1-V 140- W 88-dB audio sigma-delta modulator in 90-nm CMOS," *IEEE J. Solid-State Circuits*, vol. 39, no. 11, pp. 1809-1818, Nov. 2004.

[4.44] M. Hamaguchi, M. Takeda and M. Miyamoto, "A 240Hz-reporting-rate mutual-capacitance touch-sensing analog front-end enabling multiple active/passive styluses with 41dB/32dB SNR for 0.5mm diameter," *in IEEE ISSCC Dig. Tech. Papers*, 2015, pp. 120-121.

[4.45] P. Tomas, J. Cleary, and A. C. Galve. "Noise compensation techniques for capacitive touch screen systems." U.S. Patent Application No. 13/665,425.

초 록

본 논문에서는 강화된 잡음 면역성과 신호 대 잡음 비 (SNR) 및 프레임률 (frame rate) 조절이 가능한 터치스크린 컨트롤러용 (touch-screen controller) 아날로그 전단 회로 (analog front-end)의 설계 방법을 제안한다. 먼저 모바일용 터치스크린 컨트롤러 아날로그 전단 회로의 설계를 통해 조절 가능한 신호 대 잡음 비 및 프레임률을 구현하였다. 아날로그 디지털 변환기에서 샘플링 되는 신호의 수를 조절 함으로써 통해 아날로그 전단회로의 전체적인 신호 대 잡음 비 특성 및 프레임률을 조절 하였다. 0.18μm CMOS 공정을 이용하여 만들어진 칩은 60 dB 의 신호 대 잡음 비와 200 Hz 의 프레임률을 가진다. 신호 대 잡음 비의 조절 가능한 영역은 40 dB 에서 67 dB 이며 이에 따른 프레임률 변화는 50 Hz 에서 6400 Hz 이다. 총 소모 전력은 6.26 mW 이다.

다음으로 태블릿용 터치스크린 컨트롤러 아날로그 전단 회로의 설계에 있어서 높은 잡음 면역성을 얻기 위해 동시에 여러 개의 구동 채널을 사용하는 다중 구동 변조 방식 (multi-driving TX modulation)을 사용하였다. 이 때 기존의 변조 방식에서 사용되던 변조 코드 대신 제안하는 새로운 변조 코드를 이용해 오프셋 및 위상 지연에 의한 문제를 해결하였다. 또한 터치스크린 패널을 통해 유입되는 외부 잡음을 제거하기 위해 고차의 잡음 제거 필터를 사용하였다. 이에 더해 터치 물체를 통해 인가되는 잡음에 의한 신호 왜곡을 줄이는 선 필터링 방식의 차동 구조 센싱 회로를 제안하였다. 여기에 추가적인 변조 방식을 센싱 회로에 적용 시킴으로써 면적 소모를 줄이고 잡음 면역성을 더욱 강화 시켰다. 0.18μm

CMOS 공정을 이용하여 만들어진 아날로그 전단 회로는 최대 20 V_{pp} 의 잡음 간섭에 대해서 면역성을 가지며 120 Hz 의 프레임률에서 54 dB 의 신호 대 잡음 비 특성을 나타내었다. 총 소모 전력은 94.5 mW 이다.

주요어 : 터치스크린 컨트롤러, 아날로그 전단 회로, 잡음 면역성, 신호 대 잡음 비, 프레임률, 터치스크린 패널.

학 번 : 2013-30237